Development of Whole-Cell Diagnostic Techniques and Tools for Lithium-ion Batteries

Victor W. Hu

A dissertation
submitted in partial fulfillment of the
requirements for the degree of

Doctor of Philosophy

University of Washington

2022

Reading Committee:

Daniel T. Schwartz, Chair
David A. C. Beck
Stuart B. Adler

Program Authorized to Offer Degree:
Chemical Engineering

University of Washington

Abstract

Development of Whole-Cell Diagnostic Techniques and Tools for Lithium-ion Batteries

Victor W. Hu

Chair of the Supervisory Committee:

Professor Daniel T. Schwartz

Chemical Engineering

Whole-cell diagnostic methods and analysis tools are critical for characterizing lithium-ion batteries as we aim to increase the performance and lifetime of these devices while also minimizing safety concerns and cost. Diagnostics of whole-cells can be significantly more complicated than their half-cell counterparts because of the lack of a reference electrode, and complex way two active electrodes interact with each other to yield a whole-cell response. The complexity of whole-cell electrochemical methods adds a further burden to the quality and reproducibility of the experimental data used to validate the performance of whole-cell analysis tools.

We create a dataset used in all subsequent analysis that is well replicated and is used to showcase the statistical attributes of a testing regime carried out using Samsung INR 18650-15M cells with NMC | Graphite chemistry aged to different states-of-health (SoH) at different charging rates and temperatures. The dataset includes measurements of open-circuit voltage (OCV) from low C-rate scanning along with differential analysis of OCV and capacity, electrochemical impedance (EIS) and nonlinear electrochemical impedance (NLEIS) measurements. Quadruplicate measurements were taken for nearly all conditions.

Using data from our well-characterized cells, we adapt the half-cell Multi-Species, Multi-Reaction (MSMR) model into a whole-cell diagnostic tool via inclusion of whole-cell design parameters and cell charge balance constraints. The whole-cell model is first compared to experiments using literature reference values for the MSMR thermodynamic parameters. To improve fit quality, the MSMR thermodynamic parameters and electrode capacities are simultaneously fit to the OCV and differential voltage data, producing low error, high quality fits

to experiments. Bootstrap analysis is performed to show the robustness of the fitting software to experimental noise and data sampling. The MSMR results quantify which insertion reactions are most responsible for capacity loss in each electrode, while also showing how slippage in the lithiation window, changes in useable capacity, and other properties evolve as the cell ages.

Finally, in this work, we provided an experimental framework for nonlinear electrochemical impedance spectroscopy (NLEIS). Increasing the input AC signal from the classic small-amplitude linear limit to a moderate amplitude that produces a second harmonic in the output signal (but no other harmonics), then the first-harmonic signal remains a valid representation of the linear response, while the second harmonic signal introduces new physics to the analysis. We show how the second harmonic NLEIS spectra build from, but complements, the Warburg and interfacial charge transfer response of the cell, providing unique insights into the evolution of charge transfer symmetry at low SOC as the cathode ages during cycling.

These results launched two additional studies, where we collected the linear and nonlinear impedance response over much tighter SoC ranges to try and explore the emergence of these second harmonic charge-transfer kinetics and higher-order thermodynamic properties. We use traditional equivalent circuit elements to analyze the linear EIS, and then derive nonlinear equivalent circuit elements to model the NLEIS. Here, we also show that with inclusion of thermodynamic information achieved through the MSMR model, these new nonlinear circuit elements can capture the behavior we see in the charge-transfer asymmetry as well as the direction and quadrant that these nonlinear low-frequency may extend into. Finally, we also employ a full-physics pseudo-2-dimensional model, to show the general validity of the results we see from using the simpler, empirical equivalent circuit models.

Table of Contents

List of Figures

List of Tables

Acknowledgments

No words can truly describe how grateful I am to everybody who has helped and supported me throughout the years to finally reach this point in my graduate career. First and foremost, I want to start by thanking my committee members, Dan Schwartz, David Beck, Stuart Adler, and Gerald Seidler for your support, guidance, and thoughtful discussions throughout my Ph.D. I especially want to thank my Ph.D. adviser, Dan Schwartz for your support and mentorship throughout my years here. Your excitement and enthusiasm for mentoring and education is truly uplifting and inspiring, and your passion for science and research can make anyone smile. I'll always remember the first time we were able to have a research meeting in person again in late 2021, where you wanted to take a selfie to "commemorate us doing science in person again."

I also want to say a big thank you to all my fellow lab mates in the EMI Lab, both past and present. I want to especially thank Dr. Matthew Murbach, who made me feel especially welcomed when I joined the group and provided me with an incredible amount of research guidance when starting out. Thanks for letting me bring the fun back in and out of the lab! I'm also incredibly thankful for Erica Eggleton and Linnette Teo, who have been extraordinary research partners and been my partners-in-crime in and out of the lab throughout these last several years. Also, a big thank you to Dr. Karl Oleson, Dr. Yanbo Qi, Dr. Caitlin Parke, Dr. Akshay Subramanian, Mihyun Kim, Maitri Uppaluri, Yuefan Ji, and Rose Lee for all the memories both in and out of the office.

One of the things I have loved most about my Ph.D. is the community and network of friends at the UW that I have made throughout the years. You all are incredible people and have made such an impact on my life. It is truly one of the greatest support groups that I've found to help celebrate the wins and highs and to commiserate and comfort during the lows. I am eternally grateful for Dr. Luke Gibson, Dr. Caitlyn Wolf, Dr. Brittany Bishop, Dr. Neal Dawson-Elli, and Dr. Sheila Goodman. Each of you have made such a profound impact on my life and I cannot wait to see where our future takes us. I also want to thank Dr. Brian Gerwe, Dr. Jon Witt, Dr. Elena Pandres, Laura Dobrowski, Lindsay Blaire, Dr. Sarah Alamdari, Dr. Jaime Rodriguez, Sage Schweiller, Hawley Helmbrecht, Julia King, Jenny Stukenberg, and Olaf Bergeson for making these years fly by and for making Seattle feel like home. I also want to thank all my friends from before graduate school, who decided to still be friends with me even if I decided to move across

the country. I am thankful to Meghan Dawe, Elizabeth Bliss, Taryn Loomis, Jennifer Bombard, Jeffrey Martin, Jacob Zagorski, Nick McMahon, Sam La, Kayla DeSanty, Sean Amos, Johanna Noelk, and Stefania Khoda.

Lastly, I want to say thank you to my family. To all my cousins, thank you for the amazing memories, camaraderie, and love you have all shown me. I'm also thankful to my siblings Peter and Helen for all the great memories, guidance, and love they have given me. Finally, I am eternally thankful to my parents Jin and Si, who have provided me with immense love and support.

Dedication

To my family and friends,

Thank you for everything

Chapter 1 - Introduction

1.1 Background and Motivation

Advances in energy storage are critical as the world aims to electrify everything with variable renewable energy.[1,2] Lithium-ion batteries, the dominant electrochemical energy storage technology, consist of three major components, the anode, cathode, and the electrolyte/separator that allows ion conductivity without electrical shorting. Each of these components have ongoing, active research thrusts that are trying to increase energy density, power density, coulombic efficiency, cycle life, and safety.[3]

In fundamental battery research, half-cell experiments play a critical role. Battery half-cells are a simplified configuration that allows detailed study of the anode/electrolyte or cathode/electrolyte performance by using bulk lithium metal foil as both the counter and reference electrode. Since lithium cations are involved in both the anode and cathode reaction for lithium-ion insertion electrodes, bulk lithium metal can serve as a nearly ideal, stable reference electrode which has a large specific capacity, when prepared correctly.[4] Conventionally, new electrode materials are tested under conditions that minimize complexity, for example, using excess electrolyte (called flooded conditions) and thick lithium foil reference/counter electrodes. Because of the simplified conditions, half-cells are useful for determining fundamental thermodynamic, kinetic, and transport properties from electrochemical measurements. Moreover, the simplicity of the cell supports complementary *operando* x-ray crystallography and chemical composition studies, and so much more.[5–9]

However, half-cells offer an incomplete window into the chemical and physical processes that control the performance of the advanced batteries that are ubiquitous in the market. In a commercially viable full-cell (or whole-cell), both the anode and cathode are highly engineered electrodes that seek to maximize the amount of active material and cell potential, while using increasingly thinner separators, resulting in very lean electrolyte conditions, leading to undesired reactions.[10,11]

When constructing whole-cells, a new set of design challenges begin to make themselves apparent, with the capacity ratios, lithiation ranges, and voltage limits for each electrode and the whole cell becoming a coupled set of design parameters. In whole-cells, the capacities of the cathode and anode are not equal. In almost all commercial lithium-ion batteries, the anode material is a form of natural or synthetic graphite fabricated into a porous electrode with 10 to 30% more capacity than the cathode (to limit safety hazard associated with lithium plating on the anode during charging).[12,13] As a result, neither electrode is fully cycled , but instead often have a shallow range for lithiation and delithiation to improve the lifetime of batteries in real-world applications, to prevent lithium plating, or slow irreversible structural deformation in some layered transition metal oxides cathodes.

At a fundamental level, whole-cells consist of two materials, one a powerful reducer and the other a powerful oxidizer, held microns apart by an ionically conductive electrolyte/separator.[14–16] Half-cells fail to capture the chemical interactivity of these materials, whereas whole-cells are subject to the ramifications of these interactions. The most prevalent example is in full-cells with cathode materials containing manganese, such as spinel-manganese oxide, or layered Nickel-Manganese-Cobalt (NMC) electrodes. In these cells, Mn ions have the ability to dissolve into the electrolyte, cross through the separator, and deposit themselves into the solid-electrolyte interphase (SEI), a critical passivating layer that forms from electrolyte degradation on the graphite electrode, where they can act as catalysts for further electrolyte degradation and SEI growth (to the point where cell performance is damaged).[17–19] Thus, to truly understand the physical and chemical properties of advanced batteries, whole-cells must be studied, not just isolated half-cell electrodes.

Electrochemical methods are mostly oriented toward analyzing half-cells to extract fundamental thermodynamic, kinetic, and transport parameters. Half-cell methods such as low-C rate cycling, differential voltage and/or capacity analysis, galvanostatic or potentiostatic intermittent titration techniques, electrochemical impedance spectroscopy, and much more have been applied to whole-cells. However, the added complexity of having two active electrode responses, and no reference electrode to anchor the thermodynamic potential, makes it difficult to separate the effects of anode and cathode with confidence.[20–22] The total electrochemical signal is built from the response of the two individual electrodes. For example, the whole-cell open circuit voltage (OCV) arises by subtracting the thermodynamic half-cell potential of the anode from the cathode (*negative parity*). The differential voltage adds the differential half-cell potentials for the

cathode and anode (*positive parity*).[23] Likewise, whole-cell electrochemical impedance spectroscopy (EIS) is well known to have *positive parity*, that is, it arises from the sum of the individual half-cell impedances. We have shown that the whole-cell 2nd harmonic nonlinear EIS has *negative parity* and is derived by the difference of half-cell 2nd harmonic NLEIS from each electrode.[24] Understanding the mathematical framework that describes these signal parities, and using one set of physics-based models to describe each half-cell, is a critical idea developed here for whole-cell diagnostic tools that can be used to extract physicochemical properties of the whole cell.[20,23,24]

In order to ensure proper whole-cell experimental and modeling technique development, it is important to use batteries under test that are reproducible and reliable within a very narrow tolerance.[25] Otherwise, it is unclear if the signals collected, and quality of model fit, are from instrumentation or manufacturing variance. Because of this, in this thesis we ensure a high level of replication of experiments, even for long duration aging studies.

1.2 Whole-cell thermodynamic modeling

In batteries, the solid-state thermodynamics of lithium insertion electrode materials dictate the phases and open-circuit potentials of the half-cells as the material is lithiated or delithiated.[26,27] In a fresh whole-cell, the open circuit potentials of two know half-cells accurately represent the (negative parity) whole-cell OCV. However, as cells age, solid state materials are transformed by repeated lithiation/delithiation, as is the electrolyte, in ways that depend on the whole-cell design. Thus, physics-based modeling tools are needed that can deconvolute the evolving half-cell thermodynamic behavior from whole-cell electrochemical measurements.

Electrochemical methods, such as galvanostatic or potential intermittent titration technique[28,29], electrochemical impedance spectroscopy[30–32], and differential voltammetry techniques[33–35] can be used with half-cells and whole-cells, and each has a thermodynamic signature. Yet, the simplest and most common techniques used though in battery thermodynamic analysis is low-rate galvanostatic cycling and its complementary differential voltage or capacity analysis, where a very low C-rate is applied to the a half-cell or whole-cell of interest.[5,36,37] At low enough C-rates, the measured signal is taken to be the thermodynamic open circuit potential of a half-cell or OCV of a whole-cell. Without a reference electrode though, as in commercial whole-

cell batteries, the negative parity OCV alone cannot uniquely determine each half-cell thermodynamic potential[23,38,39]

Differential voltage (dU/dQ), and its inverse, differential capacity (dQ/dU) are positive parity signals that are sensitive to insertion electrodes solid state energetics.[23,39] In whole-cells, differential voltage and differential capacity is often used to interpret mechanisms for battery degradation and fade, inhomogeneous material degradation, and slippage.[40–42]

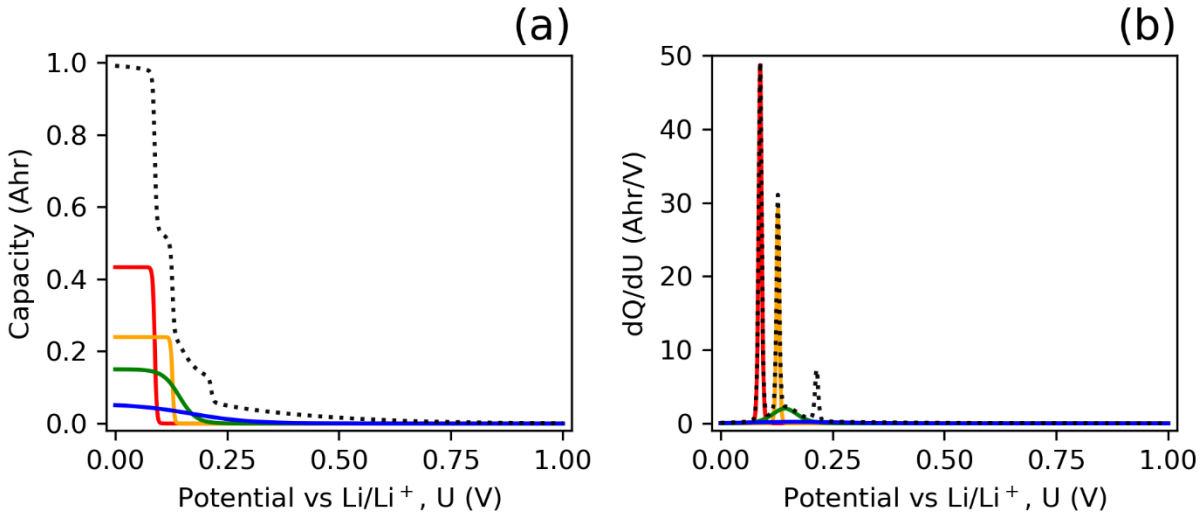

Figure 1.1 Capacity (a) and differential capacity (b) plotted against a lithium half-cell reference potential. Each individual colorized line represents one of the six different staging reactions in graphite, with the dotted black line representing the cumulative electrode response for both the capacity and differential capacity.

Quantitative thermodynamic models of insertion materials link the equilibrium potential to the extent of litigation and phases that form.[43] However, the complexity of full-physics models can limit their usefulness.[44–46] One model of interest that aims to reduce this complexity but also provide important information on the thermodynamics and solid-state relationships is the Multi-Species, Multi-Reaction (MSMR) model developed by Verbrugge et al., at General Motors.[7,47–49] In the MSMR model framework, the overarching notion is that an electrode's open-circuit potential plot is a result of a series of solid-state reactions, associated with different lithiated phases in layered transition-metal oxide electrodes[48], graphite electrodes[47], as well as conversion reactions, such as silicon electrodes.[7] Each reaction can be modeled with three interpretable parameters, yielding half-cell potential responses such as those shown in Figure 1.1, for a graphite

electrode. Each colored line in both plots show a different reaction. The cumulative response is the superposition of all the individual signals for any given voltage. While this model was first developed for examining half-cell systems, the inclusion of some design parameters allows it to be shifted into the whole-cell paradigm, allowing it to be used to study the individual electrodes in a functional cell, as shown in Chapter 3

1.3 Electrochemical impedance spectroscopy

Electrochemical impedance spectroscopy (EIS), is a diagnostic tool that can nondestructively probe physicochemical phenomena in electrochemical systems using a small AC signal and measuring its subsequent response.[50] In galvanostatic EIS, a small-amplitude sinusoidal current input is used to modulate the battery the resulting, phase-shifted sinusoidal voltage response is collected. Assuming the input current was a perfect cosine wave, at a given input frequency, ω, the impedance of the device is defined as:

$$Z(\omega) = \frac{\Delta V \cos(\omega t + \theta)}{\Delta I \cos(\omega t)} \qquad [1.1]$$

In a typical EIS experiment, the impedance is measured over a wide range of different frequencies. These impedances are commonly broken up into their real, Z'(ω), and imaginary, Z"(ω) components, and then displayed in a Nyquist plot, as shown in Figure 1.2.

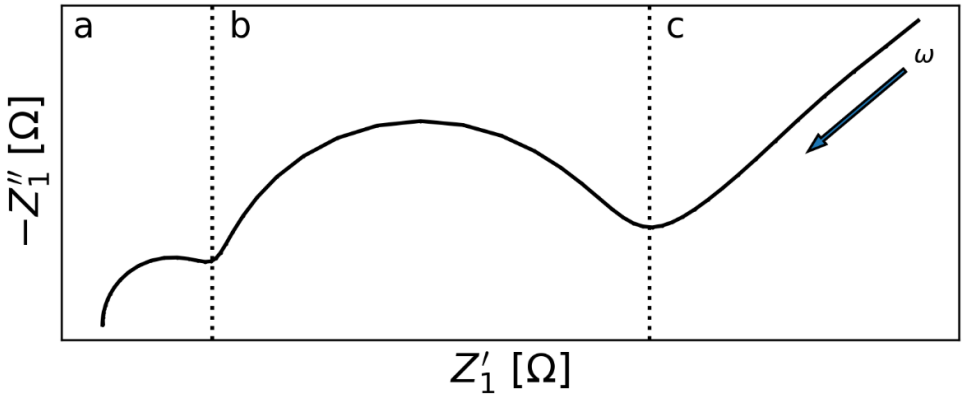

Figure 1.2 Sample Nyquist plot showing the real and imaginary impedances, broken into three sections, where (a) shows the high-frequency limit, and one electrode kinetics, (b) kinetics and interfacial processes of the more sluggish electrode, and (c) with the low-frequency tail influenced by thermodynamics and transport properties.

Lithium-ion batteries are complex systems, where several different physical and chemical behaviors are all occurring at different time scales. EIS is unique, in that the wide frequency scans allows for the separation and deconvolution of some of these behaviors that information. at the limit of the high frequency, the ohmic resistance of the device can be measured, as the high scan rates occur at too rapid a pace for any interfacial or diffusion phenomena to happen.[50] Due to instrumentation and experimental error, inductance caused by the high frequencies can lead to positive imaginary components. At slightly lower frequencies where cells can now have a measurable intercalation/deintercalation, EIS is able to probe interfacial reactions, such as charge-transfer, double-layer capacitances, or degradative side reactions.[5,30,51–55] In this regime, EIS also is capable of distinguishing if one electrode has more sluggish kinetics than the other, as shown in region a and b in Figure 1.2. Finally, at low enough frequencies, like in section c of Figure 1.2, a tail-element becomes apparent, which contains information on thermodynamic and mass transport.

Typical analysis of EIS is using equivalent circuit models, with multiple analysis programs available to do this type of model fitting to data.[56] Equivalent circuits have the distinct advantage, in that they are very simple to use, where the simplest model for a full battery can be modeled by an ohmic resistor and two RC circuits (resistor and capacitor in parallel) connected in series, as shown in Fig 1.3. These RC circuits represent the faradaic current that passes through the charge-transfer resistance and the non-faradaic current carried through the double-layer capacitance. However, these RC circuits capture the interfacial response and do not consider any contributions from mass-transfer limitations. Thus, a typical equivalent circuit in battery research is the Randle's circuit, 1b, which includes a Warburg impedance, Z_w, in the faradaic branch, that encapsulates the effects of mass-transfer limitations in the impedance measurements. Researchers have used equivalent circuit modeling in EIS to study phenomena like electrode kinetics and lithium-ion transport,[29,51] and capacity loss mechanisms,[5,30] such as SEI layer deposition and growth.[53–55]

A major shortcoming of EIS though is that is a linearized method, and applications of it to an inherently nonlinear system can reduce the informational content that's retrievable. EIS spectra are often analyzed using equivalent circuit models,[57] and in rare instances, linearized physics-based models,[58] but the drawbacks to these methods of analysis is degeneracy, meaning that a single EIS spectra can be represented equivalently by multiple solutions.[59] EIS signals from whole cells have positive parity, and arise from the sum of the two half-cell impedances.

1.4 Nonlinear electrochemical impedance spectroscopy

A variant of EIS, nonlinear EIS (NLEIS) uses an increased magnitude of the input modulation so that the system of interest enters a weakly nonlinear regime.[24] The moderate-amplitude single-sine input produces small, but measurable, outputs at one or more higher harmonics of the fundamental frequency in the Fourier transform. These signals have previously been regarded as corruption to the linear response and often removed in the signal processing steps of EIS.[60–63] However, these signals could be used to examine nonlinear phenomena and have been used in the fields of corrosion,[64–66] fuel cells,[67–69] mass-transport-controlled systems,[70–72] chemical sensing,[73–75] and more recently lithium-ion batteries.[76,77]

Lvovich and Smiechowski were able to characterize degradation in industrial lubricants through monotonic trends in the second harmonic linear responses, while the linear responses had no discernible pattern.[78] Wilson et al. used a mixture of NLEIS and physical models to determine the rate-determining mechanism of the oxygen-reduction reaction on solid oxide fuel cells, despite the models having degenerate answers in the traditional response.[67,68] Xu and Riley were able to look at even harmonics in the ferri-ferrocyanide redox couple to examine transfer coefficients, which are often hard to experimentally determine.[79] Heubner et al., then applied these same principles to gather transfer coefficients in lithium-iron phosphate cathodes.[80] More recently, studies on the total harmonic distortion from higher harmonic responses have been used to examine nonlinear faradaic processes and battery degradation.[76,81,82]

It is important to reiterate that the NLEIS method presented in this document is related to the weakly nonlinear regime, meaning that the number of measurable harmonics is few in number and that the voltage modulation does not exceed 25 mV. Due to this, NLEIS measurements can be a valuable complement to EIS, especially since it also does not require any new equipment. With small changes to the experiment methods and signal processing, higher harmonic NLEIS spectra can be calculated and better understood when analyzed in conjunction with a physics-based model.[77] The inclusion of NLEIS and expanded models that look at the nonlinear phenomena can break the degeneracy of traditional, linearized models.[67] Given the additional heightened sensitivity of NLEIS measurements and the eliminated risk of degeneracy, this technique could then be applied to study specific frequencies with a comprehensive physics-based model and estimate valuable parameters values. As we show in Chapter 4, second harmonic NLEIS is a

complementary technique to EIS, as it both reduces degeneracy inherent to EIS, but also has a negative whole-cell measurement parity compared to the positive whole-cell parity of EIS.

Chapter 2 - Battery Corpus: An open-access dataset of commercially available lithium-ion NMC batteries exploring experimental variability in battery degradation

2.1 Introduction

Li-ion cell and pack prices have declined by roughly 15% annually over the past five years[83] driving exponential growth in the demand for batteries in applications such as consumer electronics, commercial and industrial demand management, grid-scale renewables storage, and especially electric vehicles. Innovations in materials, manufacturing, and use-case information sciences are needed to optimally meet this burgeoning demand in the most economical and environmentally sound manner. An obstacle to the pace of innovation is a lack of open datasets that link manufacturing test and measurement data, application-specific user data, and data from battery second use applications.

Several groups have released battery cycling datasets that are of sufficient size for statistical and machine learning approaches[21,84–86], and some in-field user data is also emerging[87], but the raw data is not always accessible for re-use. Moreover, data quality metrics are rarely reported, nor are the metadata labels standardized for ease of reuse and reanalysis. In other fields, many of these barriers have been addressed, leading to data reuse and reanalysis have resulted in meta data standards, repository structures, and open licensing that make data available, findable, and reusable.[88,89]

To overcome these barriers to sharing and reusing battery data collected by others, there is a growing movement toward creating public data repositories[85,87,90] However, each group uses different data formats, metadata, and user-interfaces. Recently, a team of battery scientists and big-data experts created the Battery Genome Project to create a common data structure.[91] When battery datasets are accessible, more experts can explore the data in greater depth and offer alternative perspectives, insights, and analysis. Also, larger, and more comprehensive datasets can be made by combining efforts from multiple groups, which can then be used for machine learning tools.

Another obstacle is related to the quality metrics and reproducibility of battery datasets. Many experiments prioritize testing across multiple conditions but limit the number of cells at each

condition (often, just a single cell per test condition[86]). This information is useful for understanding basic battery capabilities, but in order to make statistically relevant conclusions and predictions, especially when testing is of new materials and chemistries in low volume production, rather than mass produced cells with high quality control, replicates are needed to minimize the effect of cell variability on the results.[92,93]

This work aims to contribute more cell cycling data to the community, focusing on commercial Samsung Li-NMC power cells. Nickel-Manganese-Cobalt (NMC) cathodes were chosen for this study because they have become more prominent due to their high energy density compared to Lithium-iron-phosphate and increased chemical stability and reduced cobalt content compared to Lithium-cobalt-oxide.[94] The dataset includes replicate cycling datasets and EIS measurements. We propose some aggregated statistical metrics that can be used to understand the dataset quality and identify outlier cells and experiments that exist even in mass produced cells. The data is published using the Battery Genome Project proposed JSON metadata file structure and includes a supplementary Jupyter Notebook to demonstrate the analysis and figures presented here, and to allow further investigation and data visualization from the broader community.

2.2 Methodology

2.2.1 Cycling Protocols

Commercially available Samsung 1.5 Ah Li NMC | C power cells (INR 18650-15M), all from the same manufacturers lot number, were used in all measurements. A total of 48 cells were used with a balance between replicate experiments and number of uniqure testing conditions, as summarized in the test matrix (Table 1). Two different charging C-rates (2.67C and 2.00C) and a common discharge rate were compared at two different environment temperatures (5°C and 25°C). The charging C-rates were chosen to accelerate testing and degradation, while staying within the 4A maximum charging rate recommended by the manufacture. The discharge rate for all cells was 3.00C. In short, all cells were subjected to fairly agressive charge and discharge condiitions. To glean information on the states-of-health (SOH) and reproducibility of cells operated under the four different conditions,

For each of the four unique test conditions, 12 cells were used, summing to 48 distinct cells that underwent cycling. To study the intermediate states-of-health (SOH) and probe the reproducibility of cells operated under each set of conditions, subsets of cells were cycled accordingly with the test matrix in Table 2.1. Diagnostics for cells cycled as shown in Table 2.1 included C/20 charge and discharge curves as well as electrochemical impedance spectroscopy (EIS) analysis at several different states-of-charge (SOC). An additional 4 fresh cells were used to collect open-circuit potential and impedance data at the beginning-of-life for this lot of cells. All of the 5°C experiments were completed using a Maccor 4000M 16-channel cycler in a Tenney TPS C-EVO Environment Testing Chamber and the 25°C were conducted with a Maccor 4000M 96-channel cycler in a Maccor MTC-020 environment chamber. Individual cell case temperature measurements were available only through the 96-channel cycler and thus these data are available on select cells for the 25°C datasets.

Each cell was allowed to equilibrate to the controlled temperature for four hours before being subjected to five break-in cycles at C/2 charge and discharge rates over the manufacturer recommended voltage range(2.5 V to 4.2 V). The cells were then aggressively cycled using one of the charging C-rate under study, and a 3C discharge rate, until they reached the target cycle number. The cells then underwent one more C/2 charge and discharge cycle for capacity comparisons with the beginning of life. The final measurement is the OCV measurement, which is conducted with low constant-current (C/20) measurements on charge and discharge. Once cells reached their target cycle number and had OCV and EIS measurements (as detailed in next section), they were removed from further cycling experiments. Prior work from this same class of commercial cells[24] showed that there was low cell-to-cell variability, but the extent of this variability has not been systematically characterized.

2.2.2 Electrochemical Testing

Following the cycling experiments and the OCV measurements, the cells were then removed and EIS measurements were collected using an Autolab PG-STAT128N potentiostat/galvanostat with the frequency response analyzer module (Autolab FRA32). All measurements were collected at 25°C using a four-electrode configuration with voltage sensing at the cell terminals, regardless of the cell cycling temperature.

For each cell, a rest step of at least four hours helped ensure thermal equilibrium. EIS measurements were then collected at specific voltages that correlate with 10% (3.500 V), 30% (3.643 V), and 50% (3.820 V) state-of-charge (SOC) for fresh cells in this chemistry. Since all cells were fully discharged at the end of the cycling protocol, the cell under test was charged at a C/10 rate to the desired voltage, where it would then enter a two-hour constant voltage charge step, before being allowed to rest for another two hours at open-circuit. Impedance measurements were made over a logarithmically spaced frequency range from 10 kHz to 5.01 mHz, with ten points per decade, using a minimum of five steady-periodic cycles, logged with 4096 data points.

Since all the cells are at varying degrees of degradation, the amplitude of the single-cosine current modulation waveform used to collect the impedance measurements, typically resulting in a voltage modulation around X mV, maximizing signal while avoiding measurable third harmonic responses (a signature of third-order distortions the linear EIS signal). To select the appropriate amperage, we used a cell from each of the different SOH and testing conditions and took impedance measurements at 0.100 and 0.010 Hz over a current range between 0.010 to 0.400 A at the three different SoCs. The time domain series data were then processed and amplitudes for EIS measurements for the remaining replicate cells for the condition of interest were selected where there were no detectable third harmonic signals.

2.2.3 Post-Processing, Validation, and Statistical Analyses

Due to inherent noise in the instrumentation, post-processing of the low-current (C/20) experiments was used to minimize noise in the differential information.[95] We applied a third-order polynomial Savitzy-Golay filter with a window-length of 99 points across the entire dataset, where a center voltage is selected with 49 points before and 49 points after. The differential voltage (dV/dQ) is thus computed, where capacity, Q, is directly related to the charge/discharge current. The different capacity (dQ/dV) was calculated by taking the inverse.

An important validation technique for impedance measurements is the Kramers-Kronig relationships. Proper Kramers-Kronig relations ensure that the impedance measurement is stationary, time-invariant, and is representative of a causal system. Here, we use the validation toolkit from the open-source software impedance.py, which implements the Kramers-Kronig methodology by Schönleber et al.[96,97]

To garner insight into experimental variability, statistical analysis was conducted for each measurement, at each condition for all replicate, following a common framework. First, the mean and the standard deviations are calculated at a consistent interval of the independent variable. Lower and upper limits of the envelopes of the 95% confidence intervals are calculated subtracting or adding two standard deviations to the mean value at that select interval, respectively. Relative standard deviations are also used in some of the later analysis and can be computed as the standard deviation/mean value*100%.

.

Table 2.1 Experimental Matrix with completed experiments marked

C-Rate (charge)	Temp	300 Cycles	600 Cycles	900 Cycles	1000 cycles+
2.00 C	5°C	4	4		4
2.67 C	5°C	4	4		4
2.00 C	25°C	4		4	4
2.67 C	25°C	4	2	2	4

2.3 Results and Discussion

2.3.1 Overview of data

The 3C discharge capacity of all 48 cells cycled cells cycled between 4.2 V and 2.5V, under the four different experimental conditions, are shown in Figure 2.1 as a function of cycle number. Cycles numbered 300, 600, and 900 are denoted by vertical dashed lines, since some cells were taken off-line at each of those cycle numbers for further EIS and low-rate C/20 testing. For each cycle number, the two standard deviations of true replicates (away from the mean capacity as shaded areas. The standard deviations are calculated based on the number of cells available at that particular cycle. The number of cells decreases as some cells are stopped at 300, 600, and 900 cycles according to our experimental matrix in Table 2.1. Note that some cells did not make it to 1500 cycles due to the experiments being stopped prematurely (though all these cells were degraded well past 80% capacity).

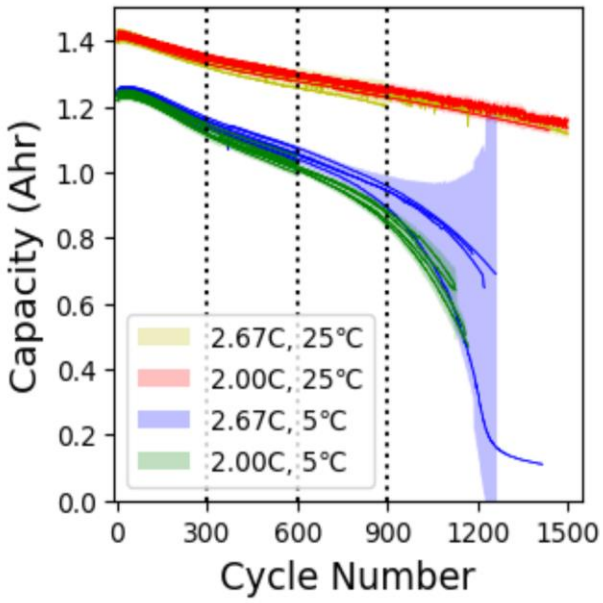

Figure 2.1 Capacity with cycles plot for all cycled cells under the four different experimental conditions Case 1: 2.67C, 25oC, Case 2: 2C, 25oC, Case 3: 2.67C, 5oC, and Case 4: 2C, 5oC. Shaded areas represent two standard deviations. For each condition, cells were cycled to either 300, 600, 900, or 1500 cycles, as noted by the dashed lines.

For the two conditions at 25°C, the initial capacity for all cells is higher than that at 5oC. Also, at the higher temperature, the cells follow a linear degradative trend, and the C-rate does not appear to have an effect on the capacity loss. For the cells cycled at the lower temperature, however, we see a steeper linear degradation trend initially, followed by nonlinear aging. There is also greater capacity loss at lower C-rates compared to higher C-rates, probably due to heat generation at higher C-rates, and much larger cell-to-cell variability.

Since we have replicates for each experimental condition, we can perform statistical analysis to get a measure of data quality which can be affected by experimental measurement quality or cell-to-cell variation. Having a way to measure data quality can give us confidence in the trends we see from a dataset and also allow us to easily pick out outliers. In this paper, we show a few examples of using simple statistical methods to qualify our dataset as a whole.

2.3.2 Voltage curves

For each experimental condition, we can examine the voltage curves at any cycle and also look at the variation within the replicate group of cells. For the experimental case, 2.67C and 25°C, there are eight cells that reach cycle 500. Figure 2.2 shows the mean of the charge and discharge voltages (normalized by capacity) of these eight cells at cycle 500. The two standard deviations calculated and shown as shaded areas in Figure 2.2 are relatively small but there is still some variation in the voltage curves for these well manufactured commercial cells. This is an example of only one of the experimental conditions. Refer to the Jupyter notebook accompanying this paper to look at data for other conditions at various cycles.

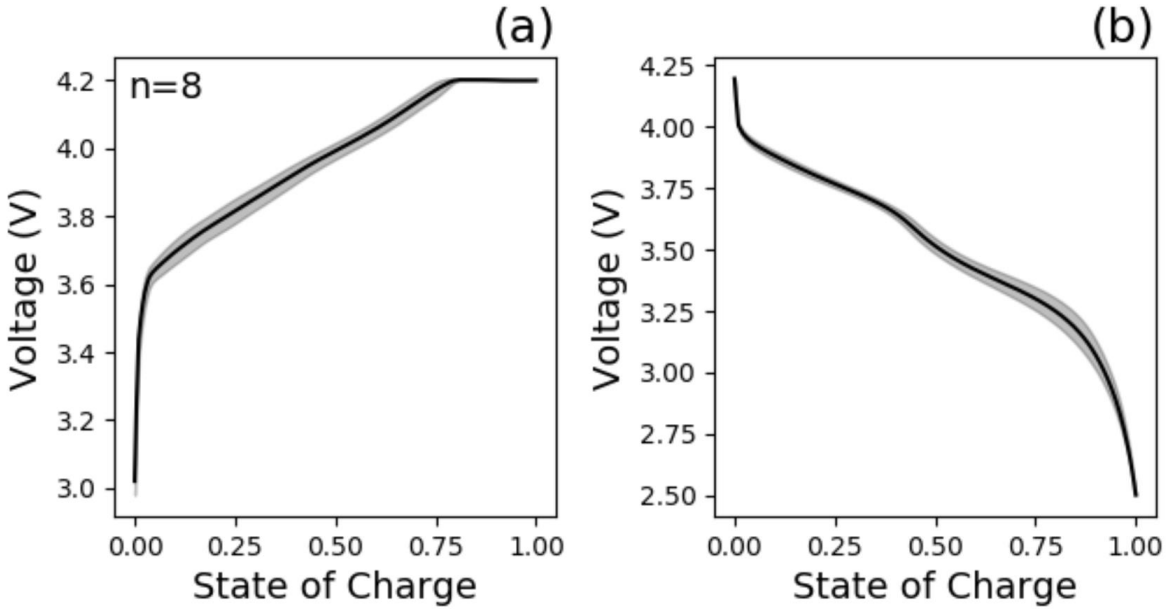

Figure 2.2 Mean values of (a) charge and (b) discharge voltage with SOC at cycle 500 for a replicate group of cells cycled under the 2.67C, 25°C condition. This replicate group consists of 8 cells and the shaded area represents two standard deviations.

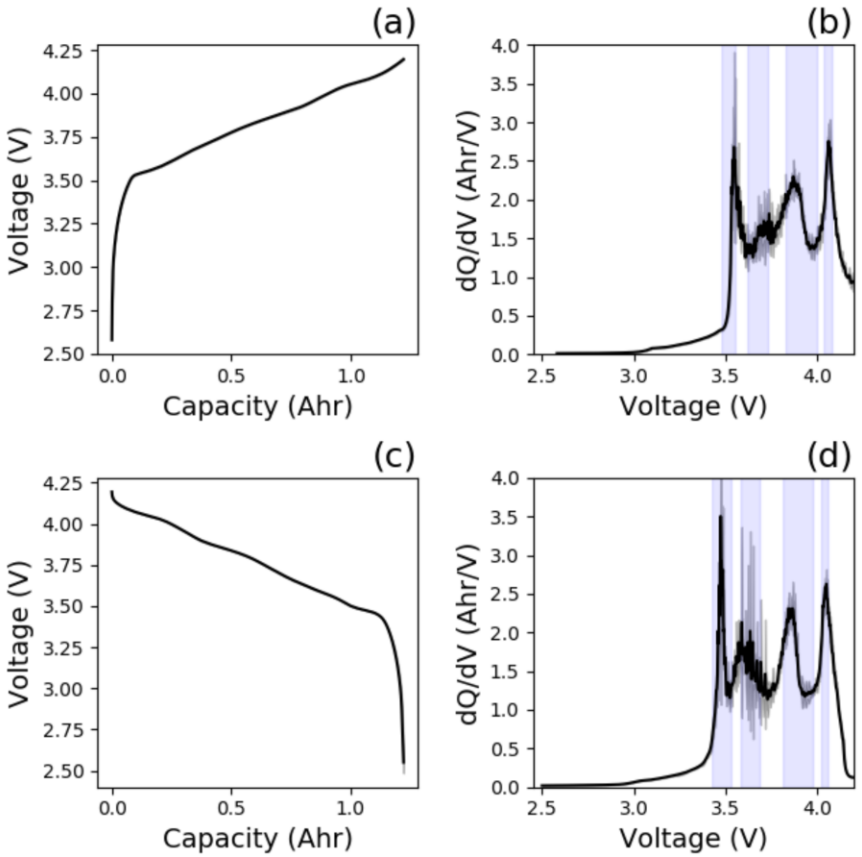

Figure 2.3 Mean values of end-of-testing C/20 constant current (a) charge and (b) discharge voltage curves with capacity for a replicate group of cells cycled under the 2C, 25ºC condition. This group consists of cells 21, 22, and 23, which were all cycled for 1500 cycles. The corresponding mean values of dQ/dV for (c) charge and (d) discharge are calculated from data shown in (a) and (b). All four plots include shaded grey areas that represent two standard deviations. The standard deviations are not noticeable in the voltage curves ((a), (b)); but in the dQ/dV plots ((c),(d)), the standard deviations are large around the peaks, which are highlighted by the vertical bands.

2.3.3 Open circuit voltage and differential capacity analysis (dQ/dV)

A slow C/20 constant current charge and discharge was carried out at the end of cycling for each cell, and the resulting voltage curves can be taken to be the pseudo-OCV. Using the experimental case, 2C and 25°C, which has three replicate cells cycled to 1500 cycles, we show the mean values and two standard deviations for the charge and discharge curves of these three cells in Figure 2.3a and 2.3b. The corresponding differential capacity or dQ/dV plots can then be obtained using techniques described in the Methods section and similarly, the mean and standard deviations of the differential capacities for charge and discharge for these three cells are shown in Figure 2.3c and 2.3d. For the voltage curves, there is little variation in this replicate group of cells; however, for the dQ/dV plots, we see larger standard deviations, especially in the regions around

the peaks, which are highlighted by the vertical bands. This is because very small changes in the voltages, when taking the derivative, can correspond to larger shifts in the peaks or changes in the width of the peaks. The peaks in the dQ/dV represent separate phase transitions and differences in materials composition, construction, and manufacturing can lead to slightly different peak heights and peak locations, leading to variability. Note that the second peak around 3.6V for the dQ/dV discharge in Figure 2.3d has especially noisy data with large variation, which we will explore later.

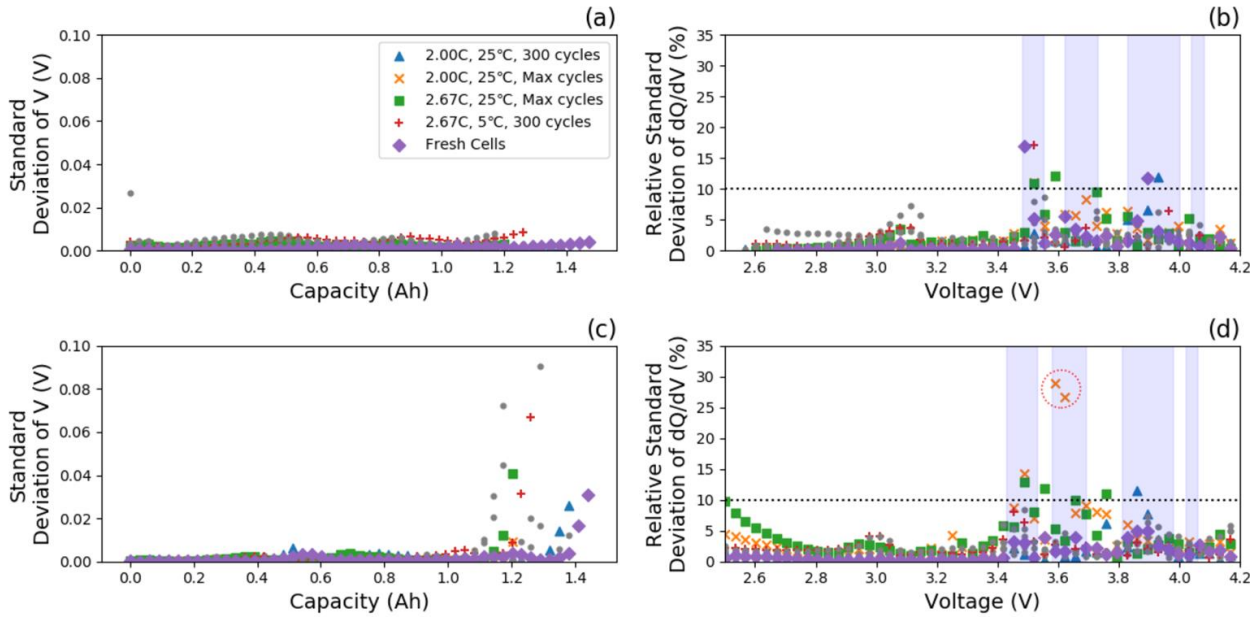

Figure 2.4 For each of the 10 replicate groups, the standard deviation of voltage for the end-of-testing C/20 (a) charge and (b) discharge, and the relative standard deviation for the corresponding dQ/dV during (c) charge and (d) discharge. Replicate groups with any value above a 10% relative standard deviation in (c) and (d) are labeled in the legend and represented by a different set of markers. All other replicate groups with smaller relative standard deviations are represented as grey circles. Vertical bands represent the voltage bands of peaks found in the dQ/dV plots in Figure 3(c),(d), where standard deviation is generally larger.

We can take the standard deviations calculated for each of the four plots in Figure 2.3 and obtain them for all replicate groups. In total, we have 9 replicate groups with sample sizes of three or greater. (In fact, we have 13 replicate groups, two of those only have sample sizes of two cells, and two other groups had cells that did not all end at the same number of cycles and are hence not true replicates.) Since OCV and dQ/dV are only measured at end-of-testing, a replicate group in this case consists of cells that have been cycled under the same conditions and have been cycled for the same number of total cycles. The standard deviations of the OCV for charge and discharge

for all 11 replicate groups are shown in Figure 2.4a and 2.4b, while the relative standard deviations of dQ/dV are shown in Figure 2.4c and 2.4d.

The standard deviation of the voltages is, for the most part, below 10mV, which is a common number used in the community for quantifying voltage fit of model to data. This is true with the exception of the end of discharge (Figure 2.3b), where there is large standard deviation up to ~90mV due to the steep dropoff in voltage at the end of discharge. For the dQ/dV, the relative standard deviations are high around the peaks, indicated by the blue vertical bands. We chose an arbitrary 10% for relative standard deviation as a measure of good data quality for the dQ/dV data. All replicate groups that have any value of relative standard deviation for dQ/dV greater than 10% are labeled in the legend and represented by a different set of markers in Figure 2.4. The remaining replicate groups that have small relative standard deviations are represented as gray circles. Further details on these other replicate groups and their conditions can be found in the Jupyter notebook. We see that the replicate group at 2C, 25°C and cycled to the max number of cycles (1500 cycles, represented by orange crosses) have two points with high relative standard deviation in the discharge dQ/dV of ~25-30% (Figure 2.4d). We can take a deeper look at this replicate group in Figure 2.5.

In Figure 2.5, we show the voltage and dQ/dV data for each of the cells (as opposed to the mean values of the three cells as in Figure 3). We see that Cell 22 (orange line) has a large oscillatory behavior for the second peak around 3.6V for the discharge dQ/dV (Figure 2.5d). Upon further examination, this is due to the oscillatory behavior in the discharge voltage seen in the inset of Figure 2.5b, where we show a zoomed in plot of the voltage. The filtering window that we chose to obtain the dQ/dV (~0.0207 Ah) is of similar length scale as the voltage discrepancies, and thus does not filter out this behavior, instead, taking the derivative amplifies the noise. We could choose to use larger filtering windows to further remove the inherent noise in the data, but larger windows might also remove important features. Here, we show that the reason for the large relative standard deviation of the dQ/dV for this replicate group is due to the underlying voltage measurement that is probably caused by the test equipment. Thus, we have shown how aggregate statistical analysis can be used as a tool to examine specific outliers and as a measure of overall data quality.

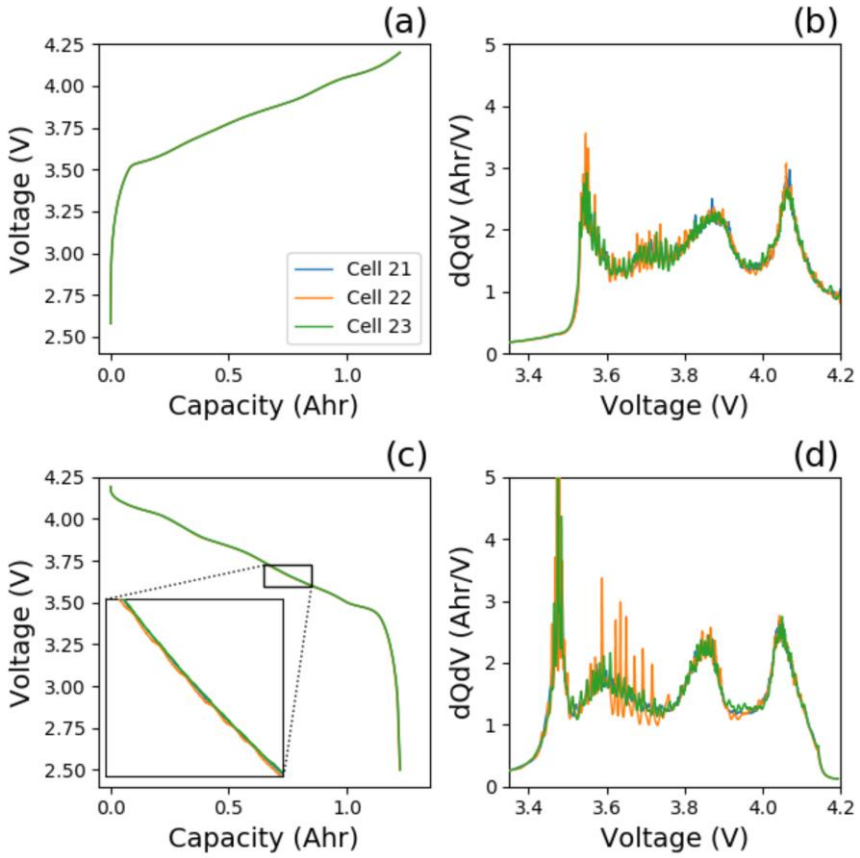

Figure 2.5: End-of-testing C/20 (a) charge and (b) discharge voltage curves for each of the three cells found in the replicate group cycled under the 2C, 25ºC condition, and cycled for 1500 cycles. The inset of (b) shows a zoomed in plot of the voltage, where voltage measurements for cell 22 have an oscillating behavior. This can explain the oscillatory behavior of cell 22's dQ/dV plot for (c) charge and (d) discharge.

2.3.4 Electrochemical impedance spectroscopy (EIS)

For each cell, EIS measurements were carried out at 10%, 30%, and 50% SOCs at the end of cycling. Again, we carry out the same statistical analysis on EIS data for replicate cells. Figure 2.6 is a Nyquist plot of the mean EIS measurement for cells 1-4 at 30% SOC, with the gray shaded area representing two standard deviations from the mean. These four cells have undergone cycling for 300 cycles under 2.67C and 25°C conditions. We observe that the EIS measurements for this replicate group of cells is relatively reproducible with low standard deviation at the high and middle frequencies, and slightly larger standard deviation at the lower frequency tail.

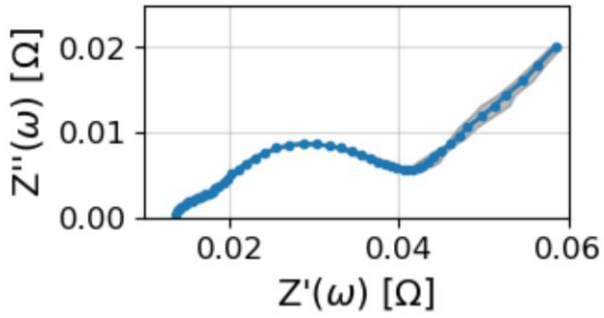

Figure 2.6 Nyquist plot of the mean value of EIS measurements at SOC=30% of cells 1,2,3,4. These cells have undergone cycling for 300 cycles, under 2.67C and 25°C conditions. The shaded grey area represents two standard deviations.

For each of the 9 replicate groups, we can calculate the relative standard deviation at each frequency for both the real and imaginary impedance. This is shown for the EIS measurements at 30% SOC in Figure 2.7. We observe that one replicate group has significantly higher relative standard deviation than all other replicate groups. This replicate group (2C, 25°C, 300 cycles, cells 13-16; plotted as blue squares in Figure 2.7) has higher relative standard deviation for real impedance in the low to middle frequencies, and higher relative standard deviation for imaginary impedance in the middle frequencies. Upon closer inspection, we see that the reason for this large deviation is due to a single cell being an outlier. Figure 2.8 is the Nyquist plot of the EIS of all four cells in the above replicate group at 30% SOC. The impedance for cell 13 is significantly different from cells 14, 15, and 16, hence translating to the large standard deviation of this replicate group. In this manner, aggregated statistical analysis of all EIS spectra collected allows us to easily point out cells that are outliers. Additionally, building a dataset with replicate cells allows us to have confidence in our measurements as the EIS of the other three cells demonstrate high quality reproducibility.

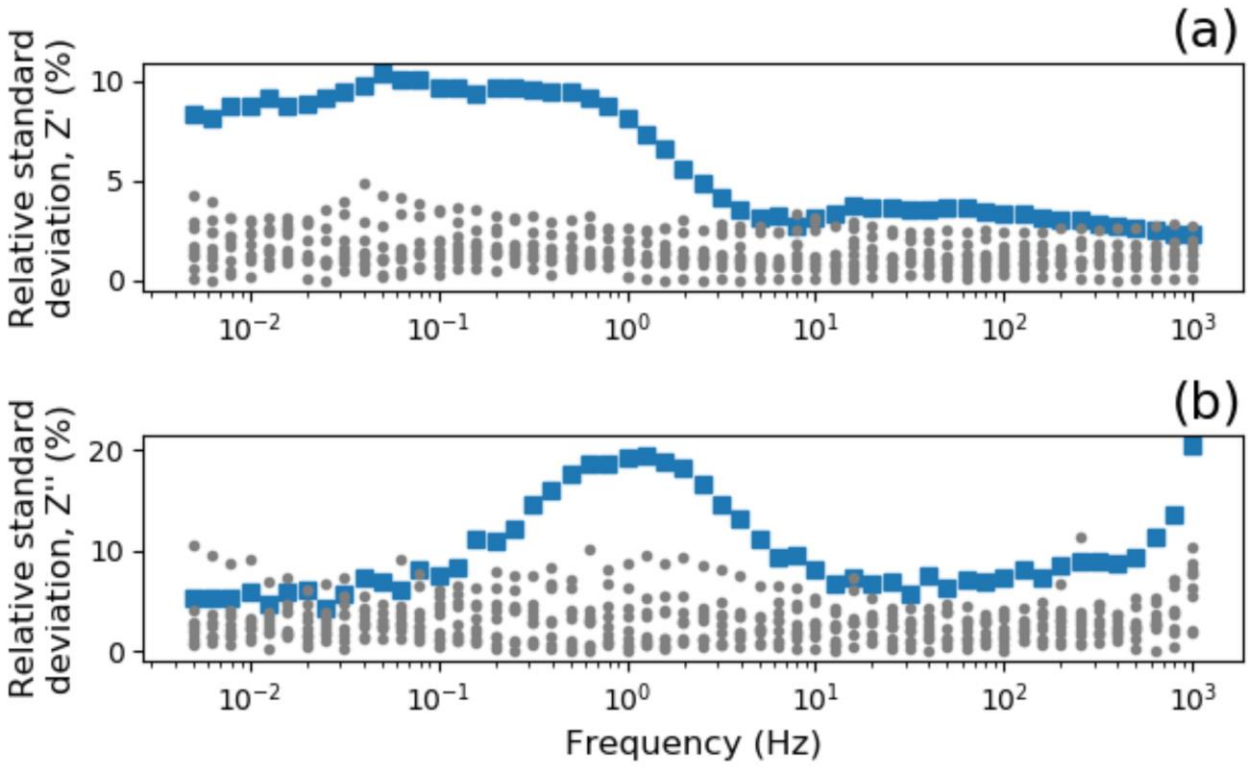

Figure 2.7 The relative standard deviation of the (a) real and (b) imaginary impedance as a function of frequency for each of the 12 replicate groups, for SOC=30%. The blue square markers represent a replicate group that has high relative standard deviation (2C, 25degC, 300 cycles). All other replicate groups with smaller relative standard deviation are plotted as grey circles.

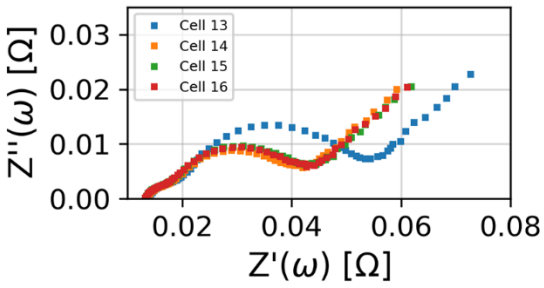

Figure 2.8 Nyquist plot of EIS measurements at SOC=30% for cells 13,14,15,16. This replicate group set (2C, 25°C, 300 cycles) is represented as having high relative standard deviation in Figure 7 as blue square markers.

Finally, validation of collected EIS spectra is also important as discussed in the Methods section. The real and imaginary residual percentage errors from carrying out the linear Kramers-Kronig analysis for all 141 EIS spectra are plotted in Figure 2.9a. Having residuals <2% is

indicative of a valid EIS measurement. Here, we point out two cases with the highest maximum residual errors of 4.63% and 5.02%, which corresponds to the EIS spectra in Figure 2.9bi and 2.9ci respectively, and we can see the residual errors for each frequency in Figure 2.9bii and 2.9cii.

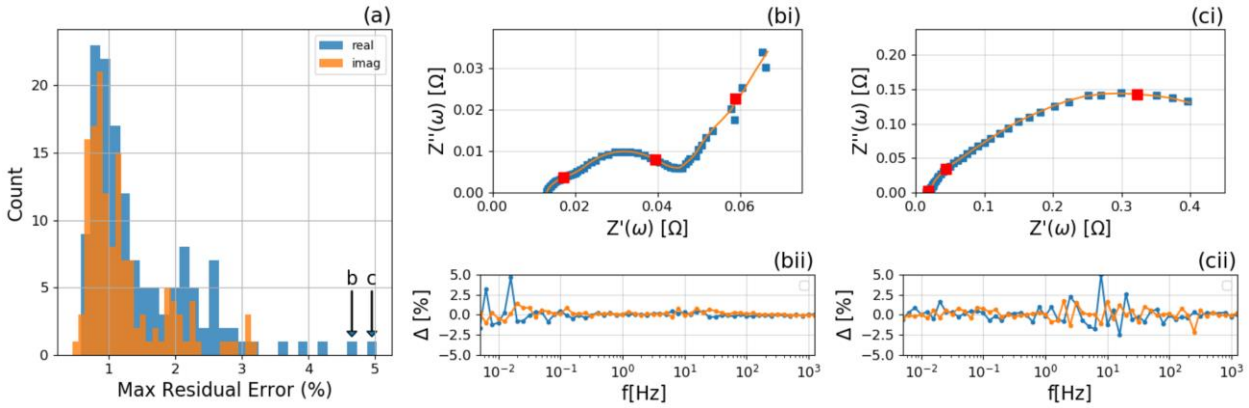

Figure 2.9 (a) Maximum residual percentage errors for real and imaginary values for all 141 collected EIS spectra is shown as a histogram. Nyquist plots of EIS spectra for (bi) cell 33 at SOC=10% and (ci) cell 10 and SOC=30%. Data is shown as blue square markers while the orange line is the fitted result from the Lin-KK model. The corresponding percentage residual error from the fit of real and imaginary data to the Link-KK model at all frequencies is plotted in (bii) and (cii). The highest real residual error shown in (bii) is 4.63%, and in (cii) is 5.02%, which are plotted and indicated by the arrows in (a).

The spectrum in Figure 2.9bi is for cell 33 at 10% SOC which has been cycled for 300 cycles under the 2C, 5°C condition. We observe that there are two residuals of ~2.5% and ~5% at low frequencies (9bii) and this corresponds to the points in the low frequency tail that deviate the most from the smooth fitted line. This means that the measurements at those frequencies might not be valid and violate the conditions required for EIS, but the rest of the spectrum at middle and high frequencies can still be considered as valid. The spectrum in Figure 2.9ci is for cell 10 at 30% SOC which has been cycled for 1500 cycles under the 2.67C, 25°C condition. In this case, there are a few residuals that are relatively high at middle frequencies (~100Hz) with the largest residual being 5.02%. It is more challenging to visualize where these points might deviate from the fitted curve in this scenario, but we can assume, based on the larger residuals, that the measurement is not valid due to the cell being non-stationary for example.

Validation of EIS measurements is important to ensure that any further analysis or interpretation of the data is reliable. Having tools to look at the magnitude and frequencies of the residuals can give us a better idea of data quality and guide data processing. For example, in the

case of cell 33 here (Figure 2.9bi), we might suggest removing the top two residuals while still keeping the data for the rest of the spectrum.

2.4 Conclusions

In this work, we present a dataset that includes cycling data and diagnostic measurements for Li-NMC commercial cells at various C-rates, temperatures, SOHs, and SOCs. The motivation of this dataset is to contribute to the battery open-data community, while also showing the importance of prioritizing replicates in cycling datasets to account for cell variation. Most of the measurements in this study have four replicates for each condition. We highlight the usefulness of using statistical tools to point out outliers and inconsistencies in data quality due to either equipment or experimental measurement error, or cell variability. This is only possible with the inclusion of replicate data and allows us to have more confidence in any trends or interpretations of results from this dataset. Furthermore, we also quantified the variance in these commercial cells for various measurements, and we believe the variance for in-house cells would be higher, which further emphasizes the importance of replicate data to have larger sample sizes for statistically significant conclusions.

All data collected in this study is published on Zenodo, including JSON files that include the metadata suggested by the Battery Genome Project. A supplementary Jupyter Notebook is also available to present the statistical analysis in more detail and the figures presented in this work.

Chapter 3 - Low error estimation of half-cell thermodynamic parameters from whole-cell Li-ion battery experiments: Physics-based model formulation, experimental demonstration, and an open software tool

Note: this chapter was published as an article in the Journal of the Electrochemical Society.[98] *All supporting data and software can be found on Zenodo*[99]

- Hu, V.W.; Schwartz, D. T. *Low Error Estimation of Half-Cell Thermodynamic Parameters from Whole-Cell Li-Ion Battery Experiments: Physics-Based Model Formulation, Experimental Demonstration, and an Open Software Tool*. J. Electrochem. Soc. (2022). https://doi.org/10.1149/1945-7111/ac5a1a
- Hu, V.W.; Schwartz, D.T. https://doi.org/10.5281/zenodo.5847378

Abstract

Low C-rate charge and discharge experiments, plus complementary differential voltage or differential capacity analysis, are among the most common battery characterization methods. Here, we adapt the multi-species, multi-reaction (MSMR) half-cell thermodynamic model to low C-rate cycling of whole-cell Li-ion batteries. MSMR models for the anode and cathode are coupled through whole-cell charge balances and cell-cycling voltage constraint equations, forming the basis for model-based estimation of MSMR half-cell parameters from whole-cell experimental data. Emergent properties of the whole-cell, like slippage of the anode and cathode lithiation windows, are also computed as cells cycle and degrade. A sequential least-square optimization scheme is used for parameter estimation from low-C cycling data of Samsung 18650 NMC|C cells. Low-error fits of the open-circuit cell voltage (e.g., under 5 mV mean absolute error for charge or discharge curves) and differential voltage curves for fresh and aged cells are achieved. We explore the features (and limitations) of using literature reference values for the MSMR half-cell thermodynamic parameters (reducing our whole-cell formulation to a 1-degree-of-freedom fit) and demonstrate the benefits of expanding the degrees of freedom by letting the MSMR parameters be tailored to the cell under test, within a constrained neighborhood of the half-cell reference values. Bootstrap analysis is performed on each dataset to show the robustness of our fitting to experimental noise and data sampling over the course of 600 cell cycles. The results show which specific MSMR insertion reactions are most responsible for capacity loss in each half-cell and the collective interactions that lead to whole-cell slippage and changes in useable capacity. Open-

source software is made available to easily extend this model-based analysis to other labs and battery chemistries.

3.1 Introduction

Widespread electrification of new economic sectors is driving the demand for reliable, safe, and affordable high energy and power-density batteries.[10] To meet this demand, battery materials are continually advancing, separators are getting thinner, the ratio of electrolyte to active material is falling, and ever larger cell formats are being introduced. The reality of these modern battery engineering strategies is that the response of an engineered cell increasingly requires the analysis of two strongly-interacting active electrodes, not a simplified half-cell. Nonetheless, battery science is largely half-cell science carried out in small button cell (CR2032) geometries, providing key properties of pristine active materials without the complicating (but important) implications of a second active electrode microns away.[14–16]

Deconvoluting fundamental physicochemical parameters for each electrode during operation of an engineered whole-cell is critical for understanding device performance, especially aging, but it is fundamentally challenging .[24,26,39,100] The differences between characterizing battery half-cells and whole-cells can be profound: coin cells use excess electrolyte whereas engineered whole-cells are lean on electrolyte; the two classes of cells have different thermal and current distribution behaviors, and it also matters if the whole cell is a cylindrical, pouch, or prismatic configurations under (nominally) identical electrochemical testing.[14,101] One way to extract half-cell electrochemical data from engineered whole-cells is destructive analysis. In this case, the (usually aged) whole-cell is disassembled to harvest electrodes for more traditional half-cell studies and materials analysis, but this introduces uncertainties such as cell compression effects, differences in electrolyte composition and amount, and possible damage to electrode surfaces and pores structure.[102] The alternative is to apply appropriate physics-based modeling to analyze whole-cell measurements, then use sophisticated estimation methods to determine fundamental physicochemical parameters of the half cell.

Here we adapt a half-cell physics-based thermodynamic model, and share open-source software, that can be used to parameterize whole-cell measurements, resulting in low residual error half-cell data. For insertion electrodes, solid-state thermodynamics dictate material phases and reactions that underpin the potential achievable at any given state-of-charge.[27] The thermodynamic open-circuit voltage (OCV) in a battery is the electrochemical potential difference between the anode and the cathode in a common electrolyte.[26] Common experimental techniques to measure

the OCV at different intercalation states involve low C-rate galvanostatic cycling[20,103,104], complementary differential voltage (dV/dQ) or differential capacity (dQ/dV), as well as galvanostatic or potentiostatic intermittent titration techniques.[105,106] Because an engineered whole-cell operates without a reference electrode, OCV vs. state-of-charge data alone is insufficient to estimate potentials of either electrodes against a known thermodynamic reference .[23,38,39] However, we show that whole-cell OCV measurements combined with a physics-based solid-state thermodynamic model that is "seeded" with half-cell parameters referenced to lithium metal, can be used to self-consistently decouple and quantify individual electrode thermodynamic parameters from the whole-cell response. We offer a quantitative approach that goes beyond using half-cell studies as a basis for assigning peaks in whole-cell differential analysis[107–112] , while avoiding destructive postmortem analysis.[37] Whole cell parameter estimation using differential voltage and differential capacity data from aging cells helps understand inhomogeneous material degradation and slippage.[40–42] Open software used for the analysis of engineered whole-cells is provided as a Jupyter notebook.

3.2 Physics-Based Modeling and Parameter Estimation Approach

Thermodynamic model attributes – The Multi-Species, Multi-Reactions (MSMR) model describes the electrochemical thermodynamics of solid-state reactions and phase transitions that insertion materials go through at different lithiation states.[7,49,113] The model has been shown to nicely match experimental half-cell open circuit potential data, and it captures a wide range of solid-state complexity, including phase changes. Because the model has a simple deterministic form with easily interpretable parameters, it can be tuned to explore the effects of parameters on OCP and differential voltage and, as shown here, used in optimization software for robust parameter estimation. Studies of open-circuit and differential voltage spectra of whole-cells typically build from half-cell experimental data and models.[114–116] As a result of having physically interpretable parameters, the MSMR model has been used to gain insight into interfacial resistances in graphite[47,117], interfacial reactions in Li-Si[7], and the effect of scan rate in linear sweep voltammetry experiments[49,113].

Mathematically, the MSMR model describes potential-dependent lithium occupancy of different insertion reactions in a half-cell electrode under study (each reaction is denoted by subscript *j*). To directly align with experimental quantities, we write the MSMR model with

extensive variables, representing the inserted Li^+ charge with Q (Ah units), rather than site occupancy fraction (an intensive variable):

$$Q_j(U) = \frac{Q_{j,tot}}{1+\exp\left[f\left(U-U_j^0\right)/\omega_j\right]} \tag{3.1}$$

and differential capacity

$$\frac{dQ_j}{dU}(U) = -\frac{Q_{j,tot}}{\omega_j}\frac{f\exp[f\left(U-U_j^0\right)/\omega_j]}{[1+\exp[f\left(U-U_j^0\right)/\omega_j]]^2} \tag{3.2}$$

where $f = F/(RT)$, U is the half-cell potential (vs. a lithium metal reference), U_j^0 is the standard potential of any reaction j, and ω_j captures non-ideality associated with intercalation reaction j. Ideal Nernstian behavior is represented by $\omega_j = 1$, whereas attractive interactions in the lithiated solid occurs with $\omega_j < 1$. Strong attractive interactions can represent complex phase behavior such as staging seen in graphite anodes. Alternatively, repulsive interaction occurs with $\omega_j > 1$. Each of the j reactions has a total insertion capacity denoted $Q_{j,tot}$. To calculate the overall insertion capacity and differential capacity of an electrode at any given voltage, the set of independent intercalation reactions are summed over all J reactions that occur in the insertion half-cell:

$$Q(U) = \sum_1^J Q_j(U) \tag{3.3}$$

and

$$\frac{dQ}{dU}(U) = \sum_1^J \frac{dQ_j}{dU}(U) \ . \tag{3.4}$$

The total insertion capacity of all electrode reactions is

$$Q_{tot} = \sum_1^J Q_{j,tot} \ . \tag{3.5}$$

The MSMR half-cell equations work equally well for the typical positive and negative insertion electrodes used in many Li-ion chemistries, and later we add a (+) or (–) superscript to variables and parameters to assign them to a particular electrode in the whole-cell.

Utilizing half-cell models to create a whole-cell response – Qualitatively, the difference between half-cell and whole-cell models is the coupling of charge transfer in each electrode, where incremental insertion in one electrode (δQ) is complemented, ideally, by an equal and opposite

extraction from the other electrode. For safety and durability, this simultaneous insertion/extraction process is bounded by upper and lower whole-cell voltage limits. Consequently, for typical Li-ion chemistries, positive electrodes are cycled between intermediate lithiation states[118], whereas graphite anodes cycle to near their fully-delithiated state. The usable capacity (ΔQ) achieved by cycling between the upper (charged) and lower (discharged) cell voltage limits is lower than the total insertion capacity of either the positive or negative electrode (denoted Q_{tot}^{+} and Q_{tot}^{-} , respectively) as defined in Eq. (3.5).

Mathematically, the relationship between each half-cell's lithiation state at the upper voltage limits can be written

$$V_{upper} = U^{+}(Q_{min}^{+}) - U^{-}(Q_{max}^{-}) \tag{3.6}$$

for a nominally charged cell, and for the lower cell voltage

$$V_{lower} = U^{+}(Q_{max}^{+}) - U^{-}(Q_{min}^{-}) \tag{3.7}$$

in a nominally discharged cell. The superscripts (+) and (–) denote the positive and negative half-cell variables computed from Eqs. (3.1)-(3.5), and the subscripts *max* and *min* describe the maximum and minimum inserted lithium ion in each electrode during a single charge/discharge cycle. The useable charge capacity (ΔQ) of an ideal cell operating between the specified upper and lower voltage bounds is defined by the relationship

$$Q_{max}^{\pm} = Q_{min}^{\pm} + \Delta Q \tag{3.8}$$

for both the positive and negative electrodes. Of course, batteries are not ideal and age over many cycles (by many mechanisms), slowly reducing the useable charge, resulting in a shift of $Q_{max}^{\pm}$ and $Q_{min}^{\pm}$ to simultaneously satisfy the constraints set by Eqs. (3.6)-(3.8) with V_{upper} and V_{lower} fixed. The consequences of loss of capacity, and the resulting "slippage" of the lithiated states for nominally fully-charged and fully-discharged cells have consequences that propagate through the estimation of all parameters in Eqs. (3.1)-(3.8).

Formulating a charge conserving full-cell model to optimize against experimental data – Experimentally, we use standard cell testing methods, namely, low-rate constant current charge and discharge (low C-rate), to determine the equilibrium cell voltage over the accessible range of

lithiation states between the discharged and charged cell. Experimental whole-cell voltages, at any state-of-charge, are represented in model variables as

$$V = U^{+}(Q^{+}) - U^{-}(Q^{-}) \tag{3.9}$$

where the measured voltages are related to state-of-charge in each electrode. Each increment of measured charge (δQ^{exp}) has a concomitant Li-ion insertion/extraction charge, such that $\delta Q^{exp} = \delta Q^{+} = -\delta Q^{-}$ for ideal faradaic efficiency. The differential voltage is also often used as a highly sensitive method for identifying multiple solid-state insertion reactions. With the nomenclature of this work, differential voltage experiments can be represented as:

$$\frac{dV}{dQ} = \frac{dU^{+}(Q^{+})}{dQ} + \frac{dU^{-}(Q^{-})}{dQ} \tag{3.10}$$

with the continuing assumption of ideal faradaic efficiency for a given cycle.

The MSMR model, Eq. (3.1)-(3.5), uses half-cell potential as the independent variable, with extent of solid lithiation as the dependent variable, whereas typical experiments, represented by Eq. (3.9) and (3.10), control lithiation state and measure the resulting voltage. Though the natural independent and dependent variables from modeling and experiments are not identical, both formulations behave well when inverted (since voltage and charge are monotonic functions in Li-ion batteries). Thus, there are several options for formulating the optimization problem when seeking to estimate model parameters against data. As represented in the Jupyter Notebook used for this work[119], we have found robust model fitting to experimental data from minimization of the *Cost* function,

$$Cost = weight_1 \sum_k \frac{\left|\delta Q_k^{exp} - \delta Q_k^{MSMR}\right|}{\langle \delta Q^{exp} \rangle} + weight_2 \sum \frac{\left|\left(\frac{dV}{dQ}\right)_k^{exp} - \left(\frac{dV}{dQ}\right)_k^{MSMR}\right|}{\langle \frac{dV^{exp}}{dQ} \rangle} \tag{3.11}$$

as a function of cell voltage, where the brackets <> denote average values. In initial work, we used 1000 evenly spaced points in voltage to define incremental charge and differential voltage in the experiment and modeled system (even spacing was relaxed in later bootstrap analysis). Moreover, if we assume the experimentally measured useable charge ΔQ^{exp} is ideally related to the modeled insertion/extraction in a given cycle, so that,

$$\Delta Q^{exp} = \Delta Q^{+} = -\Delta Q^{-}\ , \tag{3.12}$$

then we can use Q_{min}^{+} and Q_{min}^{-} as parameters of the model and apply Eq. (3.8) to determine $Q_{max}^{\pm}$ for the positive and negative electrodes. We also constrain our fits by enforcing Eq. (3.6) and (3.7), so that model and experiments agree exactly at the upper and lower cell voltages

$$V_{upper}^{exp} = U^{+}(Q_{min}^{+}) - U^{-}(Q_{max}^{-}) \tag{3.13}$$

and

$$V_{lower}^{exp} = U^{+}(Q_{max}^{+}) - U^{-}(Q_{min}^{-}) \ . \tag{3.14}$$

Finally, if the total positive and negative electrode capacities are known reliably by independent experimental measurements, *i.e.*, Q_{tot}^{exp} is known for both electrodes, then Eq. (3.5) can be used to constrain the modeled values of $Q_{j,tot}$ for each electrode by enforcing an exact match to the experimental values. When doing parameter estimation, we allowed total capacity of both electrodes to be determined by the fit, rather than imposed as a constraint. This choice has several reasons and consequences. First, we are using commercial cells for our experiments, with imprecisely known total active material loading, so it is unclear how accurately we can know Q_{tot}^{exp}. Second, as cells degrade with cycling, the total capacity of each electrode evolves into an unknown, even if there is good data on the fresh cell. Finally, determining the total capacity based on the fit parameters can allow a physics-informed evaluation of the reasonableness of the fitting process.

Seeding initial parameters and establishing physical bounds for parameters. —The procedures for initiating the best-fit of half-cell parameters ($Q_{j.tot}$, U_j^0, ω_j) in fresh cells begins with reference parameters determined by Verbrugge et al.[48] for a variety of cathode and anode materials measured in half-cells. As shown in the Results and Discussion section, the reference parameters give reasonable representations of the carbon and blended NMC/LMO electrodes in our experimental cell, when normalized by an appropriate initial guess for the positive and negative electrode total capacities Q_{tot}, along with enforcement of conditions (3.8), (3.12)-(3.14) at the beginning and end of discharge. Because the MSMR model parameters are physically intuitive and have easily predicted effects on half-cell behavior, we normally make small user adjustments to the reference parameter set to help ensure rapid convergence to low mean absolute error fits of the fresh cell experimental data. Fitting bounds were placed on each type of parameter: U_j^0 was allowed to vary by 20 mV from the initial value; $Q_{j,tot}$ was allowed to vary by 25% of the initial

value, and ω_j was allowed to vary by 25% of the initial value. The one exception was allowing only 5% variation on the $Q_{j,tot}$ parameters for the LMO reactions, to ensure the proportion of NMC to LMO in the blended electrode was close to the value we measured experimentally.

Our implementation of parameter estimation (see Jupyter notebook[119]) involves *Cost* function minimization using *fmin_slsqp*, a sequential least-squares optimization scheme in the Python package SciPy. We evenly weight the *Cost* function between the capacity and differential voltage terms in Eq. (3.11). Our basic procedure is to optimize over 1000 evenly spaced points in voltage over the range of 3.49 V to 4.15 V. This optimization window is less than the lower and upper cell voltage cycling limits (set as $V_{lower} = 2.56\ V$ and $V_{upper} = 4.2\ V$ in the charging experiments described below). By limiting the *Cost* function minimization to this window, the fit focuses on the major features in the differential voltage data, without overly biasing the fit by extreme differential voltages seen at the boundaries of the charging curves. Nonetheless, the full cycling window is part of the optimization through the constraints set by Eqs. (3.8), (3.12) - (3.14), ensuring that the modeled full-cell voltages and usable charge matches the experimental voltages at the beginning (2.56 V) and end (4.2 V) of a charge cycle.

When doing a full parameter estimation, with model parameters U_j^0, $Q_{j,tot}$, and ω_j determined for low C-rate charging of fresh cells, those parameters become the initial guesses for fitting the next dataset after the cells are aged. Here we reevaluated the cells after 300 aggressive cycles. For data from 300 aging cycles (and all subsequent cycles), the tight bounds on LMO capacity parameters are relaxed to match the ±25% bounds on NMC values of $Q_{j,tot}$. Likewise, the best-fit model parameters from 300 cycles become the initial guess for fitting low C-rate testing after 600 total cycles. For the fits of the 600-cycle aged cell, the U_j^0 parameters are bounded within ±10 mV of the values 300 cycle best-fit values.

Because the experimentally measured useable capacity declines during cell cycling, Eqs. (3.8), (3.12)-(3.14) show the fundamental origin of so called "slippage" in Li-ion batteries. Slippage arises naturally when there is model agreement with the experimental voltage constraints and (changing) useable charge values. Here, we allow the minimum inserted lithium in each electrode, Q_{min}^{+} and Q_{min}^{-}, to provide the degrees of freedom that allow the meeting of constraints at the upper and lower voltage bounds of our experimental measurements. For the positive

electrode, we set an upper bound for fitting of Q_{min}^{+} to the value from the last best-fit of data. The lower bound for Q_{min}^{+} is set as if all the measured experimental capacity loss is in slippage of Q_{min}^{+}; the best fit must fall between these physically-reasonable bounds. For the negative electrode, the fitting bounds were set between fully delithiated carbon and 0.5% lithiated carbon (for our fresh cells, that means $0 \leq Q_{min}^{-} \leq 0.0108$ Ahr).

Bootstrapping Analysis.—To further explore the statistical sensitivity of our analysis to details of experimental sampling and noise, we performed a bootstrapping analysis. Instead of using 1000 evenly spaced points within the optimization voltage range, the bootstrapping process takes 1000 random points (out of roughly 6000 for each dataset), and then performs the parameter estimation, repeating the process (with replacement) through 500 iterations. These bootstrapped data are first filtered to remove any fit iterations with differential voltage MAE > 0.04 V/Ahr, as this represented outlier fits that do not accurately capture the features of the datasets. These filtered data are then used to calculate the population mean and confidence interval for each parameter. All data shown in the main body of this manuscript is computed and fit against experimental charging data from the lower voltage limit to the upper voltage limit. In the Supplementary Information, the complementary experimental data for cell discharge, discharge best-fit parameters, and bootstrapped results are presented.

3.3 Experimental Methods

Cycling experiments were performed on commercially available Samsung 1.5 Ahr LiNMC | C cells (INR 18650-15M) using a Maccor 4000M battery cycler in a Maccor MTC-020 environment chamber set at 25°C. All cells were first subjected to five initial cycles with a C/2 charge and discharge rate within the specified voltage windows (2.5 V to 4.2), where the cell capacity stopped increasing. To evaluate cell degradation in these batteries, individual cells were cycled to 300 and 600 cycles, where a full cycle included a 2.67C (4 A) charge to 4.2 V, a constant voltage hold at 4.2 V until current drops to 100 mA, and then a 2.67C discharge down to 2.5 V.

Once the batteries had completed the specified cycling profile, the cells were then discharged at a C/10 rate to 2.5 V. The cells were then subjected to a low galvanostatically controlled (C/20) charge and discharge to estimate the open-circuit voltage data, with data points collected every 10 seconds. To get the differential voltage (dV/dQ), a smoothing filter was applied

for each dataset to reduce differentiation noise and error.[95] A Savitzy-Golay filter with a third-order polynomial was applied around a central voltage with n data points in the window length, resulting in (n – 1)/2 points before and after the central voltage.. The smoothed values at the edges were calculated from the polynomials fit at the first and last central voltages that satisfy the window length. After preliminary evaluation, we selected a value of n = 99 points, resulting in a window with a central voltage that has 49 points before and after so that all the major features of the differential voltage were easily distinguishable, but not overly smoothed.

To estimate the total insertion capacities of the electrodes for the cells under test, we discharged the cells to 0.00 V and then opened the cell casing in a glove box to extract the electrodes and separator. The positive and negative electrode sheets were peeled from the separator and placed into a vacuum oven set at 80°C overnight to remove solvents. Cathode disks were punched from the dried sheet using a 15mm arc punch and weighed. Active material from the cathode was removed using N-methyl-2-pyrrolidone (NMP, Sigma-Aldrich) to reveal the bare current collector, which was then dried overnight in the vacuum oven and weighed. The mass difference between the coated and bare current collector was the weight of the active material, binder, and other additives; standard ratios were used to estimate a total cathode insertion capacity of $Q_{tot}^{+} = 1.8\ Ah$. Anode materials were less reliably measurable, owing to poor adhesion of the coating to the current collector, resulting in material losses when peeled from the separator and when punched. Initial differential voltage analysis measurements indicated that these commercial NMC cells were a blended cathode system, composed of both $N_xM_yC_z$ and spinel MnO_2.[37,120] This was confirmed with X-Ray diffraction (XRD) and energy dispersive X-ray spectroscopy (EDX) along with the composition of the NMC and fractional MnO_2 . Electrode capacities were then estimated from the mass and composition data combined with literature values for published capacities for NMC[9,121–123], and MnO_2,[121,124] along with common formulations for the ratio of active electrode material to binder and additives .

3.4 Results and Discussion

Verbrugge et al., determined MSMR parameters for a wide variety of insertion electrodes based on fits to half-cell experiments. For our cells under test, X-ray diffraction and energy dispersive x-ray analysis showed that the cathode material is a blend of 66% NMC532 and 34% spinel-MnO_2, combined with a graphite anode. Verbrugge et al. have provided best-fit half-cell

parameters for NMC622, LMO, and carbon, and thus, provides a good initial set of thermochemical parameters for our cathode and anode material classes. The MSMR model easily accommodates a blended electrode, since the total capacity is additive at a given potential, per Eqs. (3.1) and (3.5). Consequently, the appropriate reactions for both LMO and NMC were added together, using reaction capacities commensurate with the measured blending ratio, to achieve the half-cell thermodynamics of the cathode.

Implementing the MSMR half-cell model into the whole-cell paradigm.– To illustrate how experimental whole-cell usable charge and voltage constraints, Eqs. (3.8), (3.12)-(3.14) are implement with MSMR half-cell models, we start by describing a single degree of freedom fitting of the model-to-measurements, then successively relax assumptions to achieve a higher degree of freedom best-fit of model-to-measurements.

To reduce the model degrees of freedom, we use the MSMR half-cell thermophysical parameters reported in Verbrugge et al. to represent our blended NMC/LMO (66/34) cathode and graphite anode; this removes all the MSMR model parameters as unknowns (there are six insertion reactions per electrode). Further, we scale the thermophysical parameters with an estimate of total insertion capacity for each electrode, $Q_{tot}^{\pm}$ in the experimental cell under test. Specifically, we estimate the total cathode capacity $Q_{tot}^{+} = 1.8\,Ah$ for our 1.5 *Ah*-rated Samsung cells, based on weighing of the cathode loading in disassembled cells, along with reasonable estimates of binder and other additive masses, as well as specific capacities for the blended cathode materials (200 mAh/g and 120 mAh/g for NMC532 and LMO, respectively), A typical n/p ratio of 1.1 was used to estimate the negative electrode capacity $Q_{tot}^{-} = 1.96\,Ah$.

With these half-cell and cell-under-test parameters estimated through independent means, and not allowed to vary, the whole-cell MSMR model has a single degree of freedom—chosen from among the parameters, Q_{min}^{+}, Q_{max}^{+}, Q_{min}^{-}, Q_{max}^{-}—to fit the measured usable charge (ΔQ*=1.48 Ah*) from C/20 experiment charging from a cell voltage of 2.56 V to 4.2 V. We chose to vary Q_{min}^{+} and used Eqs. (3.8), (3.12)-(3.14), along with the MSMR model (and Verbrugge et al. parameters), to search for a model that matched with whole cell experimental data. It was not known *a priori* whether the highly constraining set of modeling assumptions and estimated values used to reduce the whole-cell MSMR model to a single degree-of-freedom would produce one,

none, or multiple fits to the whole-cell data. Perhaps surprisingly, we found a single value of Q_{min}^{+} for the model that permitted all whole-cell equations (3.8), (3.12)-(3.14) to be satisfied between the experimental voltage window and measured usable charge. The single experimentally-aligned whole-cell fit of the MSMR model parameters is shown in Figure 3.1 as the differential capacity (dQ/dU) for each electrode as a function of the half-cell potential U vs. Li^{+}/Li reference.

Figure 3.1 is a representation of the MSMR model that shows the density of lithiation states in each electrode as a function of potential (against the reference electrode). Filled lithiation states in the blended cathode (red, at more positive potentials) and graphite electrodes (blue, at more negative potentials) are shown as shaded areas in the discharged state with cell voltage of 2.56V, Figure 3.1(a), and the charged state, Figure 1(b), with cell voltage of 4.2V. The quantity of charge extracted from the cathode in going from the lower-to-upper cell voltage matches the experimental usable capacity (1.48 Ah) measured in the fresh Samsung cells. Likewise, the charge inserted into the anode going from the lower-to-upper voltage is equal and opposite to the extracted charge and matches the experiments for a fresh cell. The cell voltage in the discharged and charged states has half-cell potentials at each lithiated state of the electrodes that, when subtracted, exactly match the lower and upper cell voltage bounds used in the experiments. Thus, Eqs. (3.8), (3.12)-(3.14) can be satisfied when we use literature parameters for the MSMR model and our experimental estimates of each electrode's total capacity. Based on the Verbrugge et al. model parameters and whole-cell values described here, we found the minimum lithiation for the positive electrode to be 0.185 Ahr ($Q_{\min}^{+}$) and 0.001 Ahr for the negative electrode ($Q_{\min}^{-}$), with the maximum values simply being 1.48 Ah greater, per Eq. (3.8).

For the blended cathode system, Fig. 3.1 shows that the peaks in the differential capacity are broad, indicative of single-phase reactions. It has been shown that NMC follows this behavior, but the reactions at 4.0 and 4.15 V are typically two-phase reactions caused by the redistribution of the lithium ions in the LMO material. [26,110,125] However purely crystalline, two-phase behavior is hard to maintain for real world applications of LMO, leading the electrode reactions to exhibit more single-phase behavior.[48] In contrast, the differential capacity of the graphite electrode has very sharp peaks, due to the different staging reactions that store a large fraction of capacity over a narrow potential range.[126] These derived differential capacity plots exhibit qualitatively similar

features at the potentials found in half-cell experiments for blended NMC | MnO_2 cathodes and graphite anodes in the literature.[37,120]

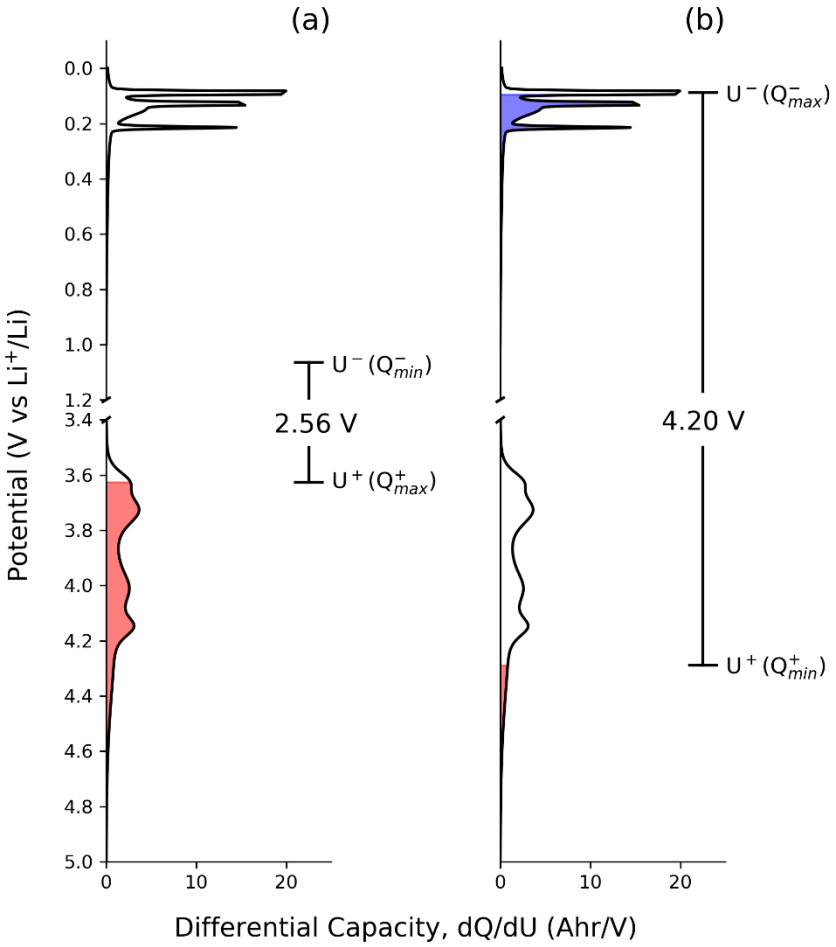

Figure 3.1 Differential capacity of a simulated blended Li NMC | MnO_2 cathode (bottom) and graphite cathode (top) in a discharged (a) and charged (b) state that meets the voltage limit constraints in our experimental data. The shaded portions denote the lithiated capacity in the positive electrode (red) and the negative electrode (blue) at each state of charge. The maximum differential capacity for the anode is more than an order of magnitude larger than the cathode maximum, so anode peaks are cut-off for clarity; this makes it difficult to see that the quantity extracted charge from the cathode exactly equals the inserted charge for the anode in going from (a) to (b).

With this single degree-of-freedom MSMR model fit to the experimentally-measured usable capacity (over the experimentally-prescribed voltage window), and estimated total capacities of each electrode, it now possible to examine experimentally-relevant half-cell and whole-cell responses over the entire range of capacities (state-of-charge) and cell voltages. Figure 3.2(a) shows the whole-cell voltage and half-cell potentials of each electrode as a function of incremental charging (δQ), where the usable state of charge is simply $SOC\ (\%) = \frac{\delta Q}{1.48Ah} * 100\%$

for our fresh cell. At any given cell incremental charge, the whole-cell voltage is the difference between the positive and negative electrode half-cell potentials at the given state of charge. Similarly, Figure 3.2(b) shows the differential voltage and differential half-cell potentials as a function of cell voltage. In this case, the whole-cell differential voltage is the sum of the half-cell potentials at each given cell potential.

Through our single parameter fit, we are assured that the two end-points of the whole cell charging curve, Figure 3.2(a), match experiments. However, none of the intermediate points, nor any of the differential voltages, have been shaped by our experiments. Instead, they represent Verbrugge's half-cell data scaled to our cell. Nonetheless, the whole-cell responses in Figs. 3.2(a) and (b) have all the qualitative features expected from experimental results, with the sharp peaks at 3.5 V and 3.85 V associated with the graphite reactions, and the broader peaks at 3.7 and 4.0 V corresponding to the phase transitions in NMC and LMO, respectively.

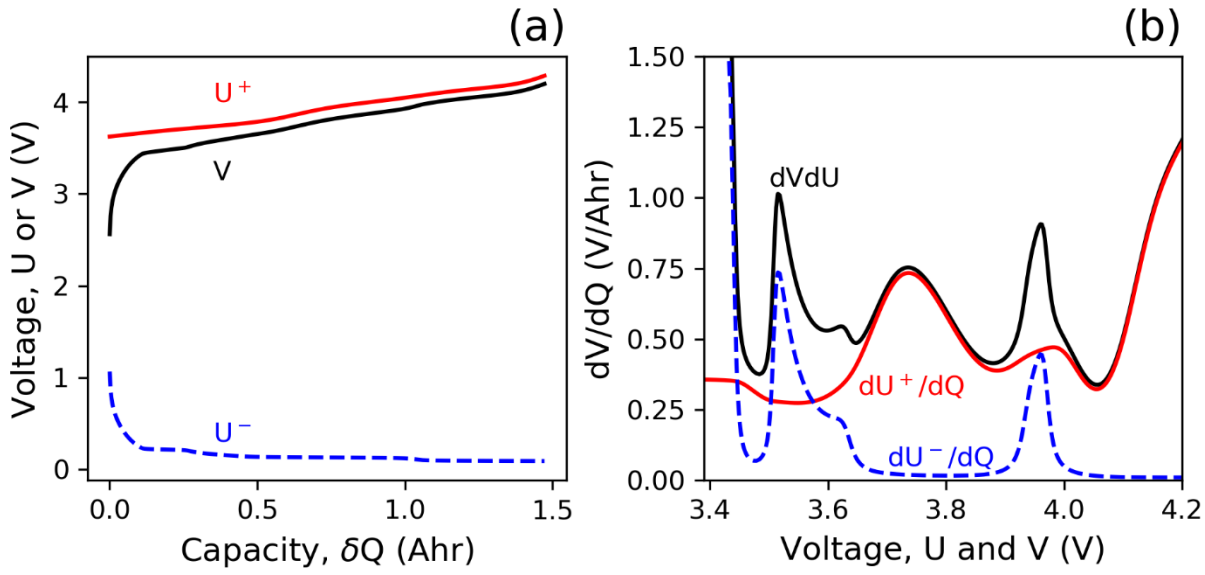

Figure 3.2: Calculated open circuit potentials and cell voltage (a) and differential potentials and voltage (b) from the MSMR model using thermophysical parameters from the literature, scaled to our cells under test. Whole-cell responses in black are the difference and sum of the positive (red) and negative (blue) electrodes for the open-circuit and differential voltage, respectively. For the data shown, whole-cell parameters of electrode capacities, N/P ratios, and lithiation windows were estimated to satisfy Equation (12)-(14).

Adding model degrees-of-freedom for parameter estimation from whole-cell experiments. - The single degree-of-freedom whole-cell model presented in Figs. 3.2(a) and (b) is compared to the experimental dataset for a fresh Samsung cell in Figs. 3.3(a) and 3.3(b). One sees that the data

and model match perfectly at the end points of Fig. 3.3(a), as enforced by our single model parameter-fit that satisfies Equations (3.8), (3.12)-(3.14). Across the whole dataset, the mean absolute error (MAE) between the data and model in Fig. 3.3(a) is 27 mV. Generally, one would like to see a sub-10 mV error between model and fit. Thus, fixing all of Verbrugge et al's parameters (for a NMC 622 composition) does not meet a satisfactory level of fit for this blended NMC 532/LMO cell.

The differences between experimental and modeled differential voltages are more dramatic, as seen in Fig. 3.3(b). While many of the differential voltage peaks are present in both experimental and modeled curves, their locations and relative sizes are quite different. Overall, the MAE for differential voltage is 0.1497 V/Ah between the data and model; the results are clearly an inadequate representation of the experimental cell. One of the attributes of the differential forms of the MSMR model (Eq. (3.2) or its inverse) is that it describes a series of independent insertion reaction "peaks", as in Figure 1, akin to an optical spectrum. In particular, Eq. (3.2) shows that each of the j insertion reactions has an energy centered at U_j^0 , width controlled by ω_j , and integrated size set by $Q_{j,tot}$. Using either a differential capacity or differential voltage formulation, with potential as independent variable, it is fairly intuitive to relax our use of Verbrugge's thermophysical parameters and improve the MAE between experimental and modeled differential voltages. Figures 3.3(c) and (d) show the consequences of manually manipulating the MSMR parameters to better align the same set of MSMR insertion reaction peaks to the data in Fig. 3.3(d), without changing any of whole-cell design parameters (ΔQ, $Q_{min}^{\pm}, Q_{tot}^{\pm}$).

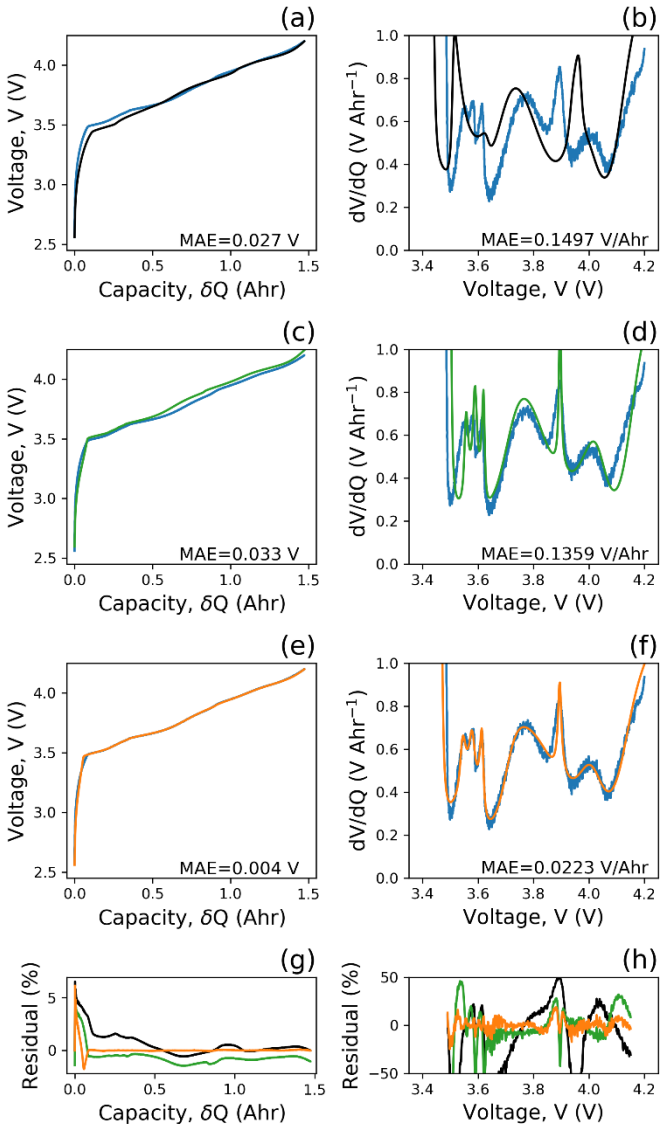

Figure 3.3 Open circuit potential and differential voltage curves of comparing computed to experimental (blue) data, using initial reaction parameters from literature (a, b) (black), manually modified reaction parameters (c, d) (green), and optimized reaction parameters (e, f) (orange), with their reported mean absolute values. The computed residuals (g, h) are being compared to the same experimental data collected from a fresh cell that was charged at a C/20 rate.

A distinct set of modeled features are seen to emerge between Figs. 3.3(b) and 3.3(d) through intuitive manipulations of parameters. In particular, three peaks associated with different graphite staging events can be coaxed from the model over a cell voltage range of 3.5 V to 3.6 V, better matching what is observed experimentally. In the original fits from Verbrugge et al., they noted an inability to capture two small peaks of interest in their experimental data. The parameters involved in the peak emergence included shifting the standard voltages lower, reducing the capacity of these insertion reactions, and decreasing the ω_j to sharpen the peaks of the first four

graphite lithiation reactions. A comparison of Figs. 3.3(b) and (d) also shows that the graphite peak at roughly 4.0 V has been shifted to a lower voltage to better match experiments by adjusting the capacities ($Q_{j,tot}$), so that the phase transition between the last graphite staging reactions occurred earlier in graphite lithiation. Minor adjustments to the standard potentials in the cathode were also made so that the peaks between the model and the experimental data matched better. Qualitatively, these adjusted parameters bring the model much closer into alignment with experimental data, though the quantitative MAE only improves a bit. A consequence of adjusting the reaction parameters and leaving whole-cell design parameters constant is that the voltage limit constraints (V_{upper}^{exp} and V_{lower}^{exp}) are no longer met for the 1.48 Ah charge, as seen in Fig. 3.3(c). Moreover, the MAE in Fig. 3.3(c) increased slightly to 33 mV compared to Fig. 3.3(a), despite the improved peak shapes in Fig. 3.3(d).

In short, while the MSMR model is quite intuitive, it is also very challenging to achieve quantitative whole-cell agreement between experimental data and the model for a full charge curve (or discharge curve, see SI) and associated differential voltage curves, while simultaneously meeting the whole-cell constraints represented by Eqs. (3.8), (3.12)-(3.14). Nonetheless, if we hold the number of insertion reactions per electrode fixed at 6 for the anode and 6 for the cathode, per Verbrugge et al., but allow the thermophysical parameters to be degrees of freedom (with bounds), while also letting $Q_{\min}^{\pm}$ and $Q_{\text{tot}}^{\pm}$ to be emergent properties that must satisfy Eqs. (3.8), (3.12)-(3.14), then we can find low MAE optimal fits and a set of realistic thermophysical parameters for this specific cell, see Figs. 3.3(e) and 3.3(f) and its corresponding parameters in Table 3.3.

Obtaining best-fit parameters starts with the half-cell modeling data given by Verbrugge, et al., (Figs 3.3(a) and (b)), with small adjustments to get key features of the differential voltage curves (Fig. 3.3(c) and (d)). The adjusted half-cell parameters are used as initial guess for fitting the data in Python with the fmin_slsqp (sequential least-squares programming) package in SciPy. The optimization included fitting the differential voltage data between V = 3.49 and V = 4.15 V, with the parameter bounds and voltage limit constraints described in the Methods section. Figures 3.3(e) and 3.3(f) show the whole-cell fully optimized fit to data, with equal weighting in Eq. (3.11). The calculated residual plots for each of the three different parameter sets (Verbrugge et al., tweaked Verbrugge et al., and fully optimized) are displayed as percent difference from the experimental value in Figs. 3.3 (f) and (g). The residuals are calculated as the deviation between

the model and experiment, with the qualitative trends discussed in Figures 3.3(a)-(f) presented quantitatively thru the residuals. One can see the high degree-of-freedom fitting of the MSMR model does an excellent job producing low MAE values in both the voltage and differential analysis results.

Taking the fit parameters and back-calculating the individual half-cell behavior (akin to Fig. 3.2) produces results comparable to half-cell experiments in the literature for these materials. Estimating half-cell potentials from a two-electrode cell, with no reference, can only be known up to an arbitrary constant. However, because the U^0_j parameters we seed our initial estimation with are derived from referenced half-cell measurements by Verbrugge, et al., and are bounded in the fitting process, the best-fit standard potential estimates are anchored to referenced half-cell potentials. Moreover, with six independent reactions in each half-cell, each constrained to within a neighborhood of 25 mV or less of the initial parameter, we expect our systematic uncertainty in any given U^0_j values to be comparable to, or smaller than, the scale of our potential bounds. All parameters for the data in Figure 3.3 are presented in Tables 3.1 – 3.3.

Fitting MSMR model parameters to data for degraded cells – As cells cycle, they degrade, as typically manifested by a declining useable capacity between the fixed upper and lower cell voltage limits. The whole-cell modeling paradigm described above allows one to see the evolution of individual parameters of the model, as well as whole-cell emergent phenomenon associated with satisfying overall charge and voltage constraints, i.e., satisfying Eq. (3.12)-(3.14) as the cell changes. Figure 3.4 shows C/20 charging data and optimized MSMR model fits for a fresh cell, Fig 3.4(a) and (b), a cell cycled 300 cycles at 2C (followed by the C/20 charge that gets fit, per Methods), Fig. 3.4(c) and (d), and a cell cycled 600 times, Fig. 3.4(e) and (f). The 300-cycle cell has a loss of 0.07 Ah of useable capacity (a 4.7% decline), whereas the 600 cycle cell lost 0.12 Ah of useable (an 8.0% decline) compared to the fresh cell over the same voltage window.

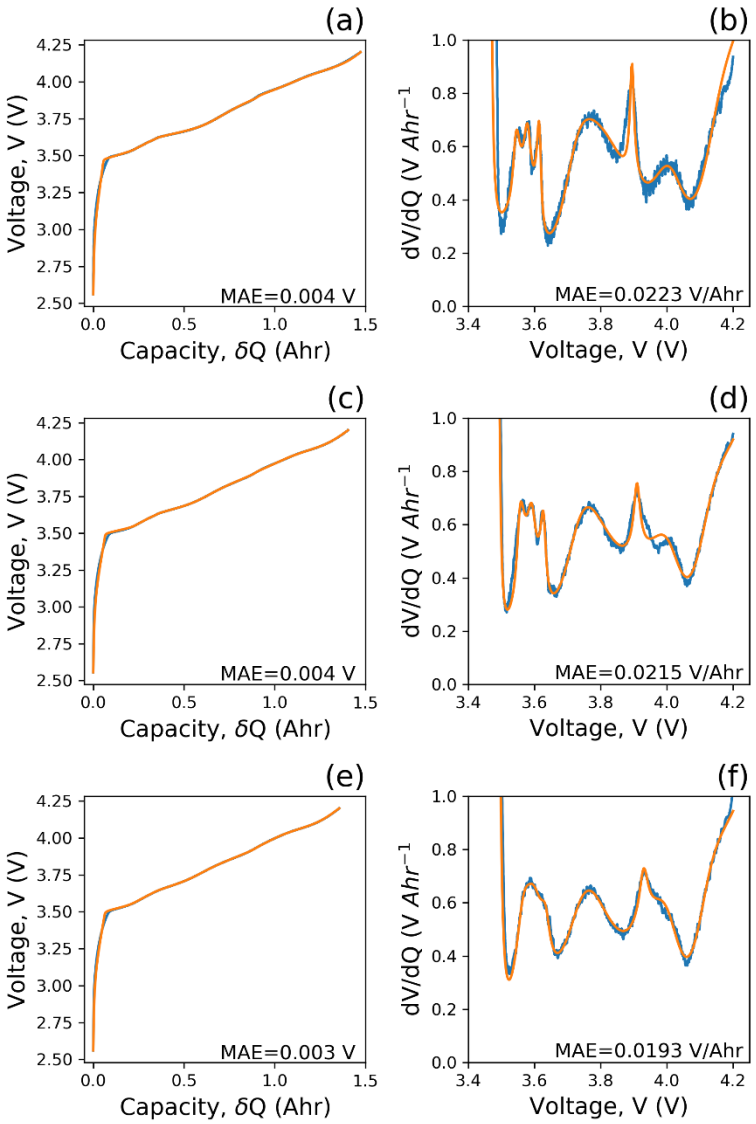

Figure 3.4 Open circuit potential and differential voltage curves of comparing optimized computed (orange) to experimental (blue) data for fresh cells (a, b), cells that have been aged over 300 cycles (c, d), and cells that have been aged over 600 cycles (e, f), with their reported mean absolute values.

The model best-fit for each of the state-of-health condition is shown in Fig 3.4, and the resulting thermophysical parameters are presented in Tables 3.3-3.5. Our fits achieve low MAE between the model and each experimental dataset; replicate cell measurements and fits for each state-of-health can be found in the Supporting Information. Initial guesses for fitting aged datasets are the parameters of the previous (less degraded). Just like the fresh-cell scenario, the optimization

for the aged fits is done between the voltage range of 3.49 V and 4.15 V with equal weighting between the voltage and differential voltage curves.

In all our best-fits, we allow the total capacity of each electrode to be an emergent property of the 6 individual insertion reactions from the electrode, rather than constraining it to a fixed value, like we did in Figs. 3.1 and 3.2 (to reduce degrees of freedom). We find that the positive electrode loses capacity as it is cycled, unlike the negative electrode which remains mostly constant, as shown in Table 3.6.

As the battery degrades, we experimentally observe that the three, distinct graphite peaks at lower voltages begin to lose definition, and eventually coalesce into a single broad peak; this effect is also captured by the MSMR model parameters. We find that the capacity associated with these three early graphite staging insertion reactions is under 15% of the total electrode capacity, consistent with the literature.[41]. As the battery degrades, we see that the graphite peaks are shifting towards higher potentials, with the most prominent peak at 3.88 V merging with the LMO transition peak at 4.0 V, potentially indicative of the positive electrode slipping towards higher potentials. The analysis also shows that a large portion of lithium loss in the positive electrode comes from the voltage range between 3.7 V and 3.8 V. This region involves the transition into a specific rock salt phase, where electrodes with higher nickel content can more easily undergo cation disordering, where lithium and nickel ions can mix, leading to lithium being trapped in the lattice and a nickel ion permanently occupying a lithiation site.[37,127]

Capacity loss can be associated with changes in the solid state insertion electrodes[116,128,129] and/or faradaic inefficiencies.[114] on one electrode or the other. Most forms of degradation lead to slippage in the electrodes, meaning that the utilization window over which the electrodes are cycling shifts as the battery is being degraded. In differential voltage data, these phenomena can lead to an changes in peak heights in the differential voltage and peak location shifts along the voltage axis associated with voltage slippage. [114,36]

Sensitivity of emergent whole-cell properties on model fitting and experimental noise. - State-of-art commercial batteries often have user or testing agreements that forbid opening the cell to measure parameters such as active material loading, material composition and structure, and specific electrochemical parameters. As Figs. 3.3 and 3.4 show, the whole-cell modeling approach

described here appears quite useful for disaggregating half-cell thermodynamic behavior from whole-cell experiments, at least when a suitable reference thermophysical dataset is available. The features of the fit that we label "emergent" are the properties that arise from the need to achieve whole-cell charge and voltage constraints, i.e., the variables in Eqs. (3.8), (3.12)-(3.14). Likewise, we include the calculated total capacity for each electrode, Eq. (3.5), when it emerges from the fit rather than being known from independent experiments. Emergent whole-cell properties are especially important in cell design, especially for understanding the nature of degradation and its impact on safety, for example, through slippage.

We expect emergent whole-cell properties to be especially sensitive to the robustness of the model optimization process to experimental variation such as noise and data sampling strategy. To test this, we performed a bootstrap analysis on the whole-cell datasets by randomly selecting 1000 points from among the roughly 6000 points in each data set (Figs. 3.3 and 3.4 were generated from evenly spaced 1000 points), then replacing and repeating again 500 times. This bootstrap method generates a distribution for every parameter, at every state-of-health tested. The histograms for all these plots can be found in the Supplementary Information. Generally speaking, the bootstrapping results show that the fitting process is quite robust to the noise and spacing of points in our experimental data; the MSMR model converges nicely when the initial physical parameter set is reasonable for the general class of materials being used in the cell. Very few outlier fits were generated.

Figures 3.5-3.7 show the bootstrapped histograms for the emergent whole-cell design parameters, such as the maximum capacities for each electrode, $Q_{tot}^{\pm}$ and the estimated half-cell potentials at the lithiation extremes in each electrode ($Q_{min}^{\pm}$ and $Q_{max}^{\pm}$). For these histograms, we show the distribution of each parameter for 0, 300, and 600 cycles, with black dashed lines demarcating the 90% confidence interval (5^{th} and 95^{th} percentile), and a solid black line denoting the median, or the 50^{th} percentile.

One insight from performing these bootstraps is to compare their results with capacities from the single fit of evenly spaced points (Table 3.6). The single fits suggests that the positive electrode's capacity remains largely constant between 0 and 300 cycles, but there is inherently some uncertainty in our fits that is not captured until we employ more statistically driven methods to

capture that uncertainty. Figure 3.5 shows the histogram of the two electrode capacities, Q_{tot}^{+} and Q_{tot}^{-}, calculated from the summation of their respective $Q_{j,tot}^{\pm}$ for each bootstrap iteration, where we see a systematic shift towards lower positive electrode capacities with aging, whereas the negative electrode narrows into a tightly defined capacity with no significant loss. This behavior is congruent with literature that the positive electrode materials deteriorate at a quicker rate than graphite electrodes, especially more Ni-rich NMCs.[5,129,130] Moreover, when looking at Figure 3.1, it is clear that the high density of states provided by staging in the anode means that the sensitivity of the negative electrode half-cell potential is fixed, so achieving the high voltage constraint equations is largely accomplished by slippage in the positive electrode minimum intercalation state.

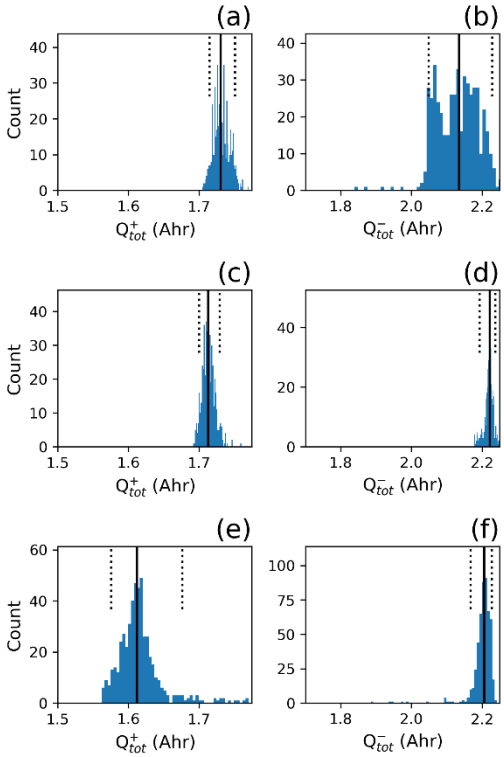

Figure 3.5 Histograms of each Q_{tot}^{+}(left) and Q_{tot}^{-}(right) over the 500 bootstrapped iterations for 0 (a, b), 300 (c, d), and 600 (e, f) cycles datasets. We show the 5th and 95th percentiles of the values demarcated by the dashed black lines and the median by the solid black line. Histograms showing the same parameter are all plotted along the same x-axis for ease for comparison.

Furthermore, to quantify slippage of the materials, we took each set of fit parameters from the bootstrapped iterations and calculated the potentials at the respective $Q_{min}^{\pm}$ *and* $Q_{max}^{\pm}$ that satisfied V_{upper} and V_{lower}. Figure 6 shows the distributions of Q_{min}^{+} and Q_{max}^{-} that satisfy the constraint at

top of charge. Here, we do not detect any appreciable differences in the distributions, and this could be expected. Based on our parameters for the graphite electrode (Table 3.3-3.5), any usable capacity greater than 1.0 Ahr will have the negative electrode in the final reaction, which can store more than half of the total negative electrode capacity over the half-cell potential window of 0.04 to 0.10 V vs Li/Li$^+$. Since the negative electrode capacity does not change appreciably as it is cycled, one finds the half-cell potential one the charged negative electrode does not drift, forcing the positive electrode to also have a nearly constant potential, in order to satisfy whole-cell upper voltage limit of 4.2 V. Examining the capacities Q^+_{max} and Q^-_{min} for the discharged cell, as shown in Figure 3.7, shows that the lower voltage constraint we observe is shifting towards higher potentials as the battery degrades, again, aligning with the literature for this chemistry.[5,114] At the bottom of discharge, the negative electrode is effectively empty, so even minute changes in the capacity could yield large changes in the potential response, whereas the positive electrode is operating in a where an appreciable amount of capacity must be added or removed to induce a potential shift.

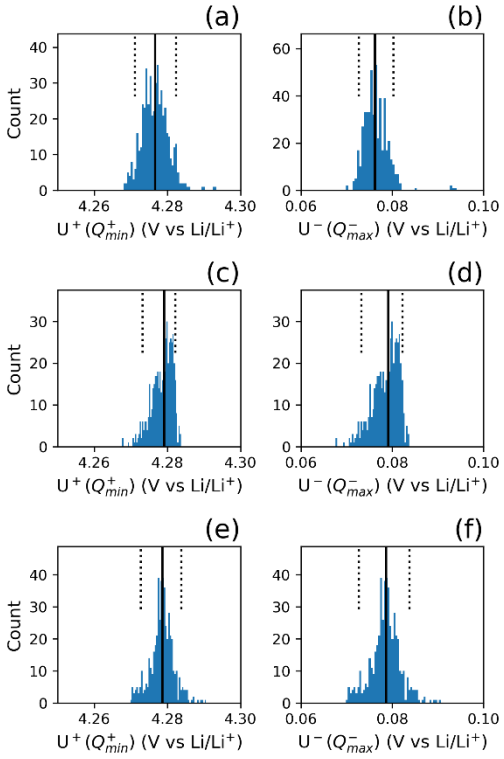

Figure 3.6 Histograms of each $U^+(Q^+_{min})$ (left) and $U^-(Q^-_{max})$ (right) over the 500 bootstrapped iterations for 0 (a, b), 300 (c, d), and 600 (e, f) cycles datasets, where the difference between the two parameters make up the voltage at the top of charge. We show the 5th and 95th percentiles of the values demarcated by the dashed black lines and the median by the solid black line. Histograms showing the same parameter are all plotted along the same x-axis for ease for comparison.

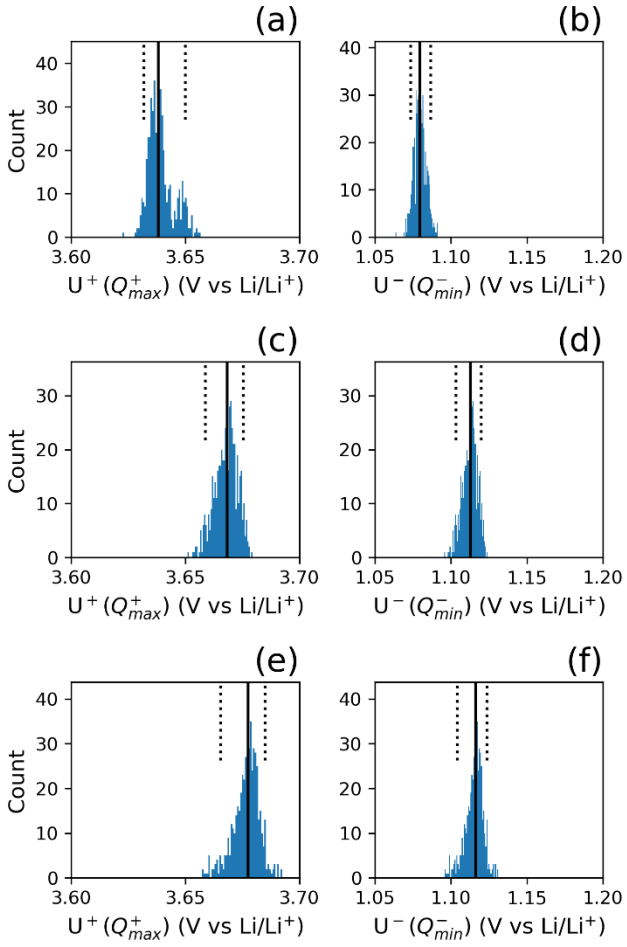

Figure 3.7 Histograms of each $U^{+}(Q^{+}_{max})$ (left) and $U^{-}(Q^{-}_{min})$ (right) over the 500 bootstrapped iterations for 0 (a, b), 300 (c, d), and 600 (e, f) cycles datasets, where the difference between the two parameters make up the voltage at the bottom of discharge. We show the 5th and 95th percentiles of the values demarcated by the dashed black lines and the median by the solid black line. Histograms showing the same parameter are all plotted along the same x-axis for ease for comparison.

Table 3.1 Initial Parameters from Verbrugge et al.

Reaction	U_j^0 (V vs Li/Li)	$Q_{j,tot}$ (Ahr)	ω_j
NMC1	3.623	0.185	0.967
NMC2	3.727	0.446	1.397
NMC3	3.906	0.290	3.505
NMC4	4.230	0.454	5.528
LMO1	4.012	0.234	1.520
LMO2	4.149	0.191	0.930
GRA1	0.088	0.858	0.086
GRA2	0.128	0.475	0.080
GRA3	0.143	0.297	0.725
GRA4	0.170	0.108	2.533
GRA5	0.215	0.134	0.095
GRA6	0.363	0.108	5.974

Table 3.2 Parameters from Manual Manipulation for fitting against fresh-cell data

Reaction	U_j^0 (V vs Li/Li)	$Q_{j,tot}$ (Ahr)	ω_j
NMC1	3.683	0.185	0.967
NMC2	3.727	0.446	1.397
NMC3	3.906	0.290	3.505
NMC4	4.261	0.454	5.528
LMO1	4.012	0.234	1.520
LMO2	4.169	0.191	0.930
GRA1	0.075	1.131	0.086
GRA2	0.103	0.504	0.080
GRA3	0.124	0.049	0.150
GRA4	0.146	0.054	0.175
GRA5	0.169	0.134	0.122
GRA6	0.363	0.108	5.974

Table 3.3 Parameters from optimization for fresh cell data

Reaction	U_j^0 (V vs Li/Li)	$Q_{j,tot}$ (Ahr)	ω_j
NMC1	3.663	0.231	0.725
NMC2	3.746	0.407	1.072
NMC3	3.888	0.306	2.656
NMC4	4.262	0.392	4.146
LMO1	4.019	0.222	1.472
LMO2	4.153	0.181	1.118
GRA1	0.077	1.251	0.108
GRA2	0.108	0.549	0.100
GRA3	0.132	0.061	0.185
GRA4	0.154	0.061	0.219
GRA5	0.177	0.165	0.152
GRA6	0.343	0.081	6.828

Table 3.4 Parameters from optimization for fitting 300 cycles aged cell data

Reaction	U_j^0 (V vs Li/Li)	$Q_{j,tot}$ (Ahr)	ω_j
NMC1	3.683	0.289	0.544
NMC2	3.749	0.413	1.254
NMC3	3.908	0.260	2.560
NMC4	4.242	0.429	3.896
LMO1	4.001	0.226	1.840
LMO2	4.137	0.136	0.948
GRA1	0.071	1.269	0.135
GRA2	0.104	0.536	0.125
GRA3	0.129	0.054	0.182
GRA4	0.151	0.066	0.273
GRA5	0.178	0.158	0.170
GRA6	0.323	0.099	6.818

Table 3.5 Parameters from optimization for fitting 600 cycles aged cell data

Reaction	U_j^0 (V vs Li/Li)	$Q_{j,tot}$ (Ahr)	ω_j
NMC1	3.692	0.217	0.408
NMC2	3.759	0.392	1.398
NMC3	3.918	0.221	2.452
NMC4	4.232	0.426	3.858
LMO1	3.991	0.225	1.763
LMO2	4.134	0.140	0.896
GRA1	0.068	1.266	0.168
GRA2	0.106	0.538	0.151
GRA3	0.129	0.054	0.228
GRA4	0.149	0.081	0.342
GRA5	0.175	0.148	0.213
GRA6	0.313	0.093	6.652

Table 3.6 Capacity of electrodes from fits

Cycles	Q_{tot}^{+} (Ahr)	Q_{tot}^{-} (Ahr)
0	1.740	2.168
300	1.753	2.181
600	1.619	2.180

3.5 Conclusion and Implications

Battery degradation intrinsically is extremely complex, as there are several physical and chemical phenomena that can occur, resulting in electrode imbalance, electrode deformation and degradation, and other modes of loss of lithium inventory. Using open-circuit potential data in conjunction with differential voltage data can be powerful tools in noninvasively probing these phenomena in fully assembled commercial batteries. While teardown, postmortem analyses, and reassembly of half cells can provide useful insight into the electrode properties and capacity loadings, it is not always feasible or allowed. Here, we extend the easy, generalizable mathematics laid out by the MSMR model to include cell design parameters and the thermodynamic relationships of the two electrodes to allow for the modeling of whole cells. This gives us the unique advantage of interpreting the evolution of fundamental reactions and transitions of each electrode, information that is often only extractable from separate half-cell and crystallography studies.

We show that by employing the thermodynamics framework in the MSMR model, we can fit experimental thermodynamic data with low errors, allowing us to extract information about the degradative states of the electrodes without having to perform postmortem testing. Using the MSMR model, we can identify the specific reactions of the NMC, LMO, and the graphite electrodes that are degrading as the cell ages, and how those losses of capacity and deviations from their original one or two-phase behavior affects the resulting thermodynamic response. It is conceivable to perform crystallography experiments in operando to confirm the compositions of each of these phases in cathode materials, to test the validity of the ability of this model to predict how these phase transitions evolve over aging so that future experiments may not need XRD or time-intensive synchrotron experiments. Furthermore, this work strictly focuses on the thermodynamics of the MSMR model, but the framework has been established by Baker et al., to use these principles to model transport and kinetic phenomena, allowing for incredible, fundamental insight opportunities.[49,113]

This present work is aiming to provide the community with a user-friendly tool that allows researchers to gain insights into state-of-health of their cells without having to perform half-cell studies from postmortem procedures. Instead, researchers can utilize a base knowledge of the battery chemistry and the parameters that Verbrugge et al. have published for a variety of electrodes.[48] It is important to reiterate though, that in the absence of teardown and half-cell data. the MSMR model yields an inherent uncertainty since the total capacities nor the true open-circuit potentials are known. Additionally, the MSMR model assumes that all reactions are occurring in a uniform electrode, which does not always hold true for degraded electrodes where there could be inhomogeneous particle sizes, cracks, and deformations, which is why we allow for flexibility in the standard potentials to help account for some of these variations. All the data files, code, and instructions on how to use this tool are available on GitHub and Zenodo.[99]

3.6 Appendix – Supplementary Information

In Figures 3.7 and 3.8, we show the conventional voltage as a function of capacity and differential voltage as a function of voltage for the separate charge and discharge C/20 constant-current experiments. The charge step (Fig. 3.7) begins after a short rest step, allowing the voltage to relax to a point slightly above 2.5 V and ends at 4.2 V. The discharge step (Fig. 3.8) begins immediately after the C/20 charge step and ends at 2.5 V, allowing the discharge step to span the

entirety of the voltage window. While the usable capacities (δQ, 1.473 Ahr and 1.471 Ahr for charge and discharge, respectively) and their voltage profiles are similar, we can see distinct differences in the different voltages. Due to hysteresis between charge and discharge profiles, the central voltages for each corresponding peak are shifted. Significant differences can be seen at the peaks between 3.5 and 3.65 V, which are all similar magnitudes in the charged step, with the peaks roughly round 0.7 V/Ahr, but these same corresponding peaks are all of much bigger variations in the discharge step. We also see the sharp peak, centered at about 3.9 V in the charge step, decrease in magnitude with aging, whereas that corresponding peak in the discharge curves grows with aging.

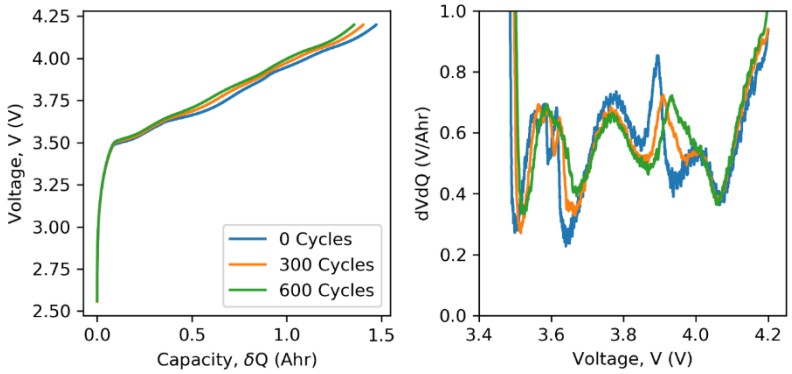

Figure 3.8 Open circuit potential and differential voltage spectra for Samsung 18650 LiNMC|Graphite Cells after 0, 300, and 600 cycles. All data were collected using a C/20 charge rate between the voltage limits of 2.5 and 4.2 V.

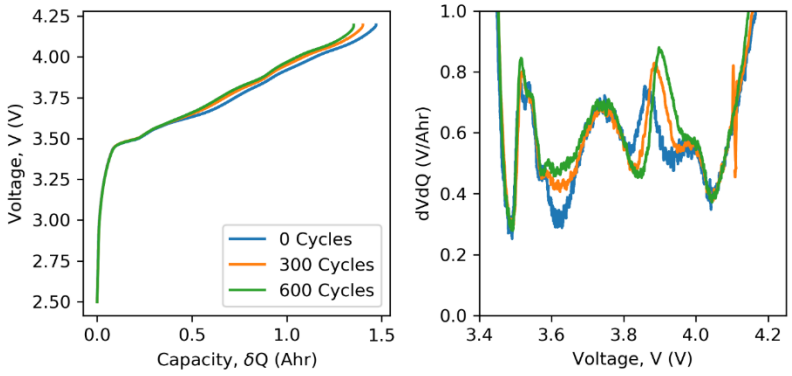

Figure 3.9 Open circuit potential and differential voltage spectra for Samsung 18650 LiNMC|Graphite Cells after 0, 300, and 600 cycles. All data were collected using a C/20 discharge rate between the voltage limits of 2.5 and 4.2 V.

Included in Tables 3.7 through 3.9 also are the deviations of each parameter from each of the charged fits against experimental data from the base parameters from Verbrugge et., al. We can expect some deviations in our parameters, as the materials that are used in our commercial batteries can be constructed with different materials (i.e. NMC622 vs NMC532) and different formulations.

Table 3.7 Changes in the parameters between literature and the 0-cycle fit for charging data.

Reaction	U_j^0 (V vs Li/Li$^+$)	$Q_{tot,j}$ (Ahr)	ω_j
NMC1	-0.040	-0.046	0.242
NMC2	-0.019	0.039	0.325
NMC3	0.018	-0.016	0.849
NMC4	-0.032	0.062	1.382
LMO1	-0.007	0.012	0.048
LMO2	-0.004	0.010	-0.188
GRA1	0.011	-0.393	-0.022
GRA2	0.020	-0.074	-0.020
GRA3	0.011	0.236	0.540
GRA4	0.016	0.047	2.314
GRA5	0.038	-0.031	-0.057
GRA6	0.020	0.027	-0.854

Table 3.8 Changes in the parameters between literature and the 300-cycle fit.

Reaction	U_j^0 (V vs Li/Li$^+$)	$Q_{tot,j}$ (Ahr)	ω_j
NMC1	-0.060	-0.104	0.423
NMC2	-0.022	0.033	0.143
NMC3	-0.002	0.030	0.945
NMC4	-0.012	0.025	1.632
LMO1	0.011	0.008	-0.320
LMO2	0.012	0.055	-0.018
GRA1	0.017	-0.411	-0.049
GRA2	0.024	-0.061	-0.045
GRA3	0.014	0.243	0.543
GRA4	0.019	0.042	2.260
GRA5	0.037	-0.024	-0.075
GRA6	0.040	0.009	-0.844

Table 3.9 Changes in the parameters between literature and the 600-cycle fit.

Reaction	U_j^0 (V vs Li/Li$^+$)	$Q_{tot,j}$ (Ahr)	ω_j
NMC1	-0.069	-0.032	0.559
NMC2	-0.032	0.054	-0.001
NMC3	-0.012	0.069	1.053
NMC4	-0.002	0.028	1.670
LMO1	0.021	0.009	-0.243
LMO2	0.015	0.051	0.034
GRA1	0.020	-0.408	-0.082
GRA2	0.022	-0.063	-0.071
GRA3	0.014	0.243	0.497
GRA4	0.021	0.027	2.191
GRA5	0.040	-0.014	-0.118
GRA6	0.050	0.015	-0.678

In Figures 3.10 to 3.12, we show the reproducibility of our data and the MSMR fitting routine. In Figure 3.10 to 3.12, we show the results of the fits for the 4 replicates at 0 cycles, 4 replicates at 300 cycles, and 2 replicates at 600 cycles, respectively. All four 300-cycle fits were seeded with the fitting results of the same 0-cycle fit (Cell 51) from the main manuscript, and both 600-cycle fits were seeded with the fitting results of the same 300-cycle fit (Cell 1) as well. All fits were done using an equal weight of the capacity-voltage and the differential voltage curves. The means and the standard deviations of each parameter for each replicate set are shown in Tables 3.10-3.12.

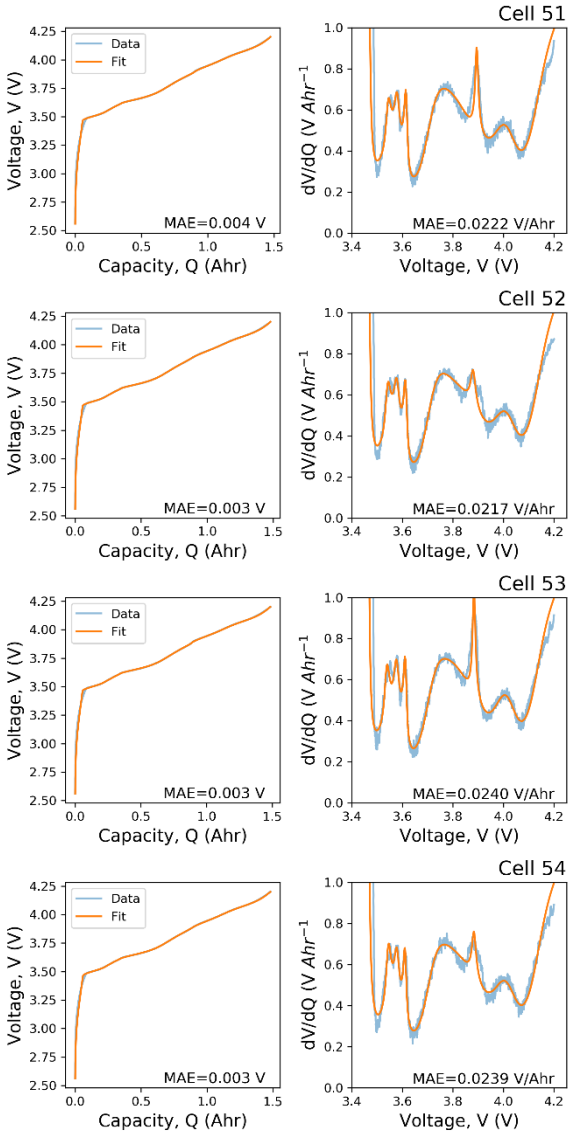

Figure 3.10 Open circuit potential and differential voltage curves of four replicate cells at 0 cycles comparing computed (orange) to experimental (blue) data, using the same initial guess from the manually modified reaction parameters with their reported mean absolute values. Cells that were charged at a C/20 rate.

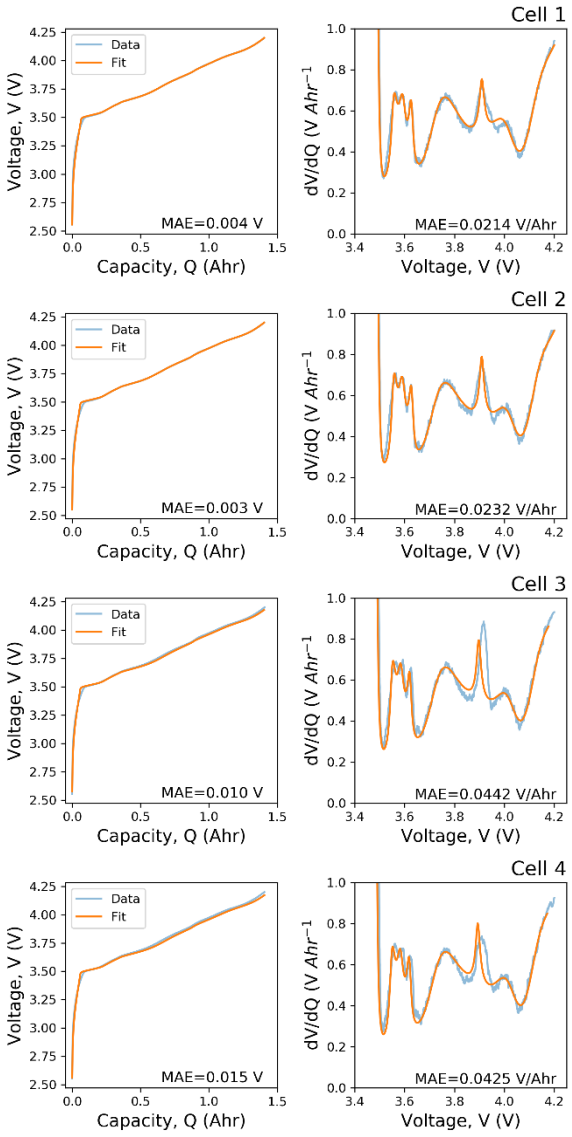

Figure 3.11 Open circuit potential and differential voltage curves of four replicate cells at 300 cycles comparing computed (orange) to experimental (blue) data, using the same initial guess from the resultant 0 cycle fit of cell 51, with their reported mean absolute values. Cells that were charged at a C/20 rate.

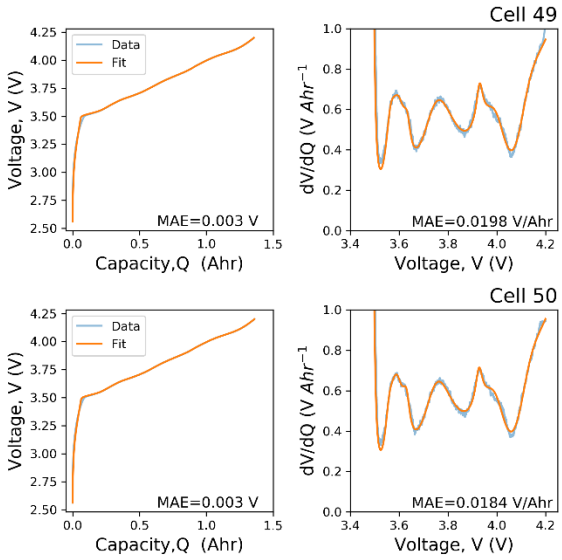

Figure 3.12 Open circuit potential and differential voltage curves of two replicate cells at 600 cycles comparing computed (orange) to experimental (blue) data, using the same initial guess from the resultant 300 cycle fit of cell 1, with their reported mean absolute values. Cells that were charged at a C/20 rate.

Table 3.10 Mean and standard deviations for fitting against all replicates of the fresh-cell charge data

Reaction	U_j^0 (V vs Li/Li$^+$)	$Q_{tot,j}$ (Ahr)	ω_j
NMC1	3.6629 +/- 0.0002	0.2290 +/- 0.0034	0.7253 +/- 0.0000
NMC2	3.7464 +/- 0.0001	0.3964 +/- 0.0140	1.0541 +/- 0.0104
NMC3	3.8880 +/- 0.0026	0.3121 +/- 0.0037	2.6373 +/- 0.0110
NMC4	4.2640 +/- 0.0037	0.3888 +/- 0.0047	4.1457 +/- 0.0000
LMO1	4.0215 +/- 0.0028	0.2223 +/- 0.0000	1.4752 +/- 0.0611
LMO2	4.1538 +/- 0.0020	0.1814 +/- 0.0000	1.1119 +/- 0.0130
GRA1	0.0780 +/- 0.0017	1.2178 +/- 0.0295	0.1076 +/- 0.0000
GRA2	0.1067 +/- 0.0013	0.5395 +/- 0.0076	0.0992 +/- 0.0014
GRA3	0.1346 +/- 0.0056	0.0594 +/- 0.0018	0.1869 +/- 0.0010
GRA4	0.1468 +/- 0.0118	0.0608 +/- 0.0048	0.2002 +/- 0.0322
GRA5	0.1746 +/- 0.0042	0.1621 +/- 0.0043	0.1499 +/- 0.0026
GRA6	0.3433 +/- 0.0000	0.0817 +/- 0.0006	6.7160 +/- 0.1305

Table 3.11 Mean and standard deviations for fitting against all replicates of the fresh-cell charge data

Reaction	U_j^0 (V vs Li/Li$^+$)	$Q_{tot,j}$ (Ahr)	ω_j
NMC1	3.6825 +/- 0.0009	0.2888 +/- 0.0000	0.5440 +/- 0.0000
NMC2	3.7502 +/- 0.0058	0.4101 +/- 0.0403	1.2320 +/- 0.0676
NMC3	3.9084 +/- 0.0000	0.2759 +/- 0.0169	2.4960 +/- 0.0928
NMC4	4.2520 +/- 0.0113	0.3859 +/- 0.0407	3.5416 +/- 0.4358
LMO1	4.0117 +/- 0.0066	0.2453 +/- 0.0192	1.8397 +/- 0.0006
LMO2	4.1395 +/- 0.0022	0.1361 +/- 0.0000	0.9375 +/- 0.0190
GRA1	0.0699 +/- 0.0021	1.2921 +/- 0.0285	0.1345 +/- 0.0000
GRA2	0.1048 +/- 0.0024	0.5366 +/- 0.0072	0.1251 +/- 0.0000
GRA3	0.1298 +/- 0.0019	0.0541 +/- 0.0042	0.1794 +/- 0.0224
GRA4	0.1515 +/- 0.0008	0.0670 +/- 0.0061	0.2734 +/- 0.0000
GRA5	0.1784 +/- 0.0007	0.1546 +/- 0.0067	0.1632 +/- 0.0120
GRA6	0.3299 +/- 0.0115	0.0972 +/- 0.0043	6.7951 +/- 0.0216

Table 3.12 Mean and standard deviations for fitting against all replicates of the fresh-cell charge data

Reaction	U_j^0 (V vs Li/Li$^+$)	$Q_{tot,j}$ (Ahr)	ω_j
NMC1	3.6919 +/- 0.0002	0.2166 +/- 0.0000	0.4080 +/- 0.0000
NMC2	3.7592 +/- 0.0000	0.3951 +/- 0.0035	1.4026 +/- 0.0046
NMC3	3.9184 +/- 0.0000	0.2081 +/- 0.0129	2.2499 +/- 0.2022
NMC4	4.2321 +/- 0.0001	0.4163 +/- 0.0092	3.7999 +/- 0.0578
LMO1	3.9910 +/- 0.0000	0.2273 +/- 0.0024	1.7642 +/- 0.0016
LMO2	4.1318 +/- 0.0021	0.1462 +/- 0.0067	0.9224 +/- 0.0260
GRA1	0.0666 +/- 0.0017	1.2662 +/- 0.0003	0.1682 +/- 0.0000
GRA2	0.1045 +/- 0.0017	0.5405 +/- 0.0025	0.1539 +/- 0.0025
GRA3	0.1286 +/- 0.0008	0.0561 +/- 0.0020	0.2278 +/- 0.0000
GRA4	0.1491 +/- 0.0002	0.0794 +/- 0.0019	0.3418 +/- 0.0000
GRA5	0.1739 +/- 0.001	0.1420 +/- 0.0056	0.2127 +/- 0.0000
GRA6	0.3132 +/- 0.0000	0.0943 +/- 0.0017	6.5731 +/- 0.0791

We also show the shift in each parameter in both the positive (Fig 3.13) and the negative (Fig 3.14) electrode as a function of cycles for the main fits shown in the main text (Fig 3.4). The cells' fits that are represented at cells 51 (0 cycles) , 1 (300 cycles), and 49 (600 cycles). Here, we show how the differential capacity for each reaction changes that sum into the total dQ/dV response.

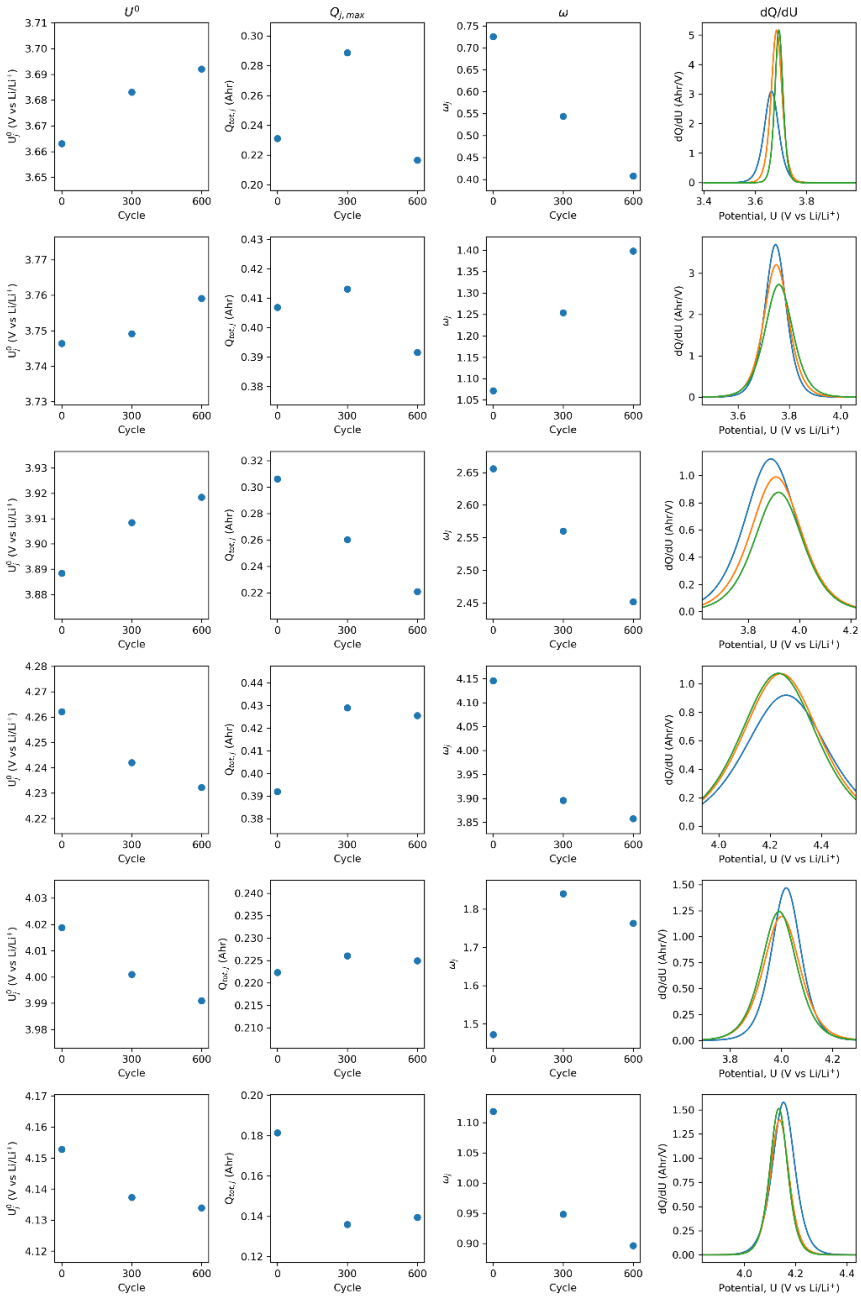

Figure 3.13 Comparison of the fit positive electrode parameters at 0, 300, and 600 cycles, with the first three columns showing, for each reaction, the standard electrode potential (U_j^0) maximum capacity ($Q_{tot,j}$), and the ω_j factor, respectively. The fourth column is the calculated dQ/dV peak for each reaction at each point in cycling (0 – blue, orange – 300, green – 600).

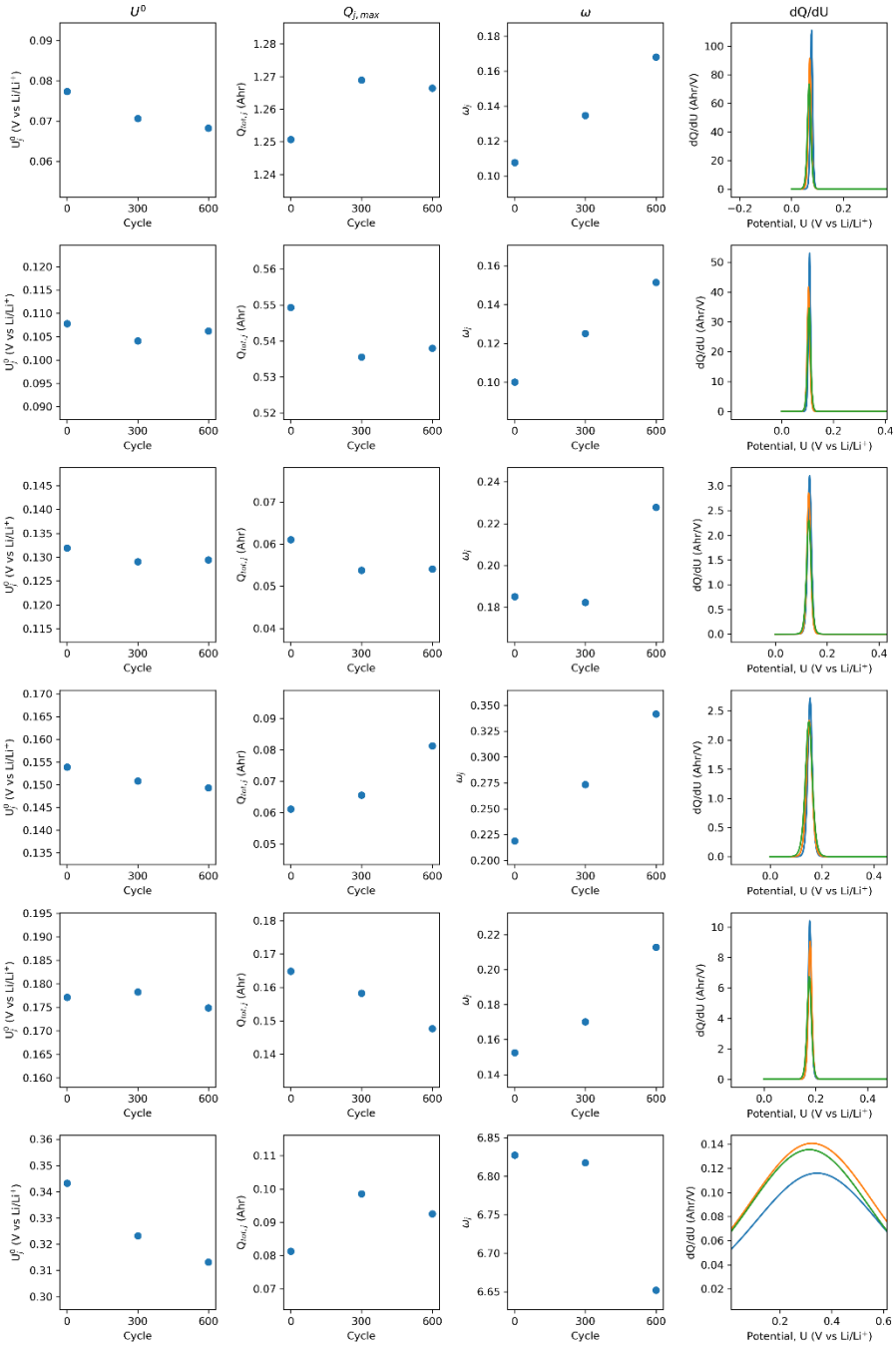

Figure 3.14 Comparison of the fit negative electrode parameters at 0, 300, and 600 cycles, with the first three columns showing, for each reaction, the standard electrode potential (U_j^0) maximum capacity ($Q_{j,max}$), and the ω_j factor, respectively. The fourth column is the calculated dQ/dU peak for each reaction at each point in cycling (0 – blue, orange – 300, green – 600).

In Figures 3.15 and 3.16 , we show the results of the discharged curves from using the same methodology described in the main text for the charged curves. For Fig 3.15a and 3.15b, the original parameters from Verbrugge et al., were used and we found Q_{min}^{+} and Q_{min}^{-} to be 0.188 Ahr and 0.003 Ahr, respectively, that satisfied the constraints laid out in Eq (3.12) – (3.14). Since hysteresis can be seen the voltage curves, we modified the initial guess in the main text by shifting the standard potential parameters by a constant for all the positive electrode reactions ($U_j^{+,0} + c_1$) and a separate one for the negative electrode reactions initial guess ($U_j^{-,0} + c_2$), as shown in Fig S6c and S6d. The optimization results perform just as well as in the discharged steps as it does in the charged steps, as shown in both the plots shown against the experimental data (Fig 3.15e and Fig 3.15f) as well as the residual plots (Fig 3.15g and 3.15h). Figure 3.16 then shows all the fits of the MSMR model against experimental discharged data for the 0-, 300-, and 600-cycle cells. All the parameters and relevant information for these fits are given in Table S3.13-3.17.

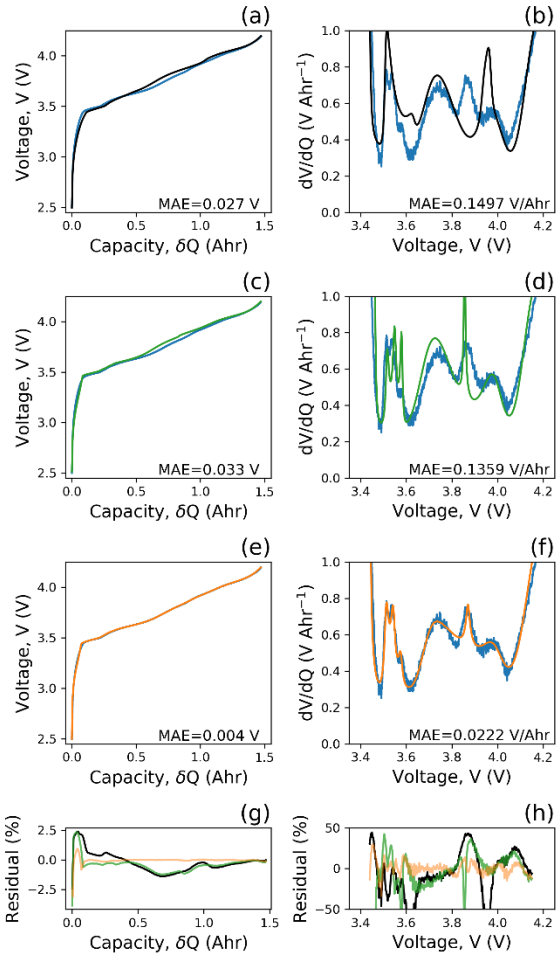

Figure 3.15 Open circuit potential and differential voltage curves of comparing computed to experimental (blue) data, using initial reaction parameters from literature (a, b) (black), manually modified reaction parameters (c, d) (green), and optimized reaction parameters (e, f) (orange), with their reported mean absolute values. The computed residuals (g, h) are being compared to the same experimental data collected from a fresh cell that was discharged at a C/20 rate.

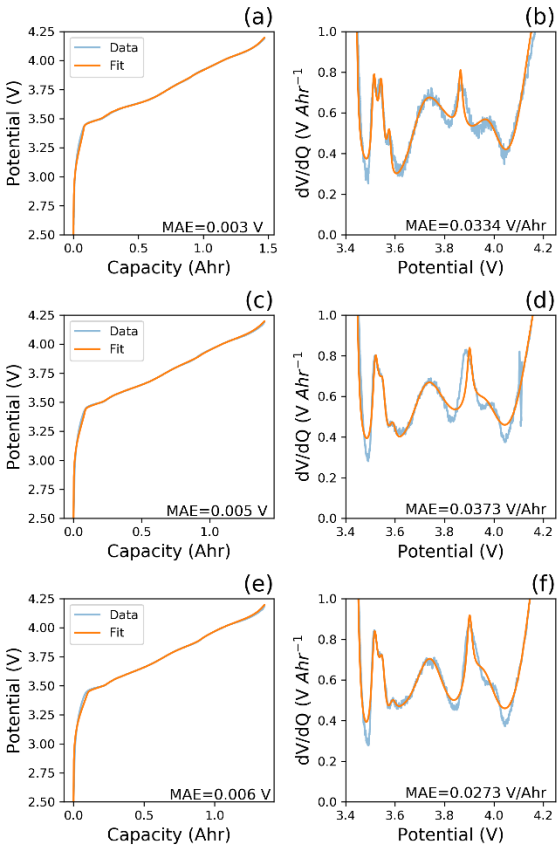

Figure 3.16 Open circuit potential and differential voltage curves of comparing optimized computed (orange) to experimental (blue) discharged data for fresh cells (a, b), cells that have been aged over 300 cycles (c, d), and cells that have been aged over 600 cycles (e, f), with their reported mean absolute values.

Table 3.13 Parameters from Manual Manipulation for fitting against fresh-cell discharge data

Reaction	U_j^0 (V vs Li/Li$^+$)	$Q_{tot,j}$ (Ahr)	ω_j
NMC1	3.668	0.185	0.967
NMC2	3.711	0.446	1.397
NMC3	3.891	0.290	3.505
NMC4	4.246	0.453	5.528
LMO1	3.997	0.234	1.520
LMO2	4.154	0.191	0.930
GRA1	0.100	1.131	0.086
GRA2	0.128	0.504	0.080
GRA3	0.149	0.049	0.150
GRA4	0.171	0.054	0.175
GRA5	0.193	0.134	0.122
GRA6	0.388	0.108	5.974

Table 3.14 Parameters from optimization for fresh cell discharge data

Reaction	U_j^0 (V vs Li/Li$^+$)	$Q_{tot,j}$ (Ahr)	ω_j
NMC1	3.677	0.148	1.169
NMC2	3.725	0.513	1.586
NMC3	3.905	0.229	2.629
NMC4	4.266	0.422	5.498
LMO1	4.011	0.222	1.900
LMO2	4.158	0.181	1.163
GRA1	0.105	0.849	0.108
GRA2	0.132	0.564	0.100
GRA3	0.152	0.061	0.152
GRA4	0.174	0.048	0.219
GRA5	0.199	0.142	0.152
GRA6	0.368	0.106	4.480

Table 3.15 Parameters from optimization for fitting 300 cycles aged cell discharge data

Reaction	U_j^0 (V vs Li/Li$^+$)	$Q_{tot,j}$ (Ahr)	ω_j
NMC1	3.685	0.186	0.877
NMC2	3.742	0.436	1.784
NMC3	3.925	0.171	2.641
NMC4	4.263	0.399	5.463
LMO1	3.991	0.225	1.961
LMO2	4.151	0.201	1.401
GRA1	0.100	0.858	0.134
GRA2	0.133	0.555	0.125
GRA3	0.152	0.076	0.150
GRA4	0.172	0.055	0.273
GRA5	0.201	0.139	0.188
GRA6	0.348	0.116	4.295

Table 3.16 Parameters from optimization for fitting 600 cycles aged cell discharge data

Reaction	U_j^0 (V vs Li/Li$^+$)	$Q_{tot,j}$ (Ahr)	ω_j
NMC1	3.700	0.232	0.658
NMC2	3.760	0.390	1.910
NMC3	3.945	0.129	2.675
NMC4	4.243	0.301	5.456
LMO1	3.974	0.205	1.470
LMO2	4.142	0.251	1.471
GRA1	0.092	0.845	0.168
GRA2	0.133	0.528	0.156
GRA3	0.155	0.079	0.188
GRA4	0.179	0.048	0.285
GRA5	0.213	0.122	0.234
GRA6	0.328	0.144	4.169

Table 3.17 Capacity of electrodes from discharge fits

Cycles	Q_{tot}^{+}	Q_{tot}^{-}
0	1.715	1.777
300	1.618	1.799
600	1.508	1.766

Fig 3.17 through 3.19 show the bootstrapped results of the charge data for the positive (a) and negative (b) electrodes for 0, 300, and 600 cycles whereas 3.20 through S3.22 show the results for the discharge data. These histograms have a solid, black line representing the median value, and then dashed, black lines that mark the 5th and 95th percentile values of the distributions. The bootstraps were initialized with the manually modified parameters for the 0-cycle, the results of cell 51's fits for the 300-cycle bootstrap, and the results of cell 1's fits for the 600-cycle bootstrap. We can observe a variety of different distributions in these histograms, where some parameters may exhibit a more normal distribution, skewed distributions, bimodal distributions, or even remain constant for every iteration.

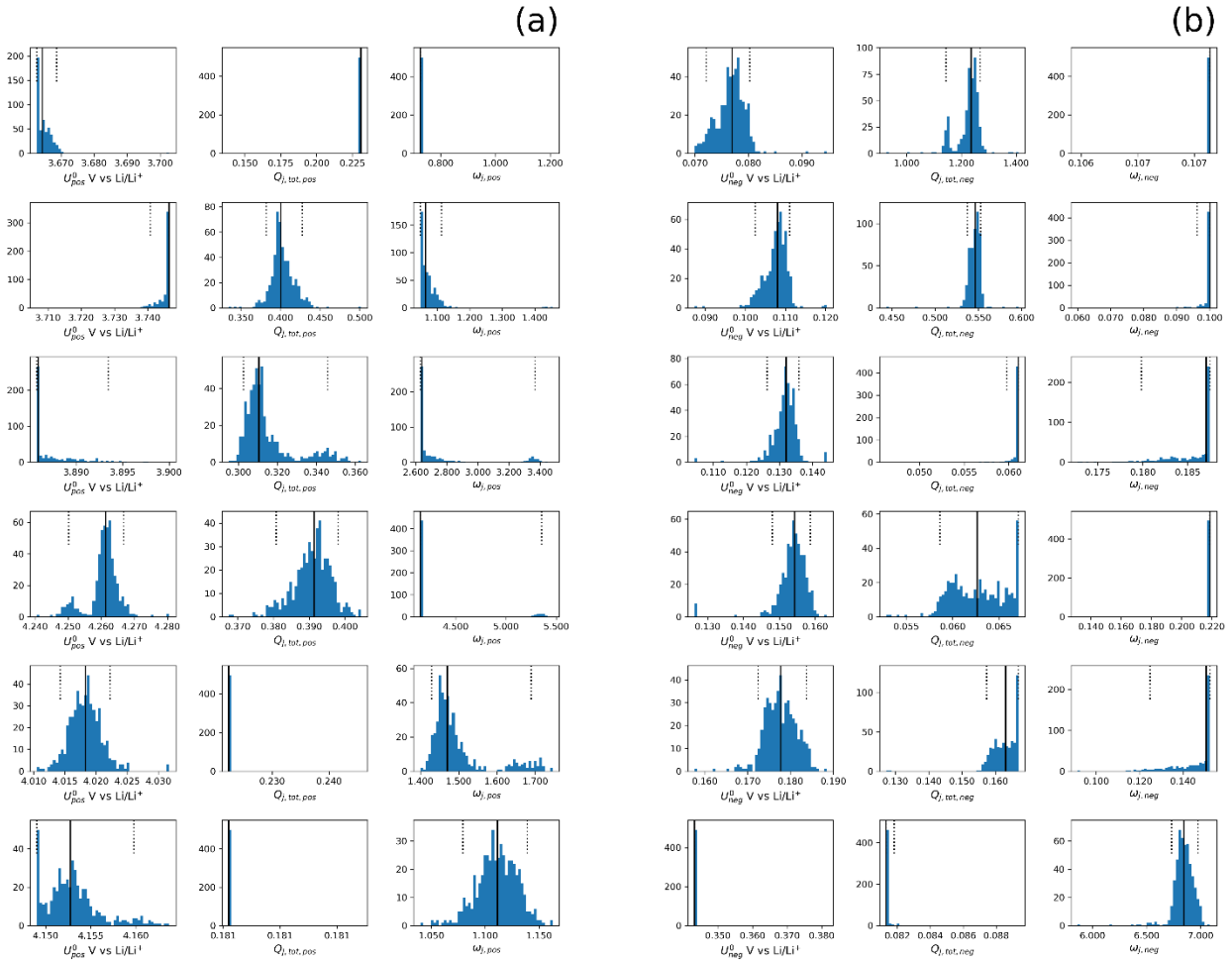

Figure 3.17 Bootstrapped data from fitting iterations using randomly sampled experimental data with replacement from the 0-cycle charge dataset. Each iteration fit was seeded with the same initial guess of the modified parameters found in Table 3 of the main manuscript. Each row represents a separate reaction j and the three columns show the distributions of the standard electrode potential (U_j^0) maximum capacity ($Q_{j,max}$), and the ω_j factor, respectively, for both the positive electrode (a) and negative electrode (b). A total of 500 iterations were done, but iterations where the fitting error was above 0.04 V/Ahr were removed.

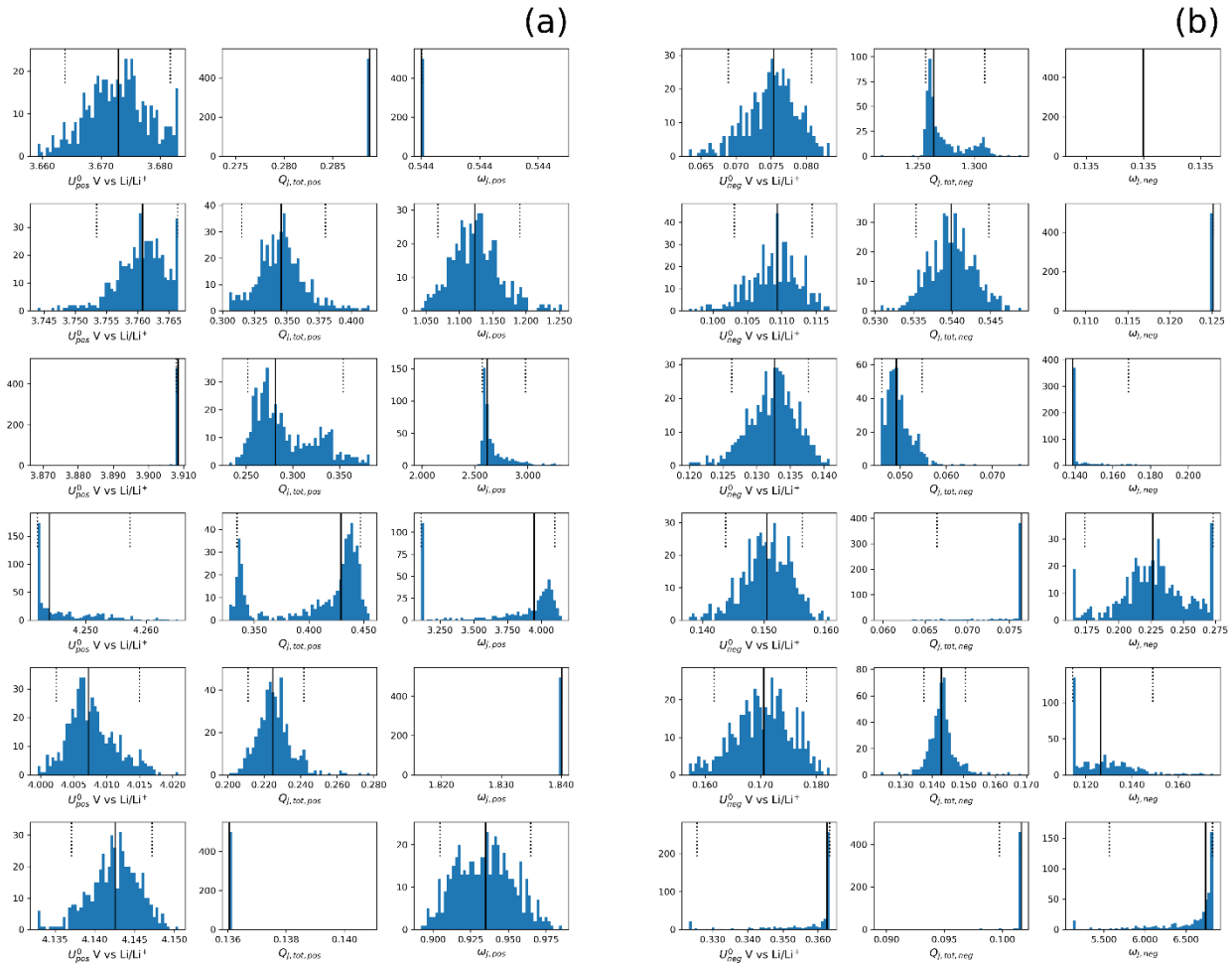

Figure 3.18 Bootstrapped data from fitting iterations using randomly sampled experimental data with replacement from the 300-cycle charge dataset. Each iteration fit was seeded with the same initial guess of the parameters found in Table 3. Each row represents a separate reaction j and the three columns show the distributions of the standard electrode potential (U_j^0) maximum capacity ($Q_{j,max}$), and the ω_j factor, respectively, for both the positive electrode (a) and negative electrode (b). A total of 500 iterations were done, but iterations where the fitting error was above 0.04 V/Ahr were removed.

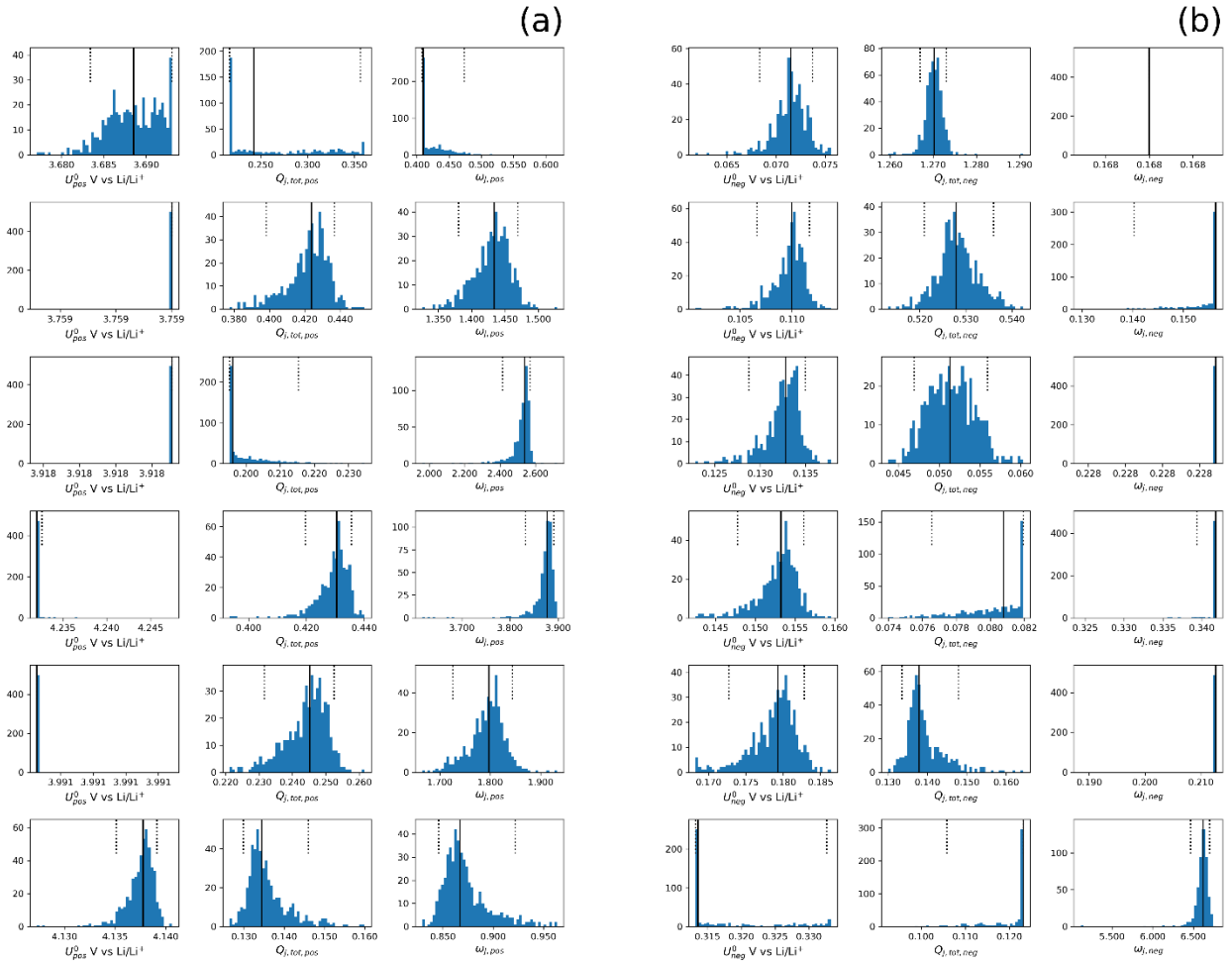

Figure 3.19 Bootstrapped data from fitting iterations using randomly sampled experimental data with replacement from the 600-cycle charge dataset. Each iteration fit was seeded with the same initial guess of the parameters found in Table 4. Each row represents a separate reaction j and the three columns show the distributions of the standard electrode potential (U_j^0) maximum capacity ($Q_{j,max}$), and the ω_j factor, respectively, for both the positive electrode (a) and negative electrode (b). A total of 500 iterations were done, but iterations where the fitting error was above 0.04 V/Ahr were removed

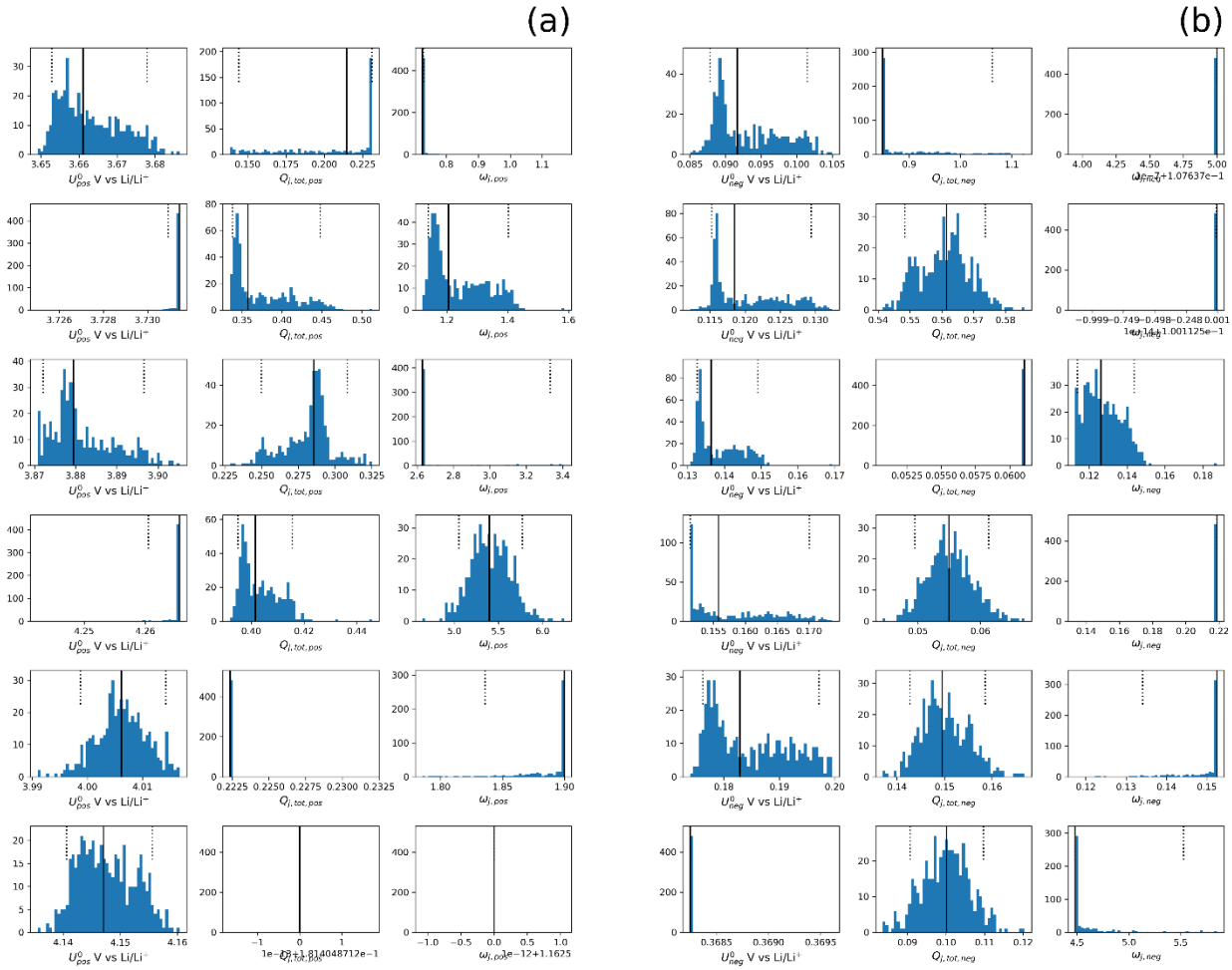

Figure 3.20 Bootstrapped data from fitting iterations using randomly sampled experimental data with replacement from the 0-cycle discharge dataset. Each iteration fit was seeded with the same initial guess of the modified parameters found in Table S4. Each row represents a separate reaction j and the three columns show the distributions of the standard electrode potential (U_j^0) maximum capacity ($Q_{j,max}$), and the ω_j factor, respectively, for both the positive electrode (a) and negative electrode (b). A total of 500 iterations were done, but iterations where the fitting error was above 0.04 V/Ahr were removed.

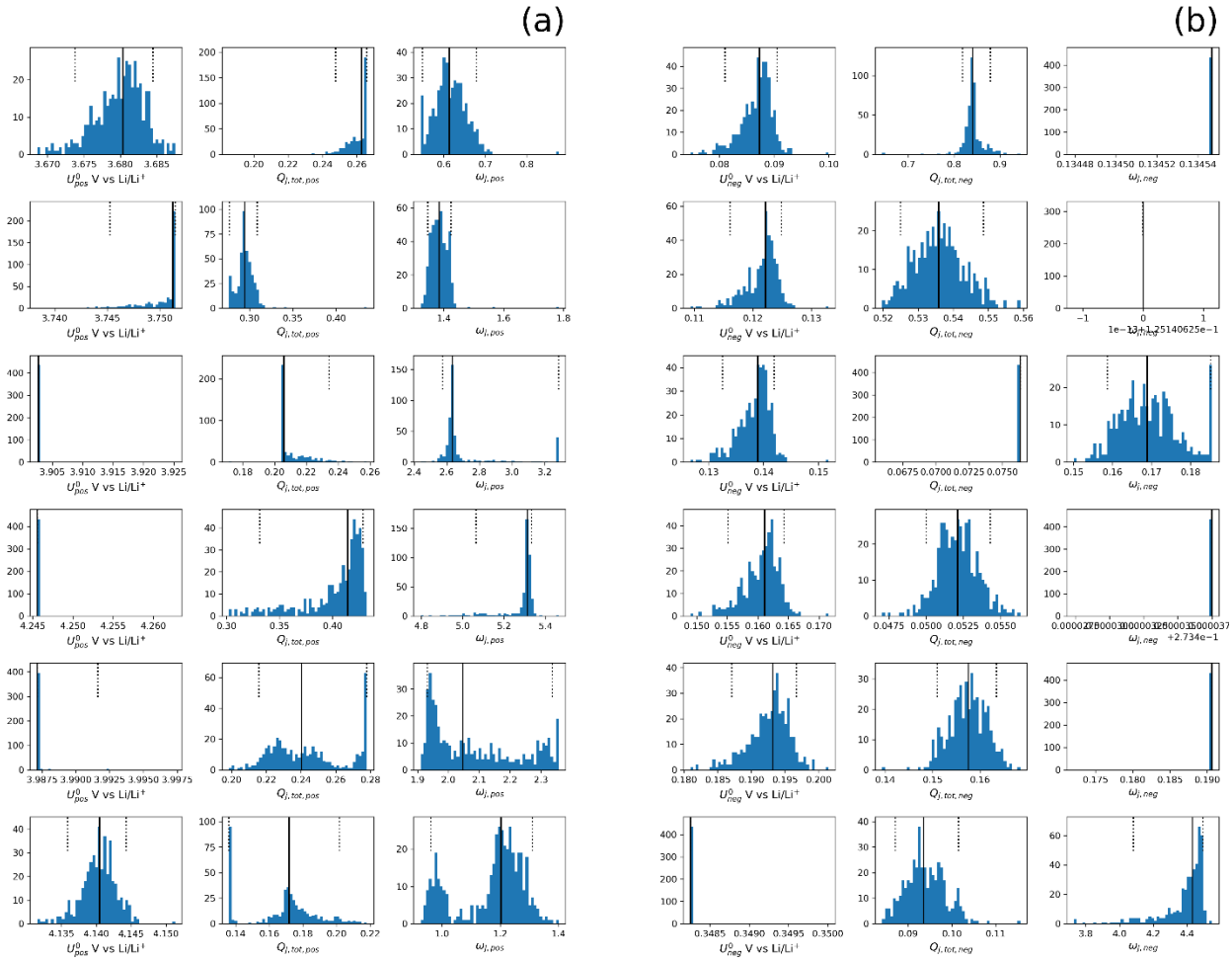

Figure 3.21 Bootstrapped data from fitting iterations using randomly sampled experimental data with replacement from the 300-cycle discharge dataset. Each iteration fit was seeded with the same initial guess of the parameters found in Table S5. Each row represents a separate reaction j and the three columns show the distributions of the standard electrode potential (U_j^0) maximum capacity ($Q_{j,max}$), and the ω_j factor, respectively, for both the positive electrode (a) and negative electrode (b). A total of 500 iterations were done, but iterations where the fitting error was above 0.04 V/Ahr were removed.

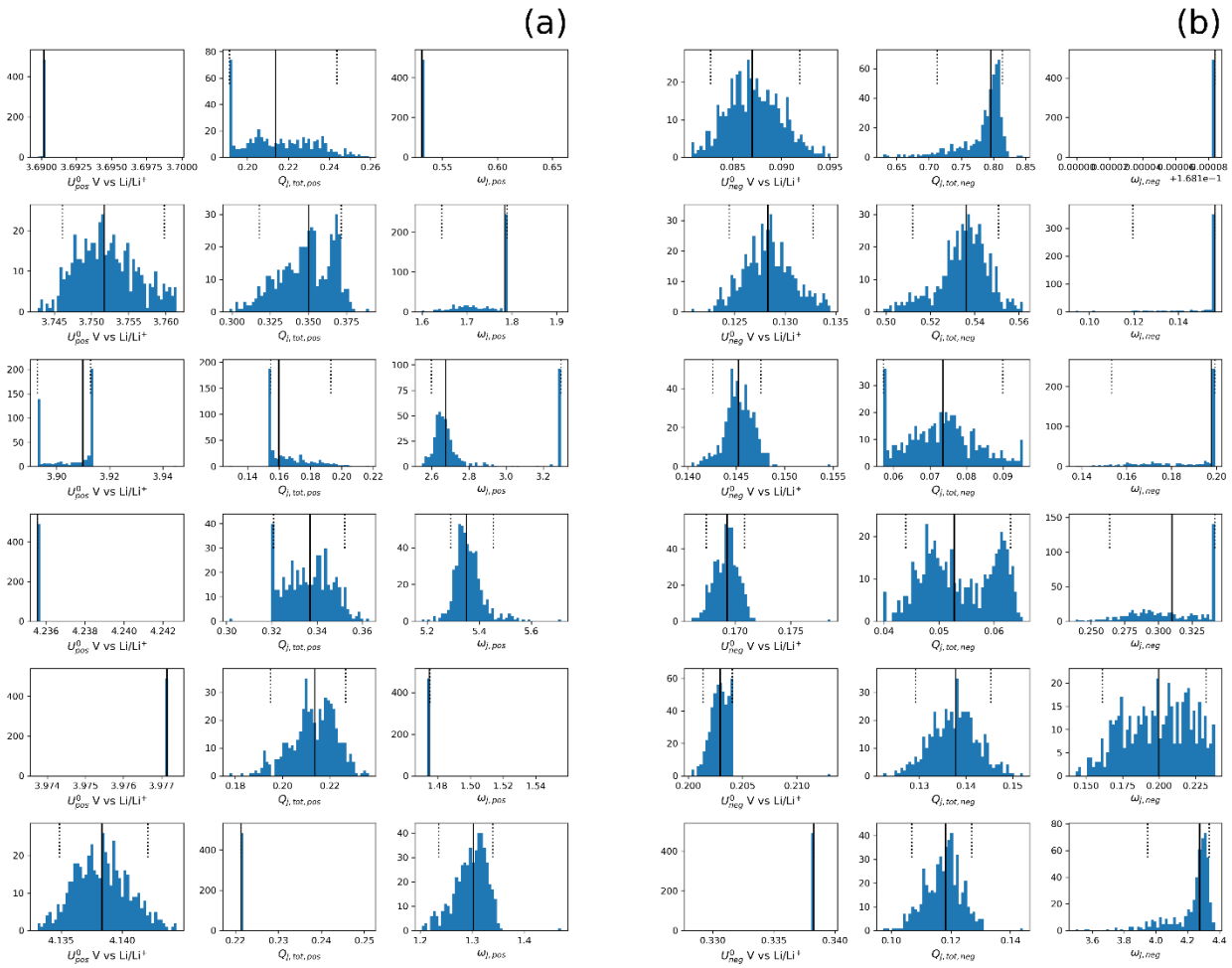

Figure 3.22 Bootstrapped data from fitting iterations using randomly sampled experimental data with replacement from the 600-cycle discharge dataset. Each iteration fit was seeded with the same initial guess of the parameters found in Table S6. Each row represents a separate reaction j and the three columns show the distributions of the standard electrode potential (U_j^0) maximum capacity ($Q_{j,max}$), and the ω_j factor, respectively, for both the positive electrode (a) and negative electrode (b). A total of 500 iterations were done, but iterations where the fitting error was above 0.04 V/Ahr were removed.

.

Chapter 4 - Reduced-order modeling of linear and nonlinear electrochemical impedance spectra using equivalent circuit methods

4.1 Introduction

Electrochemical impedance spectroscopy is an incredibly powerful tool that can be used to analyze a multitude of different physical and chemical behaviors in whole-cell lithium-ion batteries. By probing at different frequencies, EIS has the ability to parse out behaviors that are happening at different time scales, such as pure ohmic resistances at the limit of high frequencies, interfacial kinetics and charge-transfer at moderate frequencies, and then transport and thermodynamic properties at the limit of lower frequencies.[50] When used in a whole-cell, all these different physicochemical behaviors of the two electrodes can be convoluted in overlapping timescales and are in close proximity to chemically interact, leading to complex, nonlinear behavior that cannot always be captured by EIS alone. Thus, a natural extension is to increase the small-amplitude signals used in traditional EIS to a more-moderate value, where second harmonic signals in the output response can be seen out of the noise. In this method, nonlinear electrochemical impedance spectroscopy, NLEIS, information that was once inaccessible in the linearized method, EIS, can now be extracted.[24] However, few models and tools have been developed to analyze the nonlinear response, and those that are can be computationally rigorous and complicated. NLEIS and these methods are further explored in Chapter 5.

In most applications, equivalent circuit models have been the most widely adopted form of analysis for EIS spectra, as they are lower in mathematical complexity, efficient, and can easily capture degradation in lithium-ion batteries. Saha et al., used the interfacial charge-transfer kinetics extracted from equivalent circuit models to perform on Bayesian statistics to improve prognostics on the lifetime of lithium-ion batteries.[131] Zhang et al., constructed their own equivalent circuit to study the effects of the subjected voltage range on the formation of the solid-electrolyte interphase (SEI).[53] Levi and Aurbach were able to estimate transport properties, like diffusion coefficients, using equivalent circuit models from EIS spectra, and is shown that it is comparable to the results from other methods like galvanostatic intermittent titration technique.[29] While these methods have led to a variety of studies that have helped the community gain an understanding into the internal behaviors of electrochemical systems, it inherently lacks access to a trove of information because

traditional impedance is a linearized system.[24] In this work, we show that we are able to incorporate new, nonlinear circuit elements that aim to fit the second harmonic NLEIS spectra to extract relevant information with simpler, reduced-order methods.

4.2 Methodology

4.2.1 Cycling procedure and open-circuit voltage determination

All break-in cycling and degradative cycling measurements were made on commercially available Samsung 1.5 Ah LiNMC | C cells (INR 18650-15M) using a Maccor 4000M battery cycler with the temperature held constant at 25°C with a Maccor MTC-020 chamber. Break-in cycling for every cell was done with five C/2 cycles. The replicate cells used for open-circuit voltage determination and EIS/NLEIS experiments of fresh cells were removed, and the remaining replicate cells were subjected to 100 cycles of degradative aging using a 2C (3 A) constant-current within the manufacturer specified voltage limits from 2.5 V (0% SoC) to 4.2 V (100% SoC), a constant voltage at 4.2 V until a 100mA current cutoff was reached, and a constant current discharge at 2C back down to 2.5 V.

Low current scans are a common, accessible way of estimating the open-circuit potential curves of electrochemical systems because it minimizes the overpotential associated with polarization. Here, open-circuit voltage measurements were performed using an extremely low-rate constant current scan of 30 mA (C/50) on both fresh and aged cells on an Arbin High Precision Coulometer. Voltage, current, and capacity measurements were tracked on a per second basis. A Savitzy-Golay smoothing filter with a third-order polynomial was used to smooth the open-circuit potential plot. For this study, we selected a window length of n = 99 points, resulting in a window with 49 points before and 49 points after the central voltage. Each slow-scan contained roughly 17,000 points, with each point collected ten seconds apart, so this window-length covers a small expanse of the total curve. From these plots, the first and second order of the continuous open-circuit potential curve could be computed by taking the first and second derivative of the higher-order polynomial filter. As compared to the work in Chapter 3, the second derivative was given priority, so this window-length was chosen so that the second derivatives were distinguishable, but not overly smoothed.

4.2.2 Thermodynamic modeling using the MSMR model

Thermodynamic properties, such as the differential voltage and its subsequent derivative have been shown to be important parameters that determine the behavior of the low-frequency response in impedance measurements.[77,132] These impedance models require these thermodynamic data for each of the two electrodes, which may be readily accessible in a whole-cell without performing destructive or postmortem analysis. Thus, we apply the methodology of the Multi-Species, Multi-Reaction model explained in Chapter 3 to help us access this information. Since these are the same types of cells used in prior studies, we estimated that the full cell has a positive electrode capacity, Q_{tot}^{+} = 1.8 Ah, and a n/p ratio of 1.1, leading to a Q_{tot}^{+} = 1.96 Ah. For the model, we optimize the capacity and differential voltage points between a voltage range of 3.49 V and 4.15 V to minimize the contributions of the bounds. However, we follow the same procedure, where we set voltage constraints at the lower and upper cell voltage cycling limits (V_{lower} = 3.10 V and V_{upper} = 4.2 V) from the slow-scan experiment, and bounds for each parameter, where U_j^0 was allowed to vary by 20 mV; $Q_{j,tot}$ could vary up to 25% from the initial value, and ω_j was allowed to vary by 25% of the initial value. It is important to reiterate that the ω used in the MSMR model is a simplified thermodynamic factor of the activity coefficients, and not frequency as it represents in impedance notation. Once the fresh cell was fit, the parameters were then seeded into the fitting of the 100-cycle aged cells as initial guesses and the same procedure was used. Once these fits were complete, we could then extract out the related differentials, dU/dQ and d^2U/dQ^2, for each electrode.

4.2.3 EIS and NLEIS measurements of thermodynamic interest

Impedance measurements were completed at points of thermodynamic interest, meaning where local maxima and minima of the first and second derivatives exist. The full experimental data acquisition technique can be found in Chapter 5, where we perform a frequency sweep from 10 kHz to 3.16 mHz at three different amplitudes (ΔI = 300, 400 and 500 mA). In this case, fresh cells and aged cells were used to study two different voltage ranges. The fresh cells were used at the voltage window between 3.8 V and 3.92 V while the aged cells were used for all voltages below 3.65 V, as shown in Tables 4.1 and 4.2. From prior work, it is shown that the strength of the second harmonic response is very low in these cells, which is to be expected. However, even with

very mild capacity fade (< 1.0%), it has been shown that the strength of the nonlinear signal grows quite substantially. This was done because the second harmonic signals at the lower voltage window for the fresh cells had a very low signal-to-noise ratio, leading to very a noisy $Z_{2,2}$ spectra. Once the cells were aged, degradation mechanisms in the lower voltage region increased the nonlinear impedance, allowing for cleaner signals with the improved signal-to-noise ratio. From the same set of data, both the linear and nonlinear impedance are measured.

Table 4.1 Voltages for different SoCs in fresh-cell studies

State-of-Charge (%)	Voltage (V)
50	3.820
51	3.826
53	3.850
55	3.875
58	3.900
60	3.920

Table 4.2 Voltages for different SoCs in aged-cell studies

State-of-Charge (%)	Voltage (V)
10	3.500
16	3.561
17	3.575
19	3.590
21	3.605
23	3.620

4.2.4 Equivalent circuit models of impedance measurements

One of the most common tools used to analyze and understand impedance data are equivalent circuit models, where each electrode in the whole cell is analogous to an RC circuit. However, to capture transport and thermodynamic properties, an extension of the RC circuit is the Randle's circuit, which has a capacitor in parallel with the charge-transfer resistance and a

Warburg element in series. While these equivalent circuit models have been widely adopted for extracting information from EIS measurements, an analog has not yet been fully developed for the nonlinear response to enable a more straightforward, less-complicated analysis.

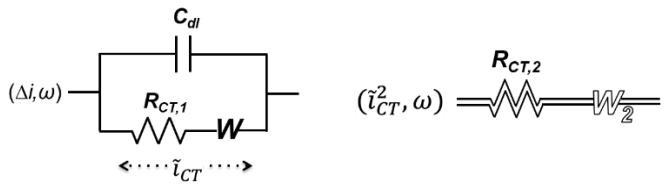

Figure 4.1 Common Randle's circuit (left) with a double-layer capacitance (C_{dl}) in parallel with two elements, a charge-transfer resistor (R_{CT}) and Warburg (W) element, in series. The additional branch (right) is related to the i_{ct} branch in the Randle's circuit nonlinear equivalent circuit elements, where a second-harmonic charge-transfer resistor ($R_{CT,2}$) and a second-harmonic Warburg (W_2) element are connected in series.

In this work, we first take our linear impedance measurement and using an open-source package on Python, impedance.py, we fit our data to a whole circuit that consists of three elements.[97] These three components, all connected in series, are a pure ohmic resistor, one Randle's circuit element to represent the negative electrode, and then another circuit element to represent the positive electrode that is another Randle's circuit. Within each Randle's circuit, the charge-transfer resistance is estimated by the width of each electrode's arc, whereas the Warburg element has a much more complicated impedance, modelled by

$$W = \frac{Y_0}{\sqrt{\omega}}\left[1 - j\left(1 + \frac{Y_1}{\sqrt{\omega}}\right)\right] \quad [4.1]$$

Once the linear impedance has been fit and the parameters for each of the elements within the whole circuit are determined, the next step is to build the nonlinear equivalent circuit analogs to try and fit the nonlinear impedance. One way to do this is to employ the formalism developed by Schwartz, where we take the same equivalent circuits, as shown above, and calculate the complex quantity, $\tilde{\theta}$, which splits the proportion of the current that flows through the charge-transfer branch (R_{CT} and W) into its real component, θ', and the proportion that the flows through the capacitive branch into the imaginary component, θ", for either electrode, j. In these Randle's circuits, we can find these quantities through Eq 4.2:

$$\theta'(\omega) - j\theta(\omega) = \frac{\tilde{Z}}{R_{CT,j} + W} \quad [4.2]$$

If we then assume that there the nonlinear analog of the circuits is as shown in Fig 4.1, then we can derive the following equation for the second harmonic impedance

$$\tilde{Z}_{2,2} = [R_{CT,2} + W_2][(\theta'^2 - \theta"^2) - j(2\theta'\theta")] \quad [4.3]$$

To determine the second-harmonic Warburg, Schwartz expands the linear Warburg impedance W_1 by examining how deviations in intercalated Li^+ affect the voltage fluctuations. Through this analysis, it's determined that the nonlinear Warburg element contains no new time constants from the linear component and is dependent on additional thermodynamic property (the second derivative of open-circuit potential), and the linear Warburg. The equation can be written as:

$$W_2 = \frac{1}{2}\frac{d^2U}{dq^2}\left(W/\frac{dU}{dq}\right)^2 \quad [4.4]$$

Thus, we can rewrite the second harmonic impedance to reflect the contribution of the linear Warburg component.

$$\tilde{Z}_{2,2} = \left[R_{CT,2} + \frac{1}{2}\frac{d^2U}{dq^2}\left(W/\frac{dU}{dq}\right)^2\right][(\theta'^2 - \theta"^2) - j(2\theta'\theta")] \quad [4.5]$$

Where the parameters that are allowed to vary for the fitting process are the nonlinear charge-transfer resistances, $R_{CT,2}$, and a lumped thermodynamic factor parameter, $B_{n,j}$ for an electrode, j, as defined as:

$$B_{n,j} = \frac{1}{2}\frac{d^2U}{dq^2}_j \Big/ \left(\frac{dU}{dq}_j\right)^2 \quad [4.6]$$

4.3 Results and Discussion

4.3.1 Understanding the thermodynamics of the Li|NMC cells

The open-circuit potential curve, first derivative, and second derivative of the open-circuit potential with respect to capacity of a fresh Li|NMC battery were determined with a C/50 constant current scan, as shown in Fig 4.2a, 4.2b, and 4.2c, respectively. These experiments were done in a controlled temperature of 25°C. The open-circuit potential is not completely linear, as evident by the subsequent differential capacity plots, where there are at least six prominent peaks in the dV/dQ plot, each representing different reactions, phase transitions, or staging phenomena in the two

electrodes. The derivatives were calculated using a Savitzy-Golay filter third-order polynomial with a moving window. For this work, high-precision coulometry equipment was used to collect the C/50 scan, but even with increased precision, errors and noise are undoubtedly propagated with further differentiation. Thus, despite the accuracy of this work, we needed to select a window size of 129 points to attain a second-derivative curve where features can be distinguished but not overly smoothed.

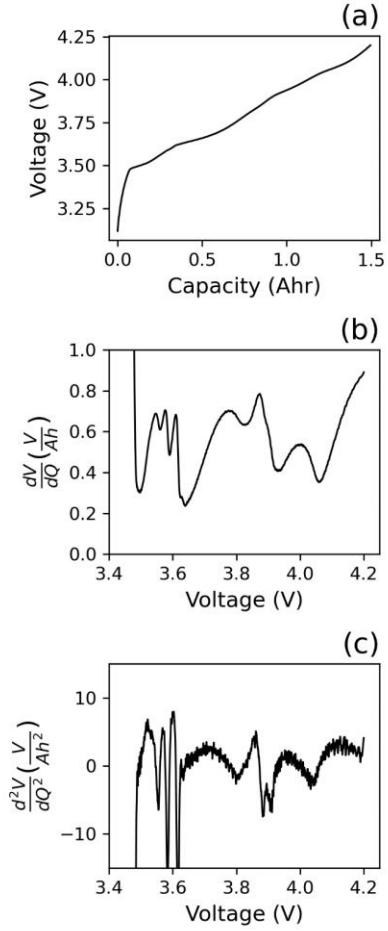

Figure 4.2: Open-circuit voltage curve (a), its first derivative with respect to capacity (b) and its second derivative with respect to capacity (c), for a fresh Samsung cell taken at 25°C with a C/50 scan rate. The derivative results here are calculated using a moving, smoothing Savitzy-Golay filter that calculates the derivatives of the open-circuit potential over 129 individual points. Each curve is made up of roughly 17,000 points.

At first glances of the open-circuit voltages for the fresh and aged cell, Fig 4.2a and 4.3a, there are no discernible differences, especially since there has been an extremely small amount of

capacity fade in these cells (<1 %). Upon looking at the differential voltage, we can start to see pick up details about the solid-states behaviors, where we see the sharper peak centered around 3.87 V begin to shift towards higher voltages. Just like the open-circuit voltage though, the differential voltage is only capable of either monotonically increasing or decreasing, meaning that the sign of the value will always be the same. Upon further differentiation, we begin to see this monotonicity break, where the second derivative has multiple regions where the signal can be of either positive, negative, or zero, giving us more levers to control and examine when we begin to include other electrochemical techniques and analyses.

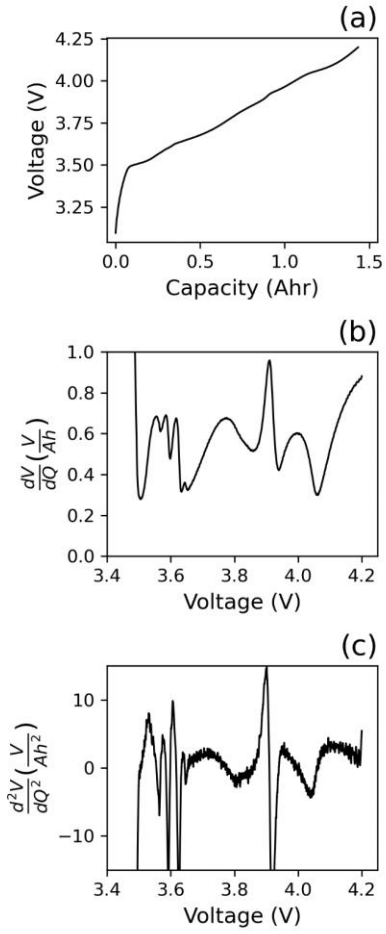

Figure 4.3: Open-circuit voltage curve (a), its first derivative with respect to capacity (b) and its second derivative with respect to capacity (c), for an aged Samsung cell (100 cycles) taken at 25°C with a C/50 scan rate. The derivative results here are calculated using a moving, smoothing Savitzy-Golay filter that calculates the derivatives of the open-circuit potential over 129 individual points. Each curve is made up of roughly 17,000 points.

Furthermore, we can also perform electrochemical impedance spectroscopy and nonlinear electrochemical impedance spectroscopy (EIS and NLEIS) to further probe not just the thermodynamic and transport properties of these cells, but also charge-transfer kinetics at a variety of different states-of-charge. In Figure 4.4, we show the Nyquist plots for the linear impedance and nonlinear impedance for fresh cells and aged cells at 10, 30, 50, and 60% SoC.

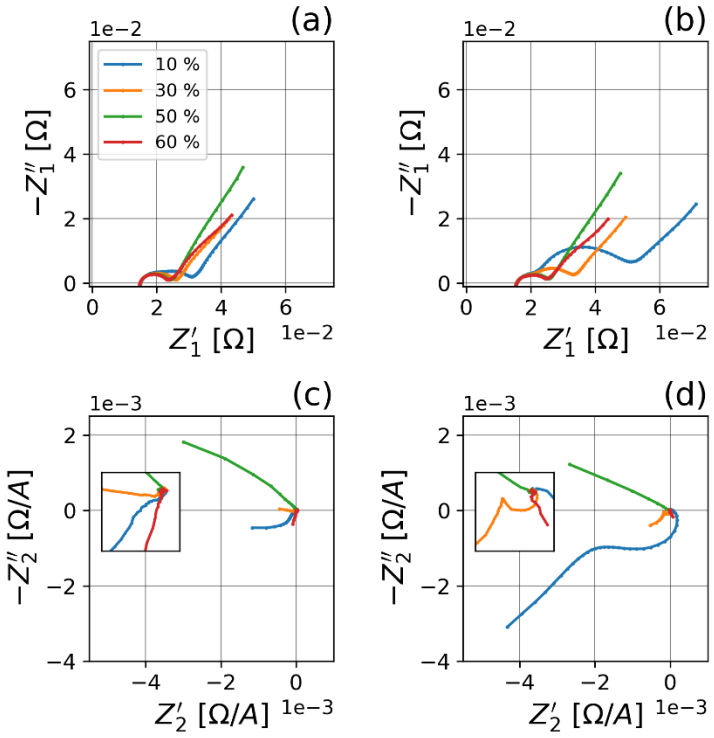

Figure 4.4 Linear and nonlinear impedance spectra for fresh (a, c) and 100-cycled aged (b, d) cells at multiple states-of-charge. Inset plots in the nonlinear spectra are zoomed in near the origin, where the magnitude of the 30% and 60% SoC spectra can be better observed. All impedance measurements were collected over a frequency range from 10,000 Hz to 3.16 mHz. All second-harmonic spectra are truncated at 10 Hz to remove signals generated from experimental noise.

Here, we can see that despite the minute capacity fade, there can be significant deviations in the behavior of the AC responses. For example, at 10% SoC, the battery shows the most prominent signs of aging, where we see a more sluggish electrode, given by the emergence of a secondary, larger arc in the linear impedance. Similarly, at 30% SoC, we still see the signs of a slower electrode, albeit not nearly as pronounced as the 10% spectra. When we move into higher SoCs, we begin to see that the response remains relatively constant and that both electrodes have similar kinetics, as there are no two distinct arcs, and the magnitudes of the impedance values are similar.

More interestingly, some of the NLEIS signals have evolved in ways that are much more dramatic than the linear impedance. The NLEIS signals are truncated at 10 Hz because of inherent instrumentation noise. For the 10% SoC, we see that the magnitude of the nonlinear response has increased with the small amount of aging, as well as what may be an overlap in the timescales of contributions from charge-transfer effects and transport effects, much like the response in the linear impedance. The 30% SoC is equally interesting, and is further explored in Chapter 5, but here, we begin to see a prominent charge-transfer arc in the nonlinear response, as shown in the inset, and a low-frequency second-harmonic tail. Finally, the NLEIS signals at 50% remains unchanged and the direction of the low-frequency tail in the 60% changes direction slightly.

Using these data, we were able to develop a more careful study, where we can measure the linear and nonlinear impedances in between some of these SoCs of interest. For example, we see that in between 50% and 60% SoC, aging the battery did not change the linear nor nonlinear impedance in a significant way. However, interestingly enough, we do see that in this region (between 3.820 and 3.920 V), that the NLEIS spectra shifts from the second quadrant into the fourth. In the slow-scan thermodynamic data, we also see that the first derivative traverses through the sharp peak at 3.90 V, and that the second derivative is oscillating in signs. Since we did not see any appreciable increase in the magnitude of the nonlinear impedance or directional shift from aging, we thus used fresh cells to study this voltage range to reduce experiment time and cost. However, the lower SoC regions (3.500 V to 3.643 V) exhibited aging effects, with the emergence of a mid-frequency response indicative of charge-transfer behavior. In addition, this region also has a number of peaks in the first derivative and oscillations in signs as well in the second derivative, making these spectra potentially information-rich in both the charge-transfer and transport/thermodynamic regions.

4.3.2 Thermodynamic information using the MSMR model

The theory behind the physics of EIS and NLEIS states that differences in SoC are demonstrated through differences in derivatives of each electrodes' open-circuit potentials with respect to the solid-state concentration, diffusivities, interfacial capacitances, and charge-transfer characteristics.[58] The first-order derivative can vary widely in magnitude, but will always be monotonic or zero, while the second order can vary in both sign and widely in magnitude. The physics show that thermodynamic contributions to the linear impedance are only affected by the

first-order derivative of the two electrodes,[58,132] while the nonlinear, second harmonic impedance is affected by both the first- and second-order derivatives.[77] Thus, it is critical to understand how the whole-cell response of the open-circuit voltage and its subsequent derivatives are achieved by the two electrodes.

From prior studies of differential capacity on similar batteries, confirmed by our own postmortem characterization of our cells, show that the positive electrode material of our batteries is a blended cathode, comprised of LiNMC and spinel-LiMnO2.[120] When the whole-cell response is disaggregated, it is reported that the dV/dQ contribution of the positive electrode is mostly constant during the first two peaks and slightly decreasing during the third peak of the graphite staging process (3.45 V to 3.65 V). The negative electrode is reported to have no contributions to the dV/dQ except for the distinct, sharp peaks that are exhibited. Theoretically, this gives us the ability to measure the thermodynamic effects of each individual electrode within a fully assembled cell, as the reaction peaks are potentially separated along the open-circuit potential curve. To do so, we employ the MSMR model from Chapter 3.

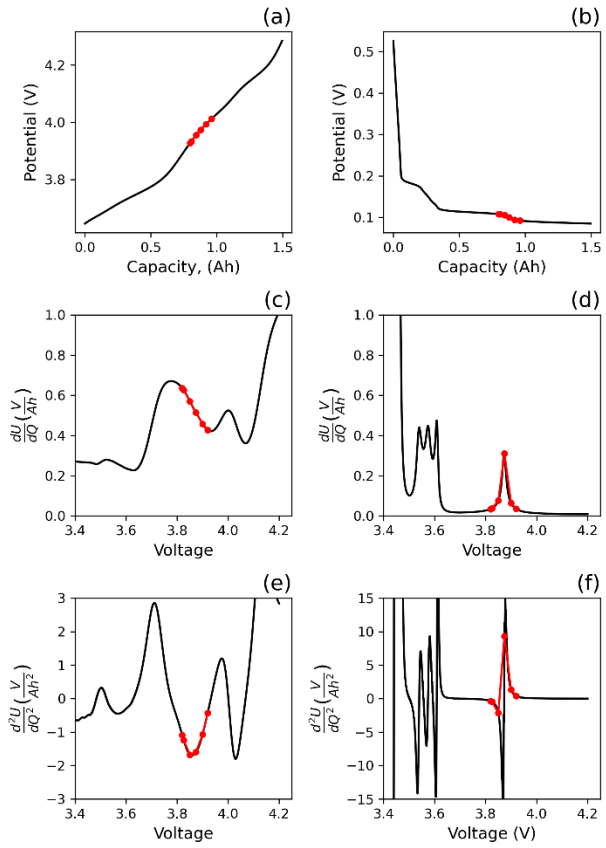

Figure 4.5 Thermodynamic data on the positive electrode (a, c, e) and negative electrode (b, d, e) for the fresh cells that are extracted and derived from the MSMR model fits. The open-circuit potential (a, b), and differential voltage (c, d) for the two electrodes are solved analytically using the model equations. The second-order derivative (e, f) are derived empirically using a higher-order Savitzy-Golay filter. Red markers are used to indicate approximately the voltages where EIS/NLEIS measurements were taken in the fresh-cell study.

Here we show results of fitting the above C/50 slow scans to the MSMR model. We disaggregate the whole-cell response of the fresh and aged cell into their half-cell responses in Figures 4.5 and 4.6, respectively. For each figure, the left-hand plots depict the positive electrode (a, c, e) response and the right-hand side shows the negative electrode (b, d, f) response. In Figure 4.5, voltages at which impedance measurements were measured are highlighted in red. Here, the MSMR model follows the trends found in literature, where the differential voltage of the positive electrode is consistently decreasing and changes concavity (4.5c), which leads to a local minima and further fluctuations in the second derivative (4.5e). In the negative electrode, the response in this voltage range traverses through the peak (4.5d), leading to second derivative values that are near zero, highly negative, and highly positive (4.5f).

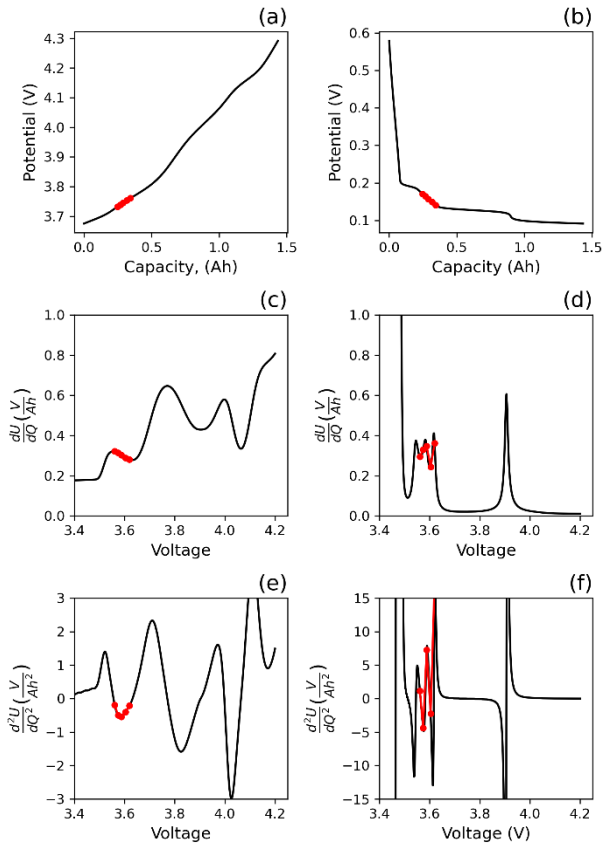

Figure 4.6 Thermodynamic data on the positive electrode (a, c, e) and negative electrode (b, d, e) for the 100-cycle aged cells that are extracted and derived from the MSMR model fits. The open-circuit potential (a, b), and differential voltage (c, d) for the two electrodes are solved analytically using the model equations. The second-order derivative (e, f) are derived empirically using a higher-order Savitzy-Golay filter. Red markers are used to indicate approximately the voltages where EIS/NLEIS measurements were taken in the aged-cell study.

The MSMR results for the aged cells further support the claims found in literature, where in this lower SoC range, 10 – 23% (3.500 V to 3.620 V), the magnitude of the positive electrode response derivative responses (dU/dQ and d^2U/dQ^2) remain fairly constant, whereas the negative electrode has a much different response. The negative electrode is undergoing multiple different staging processes as evident in the differential voltage, leading to constant shifting in signs in the second derivative. Because of the MSMR model, we are able to calculate these thermodynamic parameters, dU/dQ and d^2U/dQ^2 and apply them in trying to understand some of the phenomena that the linear and nonlinear impedances exhibit.

4.3.3 Impedance measurements and fitting for fresh cells

Figure 4.7 shows the linear and nonlinear NLEIS spectra for a fresh cell as it is charged from 50% to 60% SoC. In the linear impedance, all spectra have indistinguishable high-frequency ($\omega > 1000$ Hz) and small differences in the mid-frequency ($\omega > 1$ Hz) responses. The largest differences can be seen in angles and magnitudes of the low-frequency thermodynamic and diffusive tails ($\omega < 1$ Hz). In contrast, the second harmonic distinctly lack any mid-frequency feature, indicative of charge-transfer symmetry, so the only responses that are being measured are those related to the thermodynamics and transport of the cell. Nevertheless, the NLEIS response shows much more drastic changes in this regime. However, in the NLEIS response, we see that the low-frequency tail has a drastically different phase angle, with a complete switch in quadrant by the time the cell reaches 58% SoC.

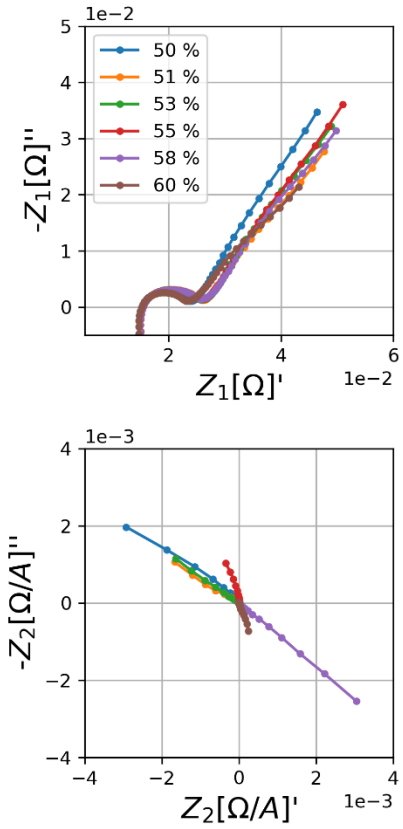

Figure 4.7 Nyquist plots of measured first (a) and second (b) harmonic coefficients, $\tilde{Z}_{1,1}(\omega 1)$ and $\tilde{Z}_{2,2}(\omega 1)$ for a fresh cell between the SoC range from 50% to 60%. The second harmonic data is truncated at 10 Hz.

To try and elucidate what may be causing these dramatic shifts in quadrants, we used the Randle's circuits and the nonlinear circuit elements to fit the data. Here, we first fit the linear impedance of the 50% SoC using the initial guesses outlined in Table 4.3, where we assume that the electrodes are similar in charge-transfer, where there is some difference in the characteristic frequency, but not enough to lead to two distinct arcs. We also assume that the two Warburg elements have very different characteristics, where one has significantly faster transport properties and shorter diffusion lengths leading to a vertical asymptote with decreasing frequency, and the other with a longer diffusion length, leading to a more traditional 45° angle line with decreasing frequency. Once the linear impedance was fit, these parameters were held constant, and used to calculate the nonlinear impedance, where four additional parameters, the second harmonic charge-transfer, $R_{CT,2}$, and the lumped thermodynamic parameters, B, are fit. The initial guesses for these parameters are found in Table 4.4. The fit parameters were then seeded into the next SoC, and the process continued until the last SoC was solved. In Fig 4.8, we show the results of all the fit parameters as a function of SoC.

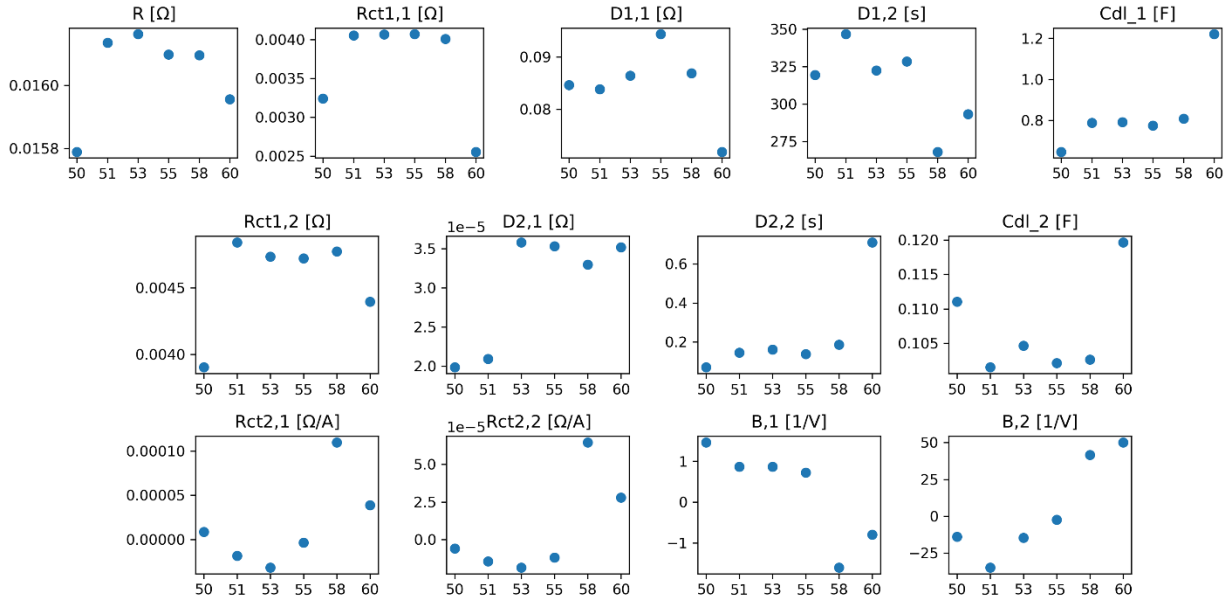

Figure 4.8 Plots of model parameter fits for the linear impedance (first row and second row) and the nonlinear impedance as a function of state-of-charge for the fresh-cell study. The top row includes parameters for the pure ohmic resistance and the Randle's circuit parameters for electrode 1. The middle row contains the Randle's circuit parameters for electrode 2. The bottom row shows parameters for the nonlinear circuit elements.

From these fitting results, we can see that the linear parameters have small variations throughout all the fits to capture the small differences seen in the linear Nyquist plots over this SoC range. The fits mirrored the initial guess, with no large discrepancy in the kinetic timescales, and the two electrodes keeping their vastly differing Warburg elements. For all fits shown using this work, we make the assumption that electrode one is the positive electrode and electrode two is the negative electrode. When we examine the parameters from fitting the nonlinear parameters, we start to see interesting trends emerge. First, in this voltage region, the frequencies related to the electrode charge-transfer properties do not generate an appreciable second harmonic signal meaning that all the response is purely due to thermodynamic and transport behavior. We can see this from our fits, where all the fit values for the nonlinear charge-transfer resistance (R_{CT2}) for both the positive and negative electrode are all nominally close to 0 for most SoCs. Additionally, the magnitudes of the two nonlinear charge-transfer resistances are roughly equal, meaning that the nature of the negative parity signal will result in the whole-cell Z_2 response to equate close to zero, such as in the cases for the 58% and 60% results.

In between 55% and 58% SoC, we see a major shift in the lumped thermodynamic parameters, as B_1 (positive electrode) becomes negative whereas B_2 (positive electrode) shifts into positive values. These trends that are observed in the lumped parameter fits follow the trends that we see in the derivatives that we calculated with the MSMR model in Figure 4.5, where we see both the positive and negative electrodes' second derivative values change signs. While it does not line up perfectly, it is important to reiterate that the results of the MSMR models are still based off a C/50 scan, where the dynamic operation, albeit very slow, still generates an inherent offset from the true OCV, which may shift the locations of these peaks. However, these offsets are very small, so generally, we know that we are probing within the local vicinity of the MSMR results.

This sudden quadrant shift in the second harmonic could be attributed to phase change of the dominating reaction. The dV/dQ plot shows that at these SoCs, the dominating reaction in the positive electrode shifts from intercalation/deintercalation of the NMC phase and into the MnO2 phase. From literature, it is known that spinel MnO2 is blended into electrodes to serve as a high-rate component, inherently leading to much faster diffusivities and different transport rates.[133] Given that, it is not surprising that this shift is an abrupt transition, as the material that is now being

electrochemically investigated is potentially different. This further shows that NLEIS can serve as a much stronger diagnostic signal than its traditional EIS counterpart.

4.3.4 Impedance measurements and fitting for aged cells

The next SoC region that we wanted to explore was the three graphite peaks that are present in the dV/dQ plot below 30% SoC (3.643 V). These three peaks include several different local maxima and minima in the first derivative and varying sign changes in the second. Furthermore, when the two different electrode contributions are separated, the derivative of the positive electrode remains fairly constant, so any changes to the thermodynamics response of the EIS should be related to the changes exhibited by the negative electrode, as shown in Figure 4.6.

In the linear spectra, as shown in Figure 4.9, there is a separation of two different electrodes, made evident by the second mid-frequency arc (10 Hz > ω > 0.10 Hz), as we have seen in these aged cells. However, in this voltage range, the changes in the spectra are small, with a monotonically shrinking mid-frequency arc with increasing SoC, and indiscernible differences in neither the high-frequency region or the low-frequency tails. However, when we look at the NLEIS response of these signals, we see a distinguishable difference between these small increments of SoCs. Similar to the linear response, we see that the mid-frequency kinetic arc associated with the positive electrode shrinks in magnitude as the SoC is increased. The low-frequency tails observed though have subtle differences in their angle and directionality as they approach lower frequencies. These signals do not appear to be artifacts of just instrument noise either, as each of these experiments were done in triplicate to ensure reproducibility. Understanding these subtle differences though is much less intuitive, as the thermodynamics of the second harmonic-response is sensitive to changes in both first and second-order derivative of the open-circuit potential.

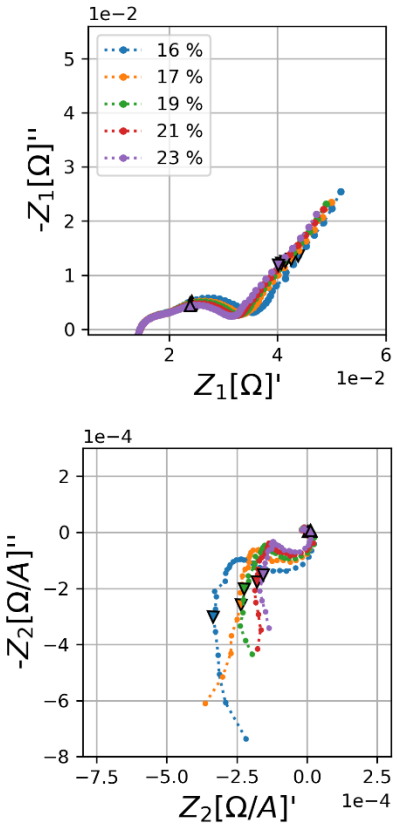

Figure 4.9 Nyquist plots of measured first (a) and second (b) harmonic coefficients, $\tilde{Z}_{1,1}(\omega 1)$ and $\tilde{Z}_{2,2}$ (ω1) of an aged battery (100 cycles) at SoCs between 16% and 23% The second harmonic data is truncated at 10 Hz.

As compared to the 10% SoC, the nonlinear impedances in the 16 – 23 % (3.561 to 3.620 V) range have two distinct regions that are separately dominated by charge-transfer behavior and transport/thermodynamic properties, without one major overlapping set of frequencies where there the two processes occur at similar timescales. As with the fresh-aged cells fits, we first start with fitting the linear impedance of the 16% SoC, and then use those parameters to fit the nonlinear impedance of the same state. Here, the fitting scheme again uses two Randle's circuits to model the two separate electrodes, with one set of Randle's circuit parameters having faster kinetics and faster transport properties (negative electrode), and then a second electrode with sluggish kinetics and slower transport (positive electrode). For the nonlinear parameters, we assume an appreciable second-harmonic charge-transfer resistance in the positive electrode and none in the negative electrode. These initial guesses are shown in Table 4.5 and 4.6, for the linear and nonlinear

impedances, respectively. Those results are again, then seeded as the initial guess for the next SoC and the process is repeated until the 23% data is complete. In Figure 4.10, we show the results of these fits

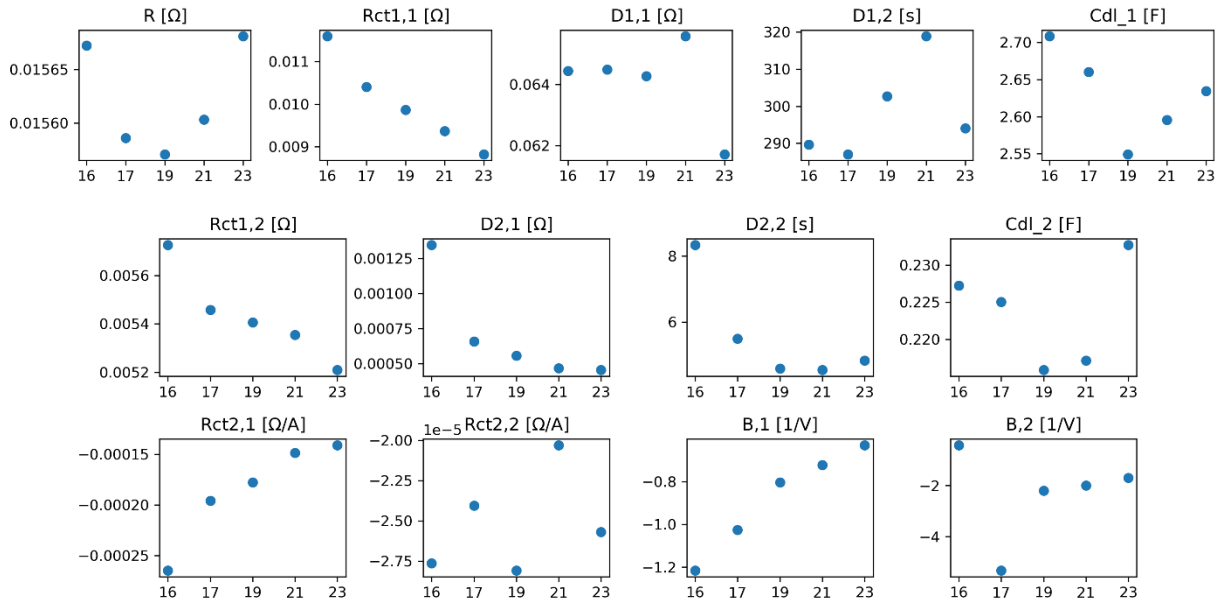

Figure 4.10 Plots of model parameter fits for the linear impedance (first row and second row) and the nonlinear impedance as a function of state-of-charge for the fresh-cell study. The top row includes parameters for the pure ohmic resistance and the Randle's circuit parameters for electrode 1. The middle row contains the Randle's circuit parameters for electrode 2. The bottom row shows parameters for the nonlinear circuit elements.

Here, we can see the effect of the increasing SoC on the electrode one, which we designate to be the positive electrode. We see that as the cell becomes more charged, the R_{CT1} value decreases, leading to a shrinking second arc at lower frequencies. While we do see a decrease in the R_{CT1} value for the negative electrode, the scale of the decrease seen in the positive electrode dominates the degradation seen in the kinetic response. However, the remaining transport parameters for the positive electrode and most of the parameters in the negative electrode, with the exception of the $D_{2,1}$ parameter which already is contributing an insignificant amount of impedance, remain constant. This is, for the most part, in parity with the behavior we see in the linear spectra, where neither the low-frequency tail nor the faster charge-transfer arc at the higher frequencies are shifting.

When we look at the nonlinear fitting parameters, we see the most prominent feature is $R_{CT2,1}$, or the second-harmonic charge-transfer resistance for the positive electrode, where it follows the same trend in decreasing magnitude with increasing lithiation. However, unlike the fresh cells, the fit $R_{CT,2}$ parameters for the negative and positive electrode are not on the same orders of magnitude, meaning that they do not cancel out, yielding the charge-transfer arc in the Nyquist plots shown in the Figure 4.9. This appreciable R_{CT2} parameter, especially in the positive electrode, means that there is a breaking of charge-transfer symmetry, or in other words, the electrode is no longer able to become oxidized with the same ease or difficulty as it is to become reduced. When we employ Equation 4.7 and 4.8 to determine the charge-transfer symmetry coefficients, we get that at all these SoCs, the α_a and α_c values for the positive electrode are about 0.4 and 0.6, respectively.

$$R_{CT2} = \frac{(\alpha_c^2 - \alpha_a^2)f}{4(\alpha_a + \alpha_c)} R_{CT1}^2 \quad [4.7]$$

$$1 = \alpha_c + \alpha_a \quad [4.8]$$

This shows that these reduced-order models are able to capture the breaking of charge-transfer symmetry, without the use for complicated physics-based models. However, it is much harder to discern a trend or pattern based off the lumped thermodynamic parameters. The positive electrode's differential voltage in this SoC range decreases in magnitude and has a change in concavity, leading to a local minimum in the second derivative, but does not exhibit any change in the sign of the second derivative. Instead, the negative electrode is traversing through three separate reaction peaks, leading to multiple peaks in the dV/dQ values, causing oscillating signs in the second derivative. However, when we look at the fit parameter (B_2), the value is only shrinking in magnitude, without the flipping of the sign of the magnitude like the second derivative should cause the B parameter to as shown in Equation 4.6.

To gain an understanding of how these parameters translate to the whole cell response, we use to model to disaggregate the two individual electrode's contribution to the linear and nonlinear impedance. Here, we show the linear and nonlinear impedance of the median SoC (19%) of the study, in Figure 4.11, where we have the experimental data plotted against the fits on the left-hand side, and then whole-cell fit and its disaggregated, individual electrodes on right-hand side. Overall, we see that the linear Randle's circuits capture the model data match exquisitely well and captures all the major features. In the nonlinear spectra, we see that the fit yields the charge-transfer

arc of similar width, our time constants still are not in parity, as evident by the fact that the model fit frequencies do not match as nicely as the first harmonic does, and that the highest frequency in the fit does not circle into the origin.

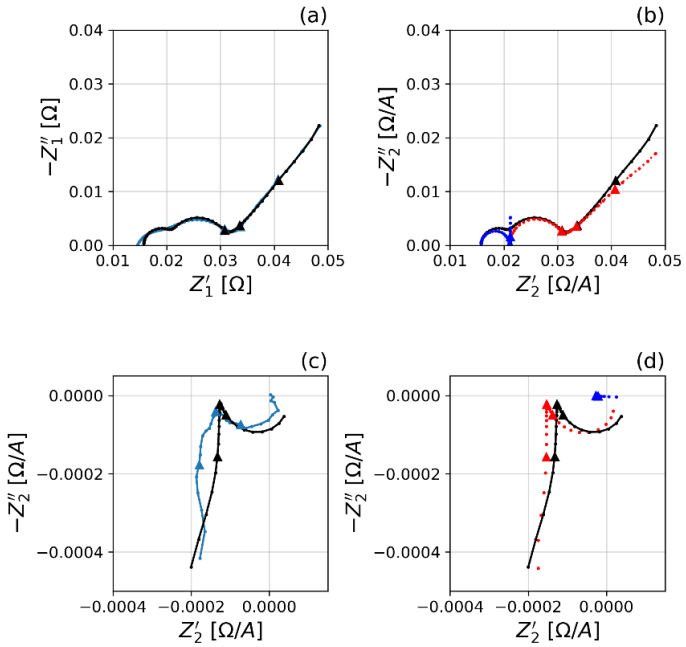

Figure 4.11 Nyquist plots showing the linear (a, b) and nonlinear (c, d) impedance for an aged-cell at 19% SoC. The left-hand side (a, c) show the spectra for the experimental data (light-blue) and the model fits from the equivalent circuit models (black). The right-hand side (b, d) show the model fit for the overall whole-cell response (black) and the two electrodes that make up the response, with the response dominated by the positive (red) electrode and not the negative (dark blue) electrode. (Δ) denote frequencies that are 1×10^{x}. The second harmonic data is truncated at 10 Hz

As evident by the parameters shown above, the negative electrode half-cell, in blue, contributes significantly less to the overall impedance response, and that the positive electrode is mainly responsible in both the linear and nonlinear spectra. In the nonlinear impedance, the positive electrode is responsible for the charge-transfer arc as well a majority of the low-frequency tail, with the negative electrode's contribution shifting it along the Z_2' axis. What we know, and can see from the negative electrode's Warburg element, is that if an electrode with fast transport leads to a vertical asymptote in the low-frequency response in the linear impedance, the nonlinear response is translated into a horizontal line, with the direction of the low-frequency response dictated by the sign of the lumped parameter. If we were to switch the sign of the B_2 parameter, we would see that the nonlinear response of the negative electrode would move along the -Z_2' axis rather what

we see in Figure 4.11. It is conceivable that the true value for the lumped thermodynamic parameter of the negative electrode is not truly captured. Based off Eq 4.6, we see that the lumped B is only related to the first and second-order derivatives with respect to the potential. We know from our experimental data and the MSMR model that the signs of the second derivative are constantly changing during this SoC window, meaning that the sign of the B parameter should be as well. Assuming the negative electrode behaves similarly in the real whole-cell, these slight directional changes in our thermodynamic tails of these sets of data could very well be explained by the small offsets along the positive or negative Z_2' axis caused by the second-harmonic Warburg element.

Table 4.3 Initial guesses for linear impedance fits for fresh-cell study

Parameter	Initial Guess
R	0.16 [Ω]
$R_{CT,1}$	0.005 [Ω]
$D_{1,1}$	0.07 [Ω]
$D_{1,2}$	300.0 [s]
$C_{DL,1}$	1.0 [F]
$R_{CT,2}$	0.005 [Ω]
$D_{2,1}$	0.00002 [Ω]
$D_{2,2}$	0.2 [s]
$C_{DL,2}$	0.1 [F]

Table 4.4 Initial guesses for nonlinear impedance fits for fresh-cell study

Parameter	Initial Guess
$R_{CT2,1}$	0.00 [Ω/A]
$R_{CT2,2}$	0.00 [Ω/A]
B_1	0.13 [1/V]
B_2	-44 [1/V]

Table 4.5 Initial guesses for linear impedance fits for aged-cell study

Parameter	Initial Guess
R	0.015 [Ω]
$R_{CT,1}$	0.01 [Ω]
$D_{1,1}$	0.007 [Ω]
$D_{1,2}$	300 [s]
$C_{DL,1}$	0.9 [F]
$R_{CT,2}$	0.005 [Ω]
$D_{2,1}$	0.00002 [Ω]
$D_{2,2}$	1 [s]
$C_{DL,2}$	1 [F]

Table 4.6 Initial guesses for nonlinear impedance fits for aged-cell study

Parameter	Initial Guess
$R_{CT2,1}$	-0.00156 [Ω/A]
$R_{CT2,2}$	0.00 [Ω/A]
B_1	-0.710 [1/V]
B_2	-21.7 [1/V]

4.4 Conclusions and Implications

A reduced-order model of NLEIS can lead to a quicker adoption of the techniques and analysis methods. Without relying on complicated P2D models to be solved in COMSOL or through other, equally rigorous calculations, NLEIS signals could be used to gain more information into phenomena that is not readily accessible in linear impedance, such as charge-transfer symmetry. While we do see that the linear impedance is well modeled by the Randle's circuits within these SoCs, the nonlinear impedance does not fully capture the correct time constants, as we can see that the points in the Nyquist plots for specific frequencies are not in parity. While the fitting with simplified Randle's circuits do show promise, there are still underlying principles that cannot be captured because of the complex nature of the physical electrode surface that a lumped model like ECMs cannot capture. This prompts the need for improved parameter estimation that uses both EIS and NLEIS, because linear impedance can be subjected to degeneracy, where the same solution can be achieved with multiple sets of parameters. Incorporation of NLEIS can benefit in two major ways. First, it helps break this degeneracy, and it could lead to a better, more accurate estimate of these first-order parameters because there is another criterion that these parameters must also account for. Second, by having access to the second-order derivatives, we can glean more thermodynamic information.

A natural extension to the work presented work would be to expand on an analog of the transmission-line model that has these nonlinear circuit elements included, allowing for the porous electrode to be better modeled and understood. Once these electrodes can be properly modeled, the implications of performing EIS at a certain open-circuit voltage, and then obtaining its first and second derivative allows us to reconstruct larger segments of open-circuit potential curve without the need for lengthy experiments. Instead, a single EIS experiment can provide information about kinetics, interfacial phenomena, and the local open-circuit curve in much faster measurement times than other traditional techniques.

Chapter 5 - Nonlinear electrochemical impedance spectroscopy of lithium-ion batteries: Experimental approach, analysis, and initial findings

Note: this chapter has been submitted as a preprint and has been accepted as a peer-reviewed article in the following citations.[24,134] *All data and code are found on the OSF project page.*[135]

- Murbach, M. D.; Hu, V.; Schwartz, D. T. *Nonlinear Electrochemical Impedance Spectroscopy of Lithium-Ion Batteries: Experimental Approach, Analysis, and Initial Findings*. ECSarXiv 2018. https://doi.org/10.17605/OSF.IO/T635X.
- Murbach, M. D.; Hu, V. W.; Schwartz, D. T. *Nonlinear Electrochemical Impedance Spectroscopy of Lithium-Ion Batteries: Experimental Approach, Analysis, and Initial Findings*. J. Electrochem. Soc. 2018, 165 (11), A2758–A2765. https://doi.org/10.1149/2.0711811jes.

Abstract

Nonlinear electrochemical impedance spectroscopy (NLEIS) is a moderate amplitude extension to linear EIS that provides a sensitive and complementary whole-battery diagnostic for charge transfer kinetics, mass transport, and thermodynamics. We present the first full-frequency, second harmonic NLEIS spectra for lithium-ion batteries using commercially available, 1.5 Ah LiNMC|C cells. The mathematical framework for NLEIS shows, and experiments confirm, that moderate-amplitude input modulations can generate a second harmonic output that does not intrinsically corrupt the linear EIS response. Experimental measurements at varied states-of-charge (SoC) and states-of-health (SoH) are used to illustrate and compare NLEIS and EIS data. At low frequencies, the second harmonic NLEIS spectrum is shown to produce a much more distinct response to SoC dependent thermodynamic and diffusion processes than linear EIS. By combining NLEIS and EIS, we are able to characterize degradation in early cell cycling (where cells lost <1% of initial capacity). We also show that NLEIS complements the characterization of charge transfer kinetics of linear EIS through the second harmonic sensitivity to symmetry. For example, NLEIS shows that fresh cells have high symmetry charge transfer ($\alpha_a = \alpha_c = 0.5$) on both electrodes, whereas early in the cycling there is a shift toward kinetics that favor oxidation on the positive electrode ($\alpha_{a,pos} > 0.5$, $\alpha_{c,pos} < 0.5$). Combined analysis of EIS and NLEIS spectra shows promise for improved parameter estimation and model validation. All experimental data and analysis code for this manuscript can be found on ECSarXiv.

5.1 Introduction

The unrelenting drive for higher energy and power dense lithium-ion batteries means the quantity of active materials is increasing at the same time separator thickness and electrolyte volume is decreasing.[136] Under these conditions, chemical and electrochemical interactions across the whole cell are critical for understanding and optimizing battery performance. Thus, there is a growing need for sensitive and selective *in situ* diagnostics that support fundamental studies of whole cells. Electrochemical impedance spectroscopy (EIS) is a powerful, noninvasive technique that works by applying a small current or voltage modulation and measuring the linear voltage or current response.[137] EIS has been used to characterize lithium-ion battery properties such as the solid-electrolyte interphase (SEI) layers,[55,138] mass transfer and kinetics of the electrode materials,[29,51] and degradative and capacity loss mechanisms.[30,139] EIS experiments are traditionally analyzed using equivalent circuit analogs, but linearized physics-based models are also available.[140–142] While EIS is a widely used and valuable technique, batteries are inherently *nonlinear* systems, and the linear nature of EIS can lead to degeneracy; that is, a single EIS dataset can often be represented equally well by different linear models[143] and circuit analogs.[59]

A natural extension to EIS uses moderately larger amplitude perturbations of current or voltage to drive the battery into a weakly nonlinear regime. This variant of EIS, which we call nonlinear EIS (NLEIS), breaks the degeneracy of linearization and contains complementary information to EIS.[143] In the weakly nonlinear regime, a moderate-amplitude, single-sine input of current or voltage produces one or more measurable (but small) higher harmonics of the fundamental frequency in the output Fourier spectrum. These higher harmonics have often been treated as evidence of a "corrupted" linear response to be eliminated from EIS measurements;[60,61,144–146] however, NLEIS spectra can be used to elucidate information about the nonlinear dynamics of a system that cannot be probed with EIS alone. NLEIS has previously been used in studies of corrosion,[64–66] fuel cell mechanisms,[69,143,147] mass transport-controlled systems,[72,148,149] chemical sensing,[74,75,150] as well as lithium-ion batteries.[76,151] Lvovich and Smiechowski were able to characterize degradation in industrial lubricants through monotonic trends in the second harmonic NLEIS responses, despite no noticeable trend in the linear responses.[78] Wilson et al. used physical models to distinguish the rate determining mechanism of the oxygen-reduction reaction on solid oxide fuel cell electrodes, despite the models being degenerate in their linear response.[143] Xu and

Riley demonstrated that the transfer coefficients, which have typically been experimentally difficult to determine, can be found through the use of even harmonics in the well-characterized ferri-ferrocyanide redox couple.[79] Heubner et al., further used the same principles to determine the transfer coefficients in lithium iron-phosphate electrodes.[80] Recently, higher harmonic responses in lithium-ion batteries have been studied through a total-harmonic distortion analysis to examine nonlinear Faradaic processes, and battery degradation.[76,152–154]

In these past studies, it is important to make distinctions between nonlinear measurements in the weakly nonlinear regime, where the measurable harmonics are few in number and orders of magnitude smaller than the fundamental response,[64–66,72,143,147–149,151] versus those studies that use much larger modulations of current or voltage and produce many harmonics within an order of magnitude of the fundamental response.[76,152–154] The NLEIS analysis presented here is only appropriate for the weakly nonlinear response.

NLEIS measurements are an interesting complement to EIS, in part, because the measurements do not necessarily require new equipment from traditional EIS.[61,79] Here we show how small changes in the experimental procedures and signal processing for EIS can allow researchers to calculate higher harmonic NLEIS spectra. These results are used in conjunction with an extension of the pseudo-two-dimensional (P2D) impedance battery model that includes the nonlinear harmonic response[151] to gain insight into the physicochemical behavior of commercial Samsung 18650 lithium-ion cells.

5.2 Experimental Methods and Signal Analysis

5.2.1 Cycling procedure of the lithium-ion battery

Cycling measurements on commercially available Samsung 1.5Ah LiNMC|C cells (INR 18650-15M) were made using a Maccor 4000M battery cycler in a controlled temperature environment of 25°C using a Maccor MTC-020 chamber. In these experiments, all cells were first subjected to five formation cycles using a C/2 charge and discharge rate within the specified voltage window (2.5 V to 4.2 V). To study the effects of aging, NLEIS measurements were conducted on new cells and cells that had been cycled for 100 cycles. The full cycles consisted of a 2C (3 A) constant current charge from 2.5 V (0% SoC) to 4.2 V (100% SoC), a constant voltage at 4.2 V until a 100mA current cutoff was reached, and a constant current discharge at 2C.

5.2.2 Measuring the nonlinear impedance of a lithium-ion battery

We demonstrate the full-spectrum application of nonlinear electrochemical impedance spectroscopy for batteries using an Autolab PGSTAT128N potentiostat/galvanostat with the frequency response analyzer module (Autolab FRA32). The measurements were made at a controlled temperature of 25°C and used a four-electrode configuration with voltage sensing at the cell terminals.

A single cosine current modulation waveform with frequency ω_1 and amplitude ΔI was sent to the galvanostat

$$I(t; \Delta I, \omega_1) = \Delta I \; Re\{\exp(j\omega_1 t)\}, \quad [5.1]$$

where $j = \sqrt{-1}$ and *Re* denotes the real component of the bracketed function. The notation $I(t; \Delta I, \omega_1)$ can be generalized as $X(a; b, c, \ldots)$ to show X is the dependent variable, a is an independent variable, and $b, c, \ldots$ are experimental parameters of the solution. The actual time domain current perturbation applied to the battery by the galvanostat, $I(t; \Delta I, \omega_1)$, and the measured voltage response, $V(t;\ \Delta I, \omega_1)$, were recorded using input modulations of 0.3, 0.4, and 0.5 A over a logarithmically spaced frequency range from 10 kHz to 3.16 mHz. Time domain data were recorded after the system had reached a steady-periodic state. A minimum of 10 steady-periodic cycles were logged with $N = 4096$ synchronous time domain measurements for both current and voltage. A rest time of 30 minutes was provided between each frequency sweep to provide a consistent baseline.

Measurements at specific states-of-charge were carried out by adding a specified amount of charge to a fully discharged battery (discharged to 2.5 V and held until the current reached 1 mA). The amount of charge to add was determined by capacity measurements at C/10 cycling. The voltages of specific states of charge were recorded after a four-hour rest to allow the cell to equilibrate.[155] For subsequent NLEIS experiments, each cell was charged to the desired voltage designated by the baseline (summarized in Table A1) through a C/10 rate, and then subjected to a two-hour constant voltage charge at the desired voltage. The cells were then allowed to equilibrate for an additional two hours at open circuit.

Fast Fourier transformation (FFT) of a steady-periodic input current of the form given by Equation 5.1, theoretically results in a very simple spectrum,

$$FFT\{I(t;\Delta I,\omega_1)\} = \Delta I, \quad [5.2]$$

at the frequency ω_1, and zero at all other frequencies. The resulting voltage spectrum, however, often contained complex Fourier coefficients at integer multiples, k, of the fundamental frequency, ω_1,

$$FFT\{V(t;\ \Delta I,\omega_1)\} = \tilde{V}(k\omega_1;\Delta I). \quad [5.3]$$

The experimental reality of our galvanostat was that harmonic distortions of the pure cosine current were introduced into the ideal spectrum given by Equation 5.2 when operated at higher frequencies and amplitudes, leading to an input current spectrum of the form:

$$FFT\{I(t;\Delta I,\omega_1)\} = \tilde{I}'(1\omega_1;\Delta I) + THD \quad [5.4]$$

where THD is the total harmonic distortion of the single sine input signal and $\tilde{I}'(1\omega_1;\Delta I)$ is the real Fourier coefficient at the fundamental frequency of the current perturbation (closely approximating ΔI). To ensure nonlinear experimental results presented here are from nonlinearity in the battery, not the power amplifier, we only report second harmonic data up to a frequency of 10 Hz for this instrument, where THD in the input was always below 1.0%. Linear EIS is reported for the entire frequency range.

The complex Fourier voltage spectrum had a pure harmonic structure comprised of signal at integer k values of the fundamental frequency ω_1. The lack of sub-harmonic ($0 < k < 1$) or anharmonic (non-integer k) output voltage spectrum indicated that the batteries (and measurement instrument) were stable, in all cases, to the finite amplitude current modulations. However, noise and imperfect sampling did lead to a small, continuous baseline in the spectrum. The baselines for the linear ($k = 1$) and second harmonic ($k = 2$) peaks were subtracted using a quadratic polynomial fit to several anharmonic baseline points adjacent to each harmonic peak of interest.

The amplitude of each voltage harmonic depends on the current modulation amplitude, ΔI. Prior research has shown that the weakly nonlinear response of the battery can be expressed as a power series in perturbation amplitude such that,[143,148,149]

$$\tilde{V}(k\omega_1;\Delta I) = \sum_{r=0}^{\infty} \Delta I^{k+2r} \tilde{Z}_{k,k+2r}(\omega_1) \quad [5.5]$$

where the resulting double indexed coefficients, $\tilde{Z}_{k,p}(\omega_1)$, are pure frequency dispersion coefficients – we will call them linear and nonlinear impedance coefficients – corresponding to harmonic number, k, and order, p. The double indexed coefficient $\tilde{Z}_{1,1}(\omega_1)$ is identically equal to the normal (linear) electrochemical impedance of the system. $\tilde{Z}_{2,2}(\omega_1)$ is the leading order nonlinear electrochemical impedance derived from the second harmonic of the voltage response to a pure cosine input current. The impedance coefficients for $p > k$, represent higher order corrections to the leading order $k = p$ solutions. In this work, we present an experimental and computational evaluation of the leading order terms in Equation 5.5,

$$\tilde{V}(1\omega_1;\Delta I) = \Delta I \tilde{Z}_{1,1}(\omega_1), \quad [5.6]$$

$$\tilde{V}(2\omega_1;\Delta I) = \Delta I^2 \tilde{Z}_{2,2}(\omega_1)\,. \quad [5.7]$$

From the complete form of Equation 5.5, it is possible to estimate how error scales when we truncate the series and use Equations 5.6 to determine the traditional linear electrochemical impedance, and Equation 5.7 to find the second harmonic NLEIS spectrum. Specifically, the error associated with using Equation 5.6 scales as $\sim\mathcal{O}(\Delta I^3)$ and the error from using Equation 5.7 scales as $\sim\mathcal{O}(\Delta I^4)$.

All of the data presented in this paper, including additional experiments showing reproducibility across several identical Samsung cells and data for analyzing the frequency-dependent galvanostat harmonic distortion, along with all of the software used for signal processing and analysis, can be found in the Supplementary Jupyter Notebook.[135]

5.3 Results

5.3.1 Current perturbation and voltage response signals

Typical time domain measurements of the input current and output voltage response from a Samsung high power NMC/C cell are shown for a frequency of $\omega_1 = 0.5$ Hz in Figure 1a and 1b, respectively, for three different current modulation amplitudes (ΔI = 0.1 A, 0.3 A, and 0.5 A). Time domain data of this nature, measured at different states of charge, frequencies, and amplitudes, are the raw data for our method.

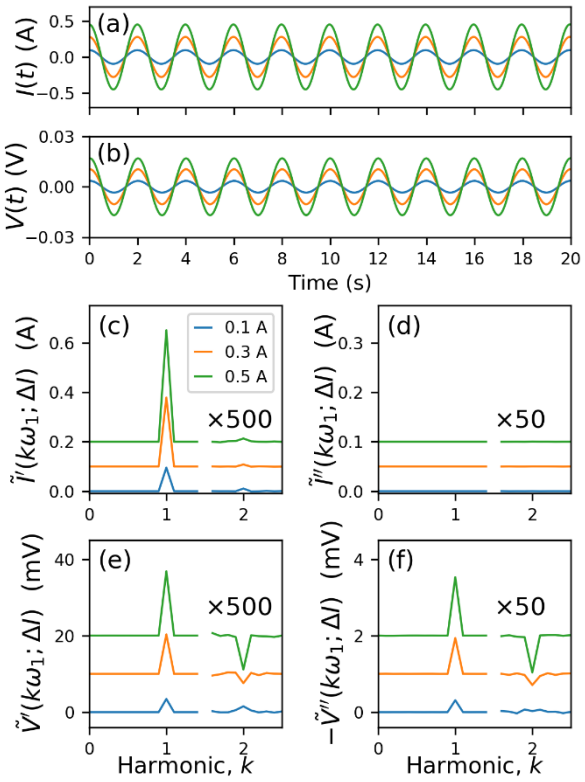

Figure 5.1. Measured time domain current (a) and voltage (b) response for a commercial 1.5 Ah LiNMC|C cell excited by a $\omega_1 = 0.5$ Hz current perturbation of varying amplitudes (ΔI) ranging from 0.1 A to 0.5 A. These signals are transformed into the frequency domain to enable analysis of the real (c, e) and imaginary (d, f) components at different harmonics, k. Offsets are added for clarity and the real and imaginary values for $k > 1.5$ are multiplied by 500 and 50, respectively, to be on the same scale. Voltage signal has mean open circuit value of 3.643 V subtracted.

In the time domain, the current (Figure 5.1a) appears to be a pure cosine. The output voltage response (Figure 5.1b) also appears to be a sinusoidal signal, with a phase and amplitude that depends on the input frequency and amplitude of the modulated current. For these high-power 1500 mAh cells, a current modulation of 100 mA is seen to produce a voltage modulation of about 4 mV around the open circuit voltage, whereas the largest current modulation of 500 mA produces roughly 20 mV of voltage modulation around the open circuit voltage. In EIS, a 4 mV modulation would be expected to fall in the linear response regime of nearly any electrochemical system. In contrast, a 20 mV modulation would generally be considered large enough to drive a weakly nonlinear response. For all of the NLEIS experiments reported here, we use current modulations between 300 and 500 mA; for the Samsung cells under test, the modulated voltages are in the 10s

of millivolts, or weakly nonlinear regime. We also do select experiments with 33 mA current modulation to determine impedances under traditional, very small amplitude linear conditions.

Details of the phase, amplitude, and harmonic content of the input current and output voltage signals are more evident in frequency domain spectra determined through FFT of the time domain signals, as shown in Figures 5.1c-f. The real and imaginary current spectra (Figure 5.1c and 5.d, respectively) show that the input is a purely real signal. A tiny amplifier-induced second harmonic signal ($k = 2$) is made evident by multiplying that portion of the spectrum by 500x, demonstrating that the actual galvanostat amplifier has a spectrum represented by Equation 5.4, but it is close to the ideal input given by Equation 5.2. In all that follows, we use the measured value $\tilde{I}'(1\omega_1; \Delta I)$ rather than the ideal value ΔI, when computing experimental impedances via Equations 5.6 and 5.7. As noted, the difference between the measured $\tilde{I}'(1\omega_1; \Delta I)$ and ΔI is generally small.

The real and imaginary frequency domain voltage spectra (Figure 5.1e and 5.f, respectively) show several features not easily seen in time domain measurements. In the frequency domain, the phase shift and magnitude of each harmonic in the voltage spectra can be quantified based by the magnitudes of the real and imaginary components. Qualitatively, one can see that the first harmonic in voltage grows linearly with $\tilde{I}'(1\omega_1; \Delta I)$ values from Figure 5.1c, as predicted by Equation 5.6. Likewise, the $k = 2$ second harmonic in voltage appears to grow at a super-linear rate with $\tilde{I}'(1\omega_1; \Delta I)$; Equation 5.7 suggests a quadratic dependence. The signs and ratios of the real and imaginary components for the $k = 2$ peaks are different than the $k = 1$ peaks at the fundamental frequency.

5.3.2 Amplitude dependence of voltage harmonics

To calculate the linear (traditional EIS) and nonlinear second harmonic impedance coefficients for the data in Figure 5.1 at frequency $\omega_1 = 0.5$ Hz, we use the real and imaginary $k = 1$ and $k = 2$ data along with Equations 5.6 and 5.7. Figure 2 shows the amplitude dependence of the voltage harmonics in Figures 1e and 1f, as a function of $\tilde{I}'(1\omega_1; \Delta I)$, the k=1 peak in Figure 1c. The impedance coefficients $\tilde{Z}_{1,1}(\omega_1)$ and $\tilde{Z}_{2,2}(\omega_1)$ are the best-fit coefficients from the polynomials in Equations 5.6 and 5.7, where $\tilde{I}'(1\omega_1; \Delta I)$ rather than ΔI is used. To retain the phase information in the double-indexed impedance coefficients, the real (Figure 5.2a) and imaginary (Figure 5.2b) components of the harmonic response are fit separately.

The solid lines in Figure 5.2 are the best-fit curves, and the dashed regions represent the extrapolations outside the three fit data points. The $k = 1$ line shows an independent, very small amplitude data point at 0.033 A, representing a measurement taken under conditions well away from any experimentally detectable voltage second harmonic. The 0.033 A points are seen to lie on the extrapolated linear fit made from the 0.3, 0.4, and 0.5 A data. The calculated $\tilde{Z}'_{1,1}$ value from fitting the three larger amplitude points in Figure 2a is $\tilde{Z}'_{1,1} = 37.31 \pm 0.45$ mΩ. The value measured from the traditional small amplitude 0.033 A modulation, where there is no $k = 2$ peak, is $\tilde{Z}'_{1,1} = 37.37$ mΩ, well within the confidence interval of the larger amplitude value. Moreover, all $\tilde{Z}_{1,1}(\omega_1)$ linear impedances calculated from the 0.3, 0.4, and 0.5 A points were found to satisfy Kramers-Kronig relations[156] to within 1.0% (see the Supplementary Jupyter Notebook).[135]

The results shown in Figure 5.2 are consistent across our wide range of frequency response data, and they support the hierarchical mathematical structure of Equation 5.5. Specifically, our results and the math show it is possible to *simultaneously, self-consistently, and accurately* determine the $\tilde{Z}_{1,1}$ spectrum from $k = 1$ voltage data (that scale with ΔI) and the $\tilde{Z}_{2,2}$ spectrum from $k = 2$ voltage data (that scales with ΔI^2), because the leading order truncation error in $\tilde{Z}_{1,1}$ scales with $\mathcal{O}(\Delta I^3)$. Stated another way, there is no fundamental reason the presence of an easily detected second harmonic in the voltage spectrum should be taken to indicate the linear impedance is corrupted by nonlinear effects. Instead, the math suggests that a cautionary signature of nonlinearity corrupting EIS is the presence of a third harmonic in the voltage spectrum (i.e., $k = 3$ signature), because that harmonic scales with ΔI^3, just like the truncation error in $\tilde{Z}_{1,1}$. The experimental implication is that we chose current modulation amplitudes of 0.3, 0.4, and 0.5 A because, for the battery under test, these values are a good compromise between measurable second harmonics but negligible third harmonics in the voltage spectra.

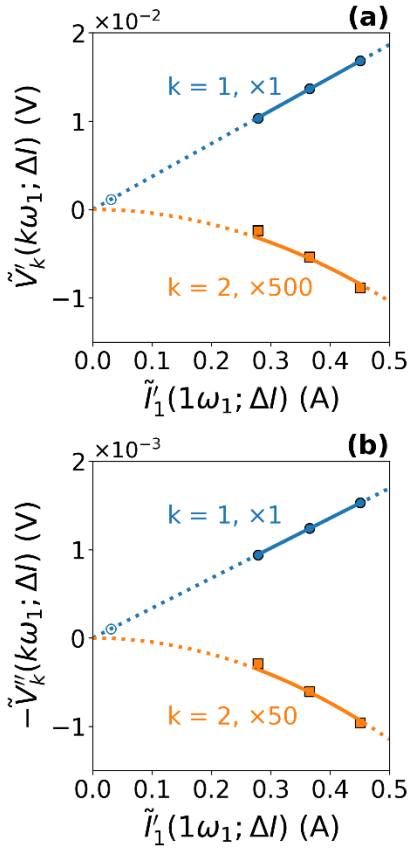

Figure 5.2 Amplitude dependence of the real (a) and imaginary (b) components of the Fourier transformed voltage response ($\omega_1 = 0.5$ Hz) as a function of the current perturbation amplitude, ΔI. The first (k = 1, ●) and second (k = 2, ■) voltage harmonics are fit to linear, $\tilde{I}'(1\omega_1;\Delta I)\tilde{Z}_{1,1}(\omega_1)$, and quadratic, $\tilde{I}'(1\omega_1;\Delta I)^2\tilde{Z}_{2,2}(\omega_1)$, functions of the measured perturbation amplitude, respectively. The real and imaginary second harmonic data are multiplied by 500x and 50x, respectively, to place them on the same scale as the linear response. The data are shown for cell 5 at 30% SoC.

As noted in the discussion of Equation 5.4, the galvanostat (like all amplifiers) is imperfect and generates harmonic distortions; these instrument-induced signals are expected to appear in the input current and output voltage spectra. To assess the magnitude and remove galvanostat-generated second harmonic in the voltage output, we use a $\tilde{Z}'_{1,1} = 21$ mΩ resistive wire that is comparable in magnitude to the impedance of the batteries under test but has no intrinsic nonlinear harmonic generating behavior. Using the same analysis of $k = 2$ voltage spectra as shown in Figure 5.2, we find the purely linear resistor produced a frequency invariant $\tilde{Z}^{in}_{2,2} = 4.56 \times 10^{-5} \frac{\Omega}{A}$ that can be entirely associated with the instrument. In all of the second harmonic NLEIS spectra

we report, this instrument value is subtracted from each $\tilde{Z}_{2,2}(\omega_1)$ point to remove the small instrument offset.

5.3.3 Nyquist representation of linear and nonlinear EIS spectra

Measuring the linear and nonlinear impedance coefficients over a range of frequencies provides insights into the system at different physicochemical timescales. Figure 5.3 shows a Nyquist representation of the experimentally measured linear EIS spectrum, $\tilde{Z}_{1,1}(\omega_1)$, and second harmonic NLEIS spectrum, $\tilde{Z}_{2,2}(\omega_1)$, for a fresh cell at 50% state-of-charge. The linear response shown in Figure 5.3a is a typical EIS spectrum for a lithium-ion battery. Figure 5.3a has a high frequency real-axis intercept (> 1 kHz) related to the internal resistance of the battery, a mid-range frequency arc ($\sim$1 kHz to 1 Hz) attributable to the coupled charge transfer kinetics and double-layer capacitance of the porous electrodes, and a low frequency tail (< 1Hz) attributable to diffusive transport and thermodynamics. The linear EIS spectra we are measuring can be thought of as the *sum* of two half-cell impedances for the positive and negative electrodes,

$$\tilde{Z}_{1,1} = \tilde{Z}^{+}_{1,1} + \tilde{Z}^{-}_{1,1}, \qquad [5.8]$$

where each half cell is defined at the mid-plane of the separator. Analysis of linear EIS spectra using equivalent circuit modeling is common in the literature, where circuit elements can be related to characteristics of the electrodes and separator.[137,140,157,158]

Prior work[151] shows that the second harmonic response is highly sensitive to several forms of symmetry in the system under test. The second harmonic NLEIS spectra we are measuring can be thought of as the *difference* between the half-cell impedances for the positive and negative electrodes,

$$\tilde{Z}_{2,2} = \tilde{Z}^{+}_{2,2} - \tilde{Z}^{-}_{2,2}\,. \qquad [5.9]$$

In a symmetric cell, where the positive and negative electrodes are identical, $\tilde{Z}_{2,2}$ will be identically zero for all frequencies. Of course, a functional battery is not a symmetric cell because thermodynamic differences in each electrode material largely defines the battery. Figure 5.3b shows that essentially all of the $\tilde{Z}_{2,2}$ response, for a fresh cell at 50% SoC, occurs at frequencies

below 1 Hz, where cell thermodynamics and diffusive transport are expected to be the dominating physics.

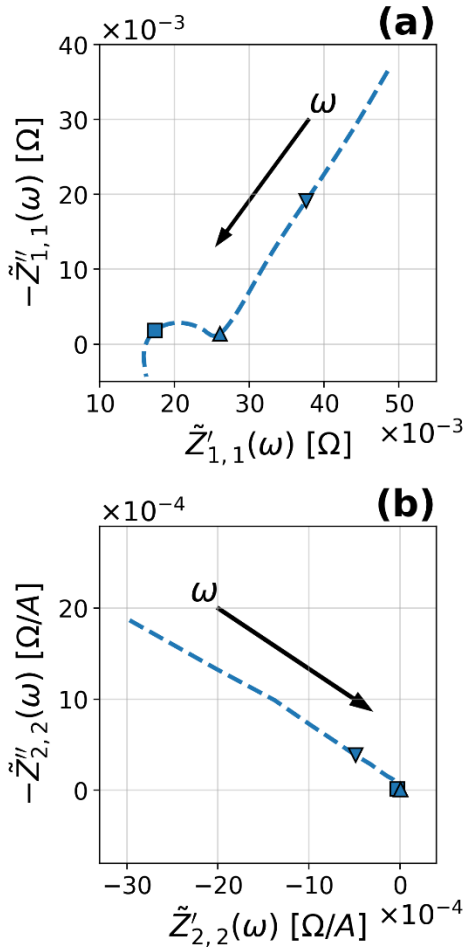

Figure 5.3 Nyquist plots of measured first (a) and second (b) harmonic coefficients, $\tilde{Z}_{1,1}(\omega_1)$ and $\tilde{Z}_{2,2}(\omega_1)$ of a "fresh" battery at 50% SoC. The data at 1 kHz (■), 1 Hz (▲), and 10 mHz (▼) are labeled for clarity.

In the mid-frequency regime (>1 Hz), where interfacial kinetic/capacitive processes dominate the linear EIS spectrum of Figure 5.3a, we see negligible $\tilde{Z}_{2,2}$ second harmonic response. In our full-physics model of lithium ion batteries, the lack of kinetic/capacitive response in $\tilde{Z}_{2,2}$ was attributed to high symmetry charge transfer where $\alpha_a = \alpha_c$ in the Butler-Volmer expression.[151] To get a basic understanding of charge transfer symmetry in the linear and nonlinear impedance, we carry out a Taylor series expansion of the Butler-Volmer equation,

$$j = i_0 \left[\exp\left(\frac{\alpha_a F}{RT}\eta\right) - \exp\left(\frac{-\alpha_c F}{RT}\eta\right) \right] \quad [5.10]$$

and include the first two terms

$$j = \left[\frac{i_0(\alpha_a+\alpha_c)F}{RT}\right]\eta + \left[\frac{i_0(\alpha_a{}^2-\alpha_c{}^2)F^2}{2R^2T^2}\right]\eta^2 + \mathcal{O}(\eta^3), \quad [5.11]$$

where i_0 is the exchange current density, α_a and α_c are the anodic and cathodic transfer coefficients, and F, R, and T are Faraday's constant, the gas constant, and the temperature, respectively. The first term on the right-hand side of Equation 5.11 is the inverse of the classic linear charge transfer resistance whereas the second term describes the leading order nonlinear behavior. Note that the second term is zero when charge transfer is symmetric with $\alpha_a = \alpha_c$, but can be either positive or negative when $\alpha_a \neq \alpha_c$.

The classic linear charge transfer resistance in EIS is insensitive to symmetry because $\alpha_a + \alpha_c$ is a constant (the number of electrons transferred) for each electrode. On the other hand, the second term of Equation 5.11, when combined with Equation 5.9, provides a symmetry-dependence that is consistent with our full-physics battery model behavior when $\alpha_a = \alpha_c$, $\alpha_a > \alpha_c$ or $\alpha_a < \alpha_c$ for either or both electrodes.[151] Thus, we can think of the second term in Equation 5.11 as being related to a "second harmonic charge transfer resistance" for each electrode. The absence of second harmonic NLEIS features at interfacial kinetic/capacitive frequencies in Figure 5.3b suggests charge transfer on both "fresh" electrodes is symmetric.

5.3.4 State-of-Charge (SoC) dependence for fresh cell

The full physics theory for linear EIS and second harmonic NLEIS includes explicit state-of-charge (SoC) dependence through derivatives of the open circuit potential of each electrode, and implicit dependence on parameters such as diffusivities, interfacial capacitances, and charge transfer parameters.[151] Specifically, linear EIS response depends on the first derivative of open circuit voltage with respect to intercalated lithium content; the first derivative is always negative for either electrode, but the magnitude can vary widely by material. The second harmonic NLEIS response depends on both the first and second derivative with respect to intercalated lithium content; the second derivative can be positive, negative, or zero for either electrode. As a result of the additional parameters, their varied signs, and the fact the response comes from differences

between electrodes, per Equation 5.9, our theory suggests that the thermodynamics/diffusion dominated regions of second harmonic NLEIS spectra can display a much richer set of SoC-dependent behaviors compared to the Warburg-like behavior expected for linear EIS.[151]

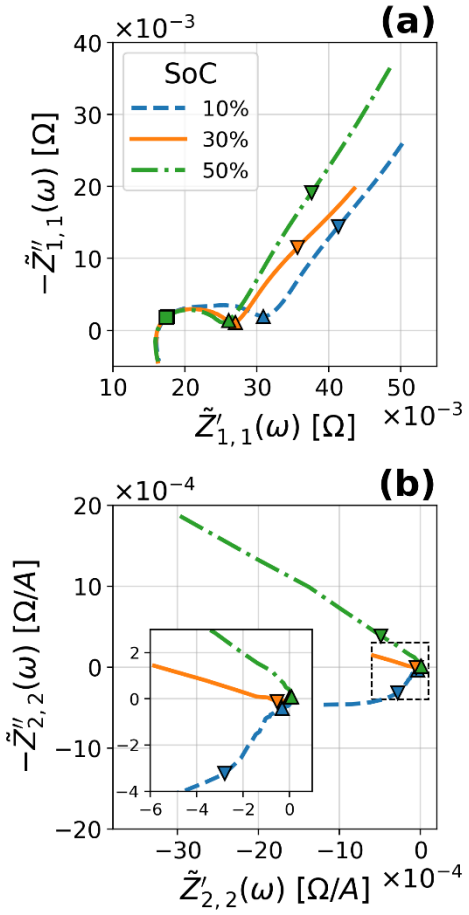

Figure 5.4 Nyquist plots of measured first (a) and second (b) harmonic coefficients, $\tilde{Z}_{1,1}(\omega_1)$ and $\tilde{Z}_{2,2}(\omega_1)$, for a "fresh" cell at several states-of-charge. The data at 1 Hz (△) and 10 mHz (▽) are labeled for clarity and the inset in (b) shows the region near the origin in more detail.

Figure 5.4 shows the linear EIS and second harmonic NLEIS spectra as the SoC is varied from 50% (same as Figure 3) to 10% in a fresh cell. The accompanying Supplemental Jupyter Notebook includes data for other states-of-charge, but they are excluded from Figure 5.4 for clarity.[135] The series of linear EIS spectra in Figure 5.4a all have characteristic mid-frequency arcs associated with interfacial kinetic/capacitive behavior ($\omega_1 > 1$Hz) and low frequency

thermodynamic/diffusive tails ($\omega_1 < 1\text{Hz}$). The interfacial charge transfer impedance grows systematically as the SoC is reduced. The low frequency EIS tail displays subtle changes in length with state-of-charge, being longest at 50% SoC, shortest at 30%, and longer again at 10%. Based on the full physics EIS model presented elsewhere, the mid-frequency changes are likely to be driven by SoC-dependent changes in exchange current density (i_0) and double-layer capacitance (C_{dl}) on one or both electrodes. The low frequency response is typically driven by SoC-dependent changes in the first derivative of open circuit voltage and solid-state diffusivity on one or both electrodes, though other transport processes can also come into play.[142,151] The effects of these changes are additive, per Equation (5.8).

The second harmonic spectra in Figures 5.4b show much greater variation in behavior than the linear EIS as the SoC changes. Despite large variation in the low-frequency region, none of the spectra show significant responses in the interfacial kinetic/capacitive regime ($\omega_1 > 1\text{Hz}$), see inset in Figure 5.4b. As discussed above, the lack of significant second harmonic response in the mid-frequency regime indicates symmetry of charge transfer over all states-of-charge tested. The complexity of the low-frequency second harmonic NLEIS response is not surprising given the increased number of parameters controlling the behavior, as described above. Moreover, the fact that the NLEIS spectrum results from differences in each electrode, Equation (5.9), means that subtle changes in one electrode can be amplified. In theory, this increased sensitivity to parameter changes improves parameter identifiability, but the more complex dependencies of NLEIS means that more sophisticated analysis is required. We will explore detailed SoC-dependent analysis and parameter estimation of NLEIS spectra in future work.

5.3.5 State-of-Health (SoH)

We have begun to explore the sensitivity of second harmonic NLEIS as a method for state-of-health (SoH) assessments. Figure 5.5 shows the linear EIS and second harmonic NLEIS spectra at 30% SoC for the fresh Samsung power cells and cells that have been charged and discharged at 2C for 100 cycles. The measured capacity loss from this cycle-dependent aging is only 0.8%. The small change in the overall capacity implies small changes to physicochemical processes in the battery.

EIS is known to be valuable for prognostic and diagnostic analysis of battery aging.[131] Here we see the linear EIS response in Figure 5.5a is noticeably changed in the mid-frequency kinetic/capacitive regime, despite less than 1% degradation of capacity. In particular, the mid-frequency impedance has grown, and two distinct arcs are now visible in the aged cell. For LiNMC|C cells, the growth of a second mid-frequency kinetic/capacitive arc from cycling is typically attributed to an increase in the positive NMC electrode charge transfer resistance.[139] The highest frequency arcs for fresh and aged cells continue to overlap in Figure 5.5a, suggesting negligible changes to the negative electrodes from 100 cycle aging. Likewise, aging related changes in the low frequency tail are extremely subtle.

While linear EIS provides useful insights, Figure 5.5b shows second harmonic NLEIS produces much greater changes from 100 cycle aging than linear EIS; we find all measurable frequencies are distinctly altered in the aged cell. In particular, the emergence of a mid-frequency response in the aged cell indicates a breaking of charge-transfer symmetry for at least one electrode. Combining the EIS interpretation with the new NLEIS results here suggests the positive NMC electrode ages with an increase in linear charge transfer resistance (*i.e.*, decreasing i_0) and that change is accompanied by a breaking of charge transfer symmetry (*i.e.*, $\alpha_a \neq \alpha_c$).

Previous full-physics theory results show that the "second harmonic charge transfer resistance", as we called it above, can be either positive or negative depending on the direction of charge transfer asymmetry and the electrode where that asymmetry arises.[151] Using these prior results, and attributing all the degradation to the positive electrode, means the charge transfer arc in Figure 5.5b arises from the anodic transfer coefficient, $\alpha_{a,pos}$, being larger than the cathodic transfer coefficient, $\alpha_{c,pos}$. For a positive electrode with $\alpha_{a,pos} > \alpha_{c,pos}$, oxidation (charging) is relatively easier (requires lower overpotential) than the equivalent reduction (discharging). This new insight into mechanistic changes in charge transfer cannot be determined from EIS alone, as linearization of the governing equations (and the governing physics) makes EIS wholly insensitive to charge transfer symmetry in either electrode.

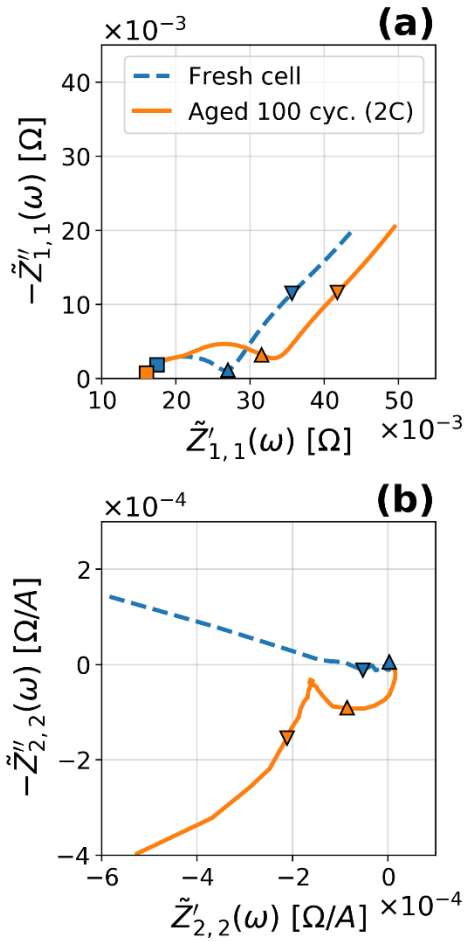

Figure 5.5 Nyquist plots of measured first (a) and second (b) harmonic coefficients, $\tilde{Z}_{1,1}(\omega_1)$ and $\tilde{Z}_{2,2}(\omega_1)$ for a fresh cell and a cell which has been cycled 100 times at 2C. The data at 1kHz (□), 1 Hz (△) and 10 mHz (▽) are labeled for clarity. The second harmonic data is truncated at 10 Hz. Cells are at 30% SoC.

As described in Figure 5.4b, the low frequency tail is sensitive to subtle changes in several thermodynamic and diffusive transport parameters for either or both electrodes. As noted above, the sensitive, multi-parameter nature of the NLEIS low frequency domain makes attention to modeling more essential for interpretation. Overall, second harmonic NLEIS appears to complement linear EIS as a method for probing degradation processes at the earliest stages of cycling.

5.3.6 Physics-based modeling of the EIS and NLEIS spectra

All of the experimental observations we have made in Figures 5.3-5.5 can be represented by our previously developed pseudo 2-dimensional (P2D) physics-based model for the linear EIS and second harmonic NLEIS response of a lithium-ion battery.[151] We are currently building up the computational tools needed for multi-parameter estimation of linear EIS and second harmonic NLEIS based on full-physics parameter estimation fit to experiments.[159] However, even without best-fit parameters, it is possible to qualitatively demonstrate that important characteristics of the linear and nonlinear response for the battery can be captured by the model. For example, Figure 5.6 shows simulated spectra that qualitatively mirror the EIS and NLEIS aging results presented in Figure 5.5; the two sets of model parameters are given in Table 5.2.

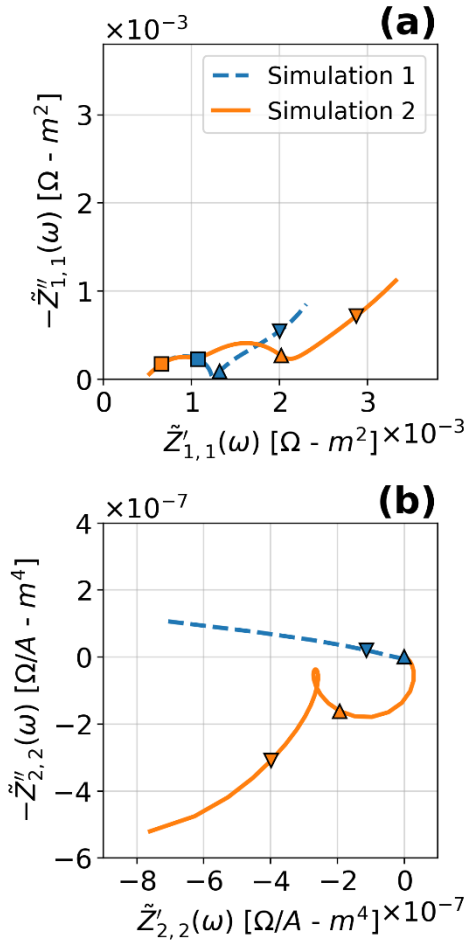

Figure 5.6 Nyquist plots of computed first (a) and second (b) harmonic coefficients, $\tilde{Z}_{1,1}(\omega_1)$ and $\tilde{Z}_{2,2}(\omega_1)$ from 3.16 mHz to 10kHz. The data at 1 kHz (□), 1 Hz (△), and 10 mHz (▽) are labeled for clarity.

In the aged cell experiments, the appearance of two distinct kinetic/capacitive arcs in the EIS spectrum was attributable to growth of the charge transfer resistance and an increase in the characteristic "RC" time constants for the positive electrode. The main way the model captures this aging affect is by a large reduction in positive electrode i_0 and large increase in double-layer capacitances C_{dl} for both electrodes. Changes to the charge transfer symmetry have no effect on the linear EIS. Further, looking at Table 5.2, we see that many of the thermodynamic and .diffusion parameters are changed for the aged cell, but these changes only produce subtle differences in the linear EIS spectrum at low frequencies, similar to the experimental observations in Figure 5.5a.

As noted in the discussion of Figure 5.5b, aging qualitatively changes everything about the second harmonic NLEIS spectrum; that behavior is mirrored by our model. As expected, symmetric charge transfer coefficients ($\alpha_a = \alpha_c = 0.5$), for both electrodes, produce a low frequency curve that goes straight toward the origin, as seen with the "fresh cell" model parameters. In this case, there are no mid-frequency kinetic/capacitive features. Introducing asymmetry in the transfer coefficients of the positive electrode, ($\alpha_{a,pos} = 0.55, \alpha_{c,pos} = 0.45$) results in the characteristic second harmonic kinetics arc seen in Figures 5b and 6b. At low frequencies, the changes in thermodynamic and diffusion coefficients for both electrodes drive a radically different low frequency second harmonic NLEIS response, despite having only modest impact on the linear EIS response.

The impact of charge transfer symmetry on the second harmonic signature is further illuminated in Figure 5.7. The effect of varying the positive electrode anodic transfer coefficient, $\alpha_{a,pos}$, for three cases where $\alpha_{a,pos} > \alpha_{c,pos}$, $\alpha_{a,pos} = \alpha_{c,pos}$, and $\alpha_{a,pos} < \alpha_{c,pos}$, is shown. The result shows that, depending on the nature of the asymmetry, the "second harmonic charge transfer resistance" can be positive or negative and its sign defines the quadrant of the resulting kinetic/capacitive arc. A similar, but inverted, dependence on symmetry exists for the negative electrode, because of the effect Equation (5.9) has on the total cell response. We are exploring scaling relationships and analytical approaches for relating the second term of Equation (5.11) to the quantity we refer to as the "second harmonic charge transfer resistance," which we think of as a nonlinear analog to the Randles' circuit; we will report on those results later.

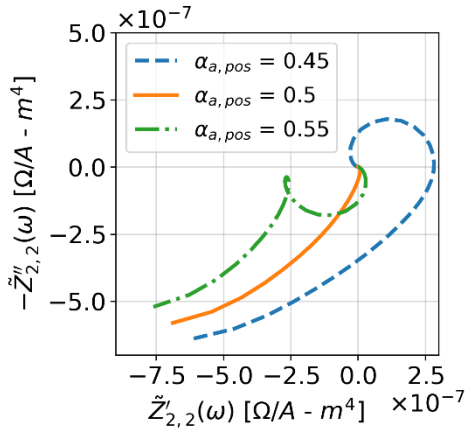

Figure 5.7 Nyquist plots of simulated second harmonic spectra, $\tilde{Z}_2(\omega_1)$ for varying positive electrode anodic transfer coefficients, $\alpha_{a,pos}$.

5.4 Conclusions and Implications

Nonlinear electrochemical impedance spectroscopy (NLEIS) can be implemented as an add-on to traditional linear EIS by using a modestly larger input current or voltage modulation and advanced signal processing. Our experiments and analysis show that NLEIS provides complementary information to EIS; this new information helps unlock insights into the charge-transfer kinetics, thermodynamics, and mass transport processes that govern lithium-ion batteries. We lay out experimental method and complications, as well as the mathematical framework for analysis of NLEIS. State-of-charge and state-of-health data for a fresh and cycled commercial Samsung LiNMC|C cell is used to illustrate the sensitivity of NLEIS.

There is a general notion that the existence of higher harmonics in the output voltage or current spectrum necessarily means EIS data is corrupted by nonlinear phenomenon.[60,78] Instead, we show that the general mathematical form of the weakly nonlinear regime does not support this as a universal premise. Specifically, the mathematical truncation error associated with a linear impedance measurement is $\sim\mathcal{O}(\Delta I^3)$, assuming current is modulated with amplitude ΔI, whereas the second harmonic output is an $\sim\mathcal{O}(\Delta I^2)$ signal. Thus, it is generally possible to find input modulation amplitudes where first order (EIS) and second order (second harmonic NLEIS) effects dominate third order effects (error in the EIS signal and third harmonic NLEIS). Of course, the exception to this statement is a symmetric electrochemical system with identical electrodes; the second harmonic output is identically zero at all frequencies for a symmetric cell. Fortunately, functional whole batteries are always asymmetric cells. For our experiments with 1500 mAh

power cells, input current modulations up to 500 mA produced fundamental peaks on the order of 10s of millivolts, second harmonics several orders of magnitude smaller, and no measurable third harmonic. Experiments showed that EIS results acquired under these conditions matched much smaller modulations, and satisfied Kramers-Kronig relationships to within 1% error at all frequencies.

It is worth reiterating here that instrumental limitations constrained the useable frequency range for second harmonic NLEIS spectra to $\omega_1 \leq 10$ Hz because of the total harmonic distortion that was generated by the galvantostat for these low impedance cells. Thus, we were unable to achieve high enough frequencies to fully probe the negative electrode kinetic/capacitive regime. It is worth noting, however, if the higher frequency electrode possessed asymmetric charge transfer, the effect would be reflected in the lower frequency second harmonic as a real axis offset from the origin. Consequently, improvements in instruments that enable larger current modulations for low impedance batteries are crucial for accurately probing smaller, and higher frequency, physicochemical processes with NLEIS.

A tantalizing view into the power of combining NLEIS experiments with NLEIS physics-based models was provided in the analysis of cell aging. We used a previously developed physics-based linear EIS and second harmonic NLEIS model to interpret the second harmonic response's sensitivity to charge transfer symmetry at mid-frequency ranges, as well as thermodynamic and mass transport parameters at low frequencies. The aged batteries, despite losing less than 1% of capacity from cycling, showed a fundamentally different signature in the nonlinear response due to the presence of asymmetric charge transfer kinetics. The measurable effects of the transfer coefficients, which have not been detectable in standard EIS, can now be monitored with aging, and at various states of the battery. This ability to measure fundamental aspects of charge transfer more completely, such as symmetry coefficients *in situ* and in whole cells, is a potentially important advance. We are working on the tools to extract quantitative parameters from combined EIS and second harmonic NLEIS.

5.5 Appendix

Table 5.1 Voltages for NLEIS measurements

State-of-Charge	10%	30%	40%	50%	60%
Voltage	3.500	3.643	3.706	3.820	3.920

Table 5.2 Physicochemical parameters for simulated fresh and aged cells

Parameter	**Fresh Cell Value [Units]**	**Aged Cell Value [Units]**
$C_{dl,n}$	10 [μF/cm^2]	50 [μF/cm^2]
$C_{dl,p}$	25 [μF/cm^2]	1000 [μF/cm^2]
c_0	1000 [mol/m^3]	1000 [mol/m^3]
D	1.5E-10 [m^2/s]	7.5E-10 [m^2/s]
$D_{s,n}$	3.9E-14 [m^2/s]	9.8E-15 [m^2/s]
$D_{s,p}$	1.0E-14 [m^2/s]	2.5E-15 [m^2/s]
$\frac{dU_n}{dc^s}$	0 [V·cm^3/mol]	-3.21 [V·cm^3/mol]
$\frac{dU_p}{dc^s}$	-10 [V·cm^3/mol]	-11.7 [V·cm^3/mol]
$\frac{d^2U_n}{dc^{s2}}$	-100 [V·cm^3/mol]	-400 [V·cm^3/mol]
$\frac{d^2U_p}{dc^{s2}}$	0 [V·cm^3/mol]	-600 [V·cm^3/mol]
$i_{0,n}$	29.7 [A/m^2]	14.85 [A/m^2]
$i_{0,p}$	33.0 [A/m^2]	5.51 [A/m^2]
t_+^0	0.364 [–]	0.364 [–]
$\alpha_{a,n}$	0.5 [–]	0.5 [–]
$\alpha_{a,p}$	0.5 [–]	0.55 [–]
$\alpha_{c,n}$	0.5 [–]	0.5 [–]
$\alpha_{c,p}$	0.5 [–]	0.45 [–]
κ	0.205 [S/m]	0.205 [S/m]
σ_n	100 [S/m]	100 [S/m]
σ_p	100 [S/m]	100 [S/m]

Table 5.3 Geometric parameters for simulated fresh and aged cells

Parameter	Fresh Cell Value [Units]	Aged Cell Value [Units]
l_n	88 [μm]	88 [μm]
l_s	25 [μm]	25 [μm]
l_p	80 [μm]	80 [μm]
R_n	2 [μm]	2 [μm]
R_p	2 [μm]	2 [μm]
$\epsilon_{f,n}$	0.0326 [–]	0.0326 [–]
$\epsilon_{f,p}$	0.025 [–]	0.025 [–]
ϵ_n	0.485 [–]	0.485 [–]
ϵ_s	0.724 [–]	0.724 [–]
ϵ_p	0.385 [–]	0.385 [–]

Chapter 6 - Conclusions and future work

In order to advance further battery research and improve our understanding of the different types of aging that can occur in lithium-ion batteries, we must continue to develop and expand upon whole-cell diagnostic techniques and models. One way to rapidly improve the pace of these methods and tool development is to have a large repository of open data where researchers can use and properly cite. This can allow for model and tool developers to test and validate their methods on replicate data or even cells of different chemistries without the need to expend time and resources on collecting data that may already exist. In our work, we aimed to provide the community with a dataset with cycling, open-circuit estimates, and impedance data across replicate cells for a ubiquitous battery chemistry, NMC | Graphite, that the battery community will have access to. For our own work, we used the open-circuit voltage and its subsequent differential voltage to test and validate the Multi-Species, Multi-Reaction model that we converted from the half-cell framework into the whole-cell paradigm via inclusion of whole-cell design parameters. We fit the model to these slow-scans at various states-of-health and were able to investigate the electrodes' thermodynamic behaviors with aging and how those propagate into the emergent properties that come with the whole-cell design. Finally, we were also able to expand upon traditional impedance by developing the experimental methods for the natural extension, NLEIS. To analyze these new data, we used both new nonlinear equivalent circuit methods as well as more complicated, full physics-based modelling to mirror the spectra we see in the EIS and NLEIS spectra.

6.1 Advancing open battery data

With lithium-ion batteries becoming increasingly commonplace in everyday applications, it is no surprise that there is an increasing demand for battery data and characterization and diagnostic tools to provide insight into the internal states. In the research community, open-data has not kept pace with the exponential adoption of lithium-ion batteries. Here, we sought to collect an battery dataset using NMC | Graphite cells, which can be found in many commercial devices and battery packs. We aimed to look at how different temperatures and different charging C-rates affect the aging of these cells, and we collected reference performance data at intermediate SoHs with open-circuit potential estimations and impedance measurements. We also prioritized

collecting replicate cell data for each SoH for each condition to capture the experimental variation in these cells, respectively, as this is not commonly seen in many open-datasets. An important implication of collecting replicate data is to try and understand these experimental variations, which when determined, can provide users with confidence intervals or windows of when the cells are operating safely. Thus, in the instance where a cell is degrading abnormally, either through external or excessive stress or manufacturing flaws, it can be easily detected well before any noticeable safety hazards occur.

While still in progress, the aim of this work is to publish it into an open-data repository, following the guidelines laid out in the Battery Data Genome Project.[91] We believe that in doing so, we are removing a time and resource-intensive step for researchers by supplying the community with a dataset on a popular chemistry that can be used to speed up model development and machine learning techniques. For example, machine learning studies, like the one developed by Severson et al[86] can be further validated by using the input parameters found in their work to see if our batteries' lifetimes can be predicted at the beginning of life. Furthermore, these data include open-circuit data estimates, EIS, and NLEIS measurements. While the work on NLEIS was done primarily on cells that have undergone very little degradation (100 cycles, < 1% capacity fade), yet show incredible, emergent effects. The data collected in this dataset contain spectra for cells at widely different SoHs, allowing us to further examine NLEIS spectra and possibly features that had not yet emerged with our limited cycling.

6.2 Whole-Cell Modeling with the Multi-Species, Multi-Reaction model

There is an increasing need for proper, whole-cell diagnostics in real-world applications, such as in electric vehicles, where postmortem analysis and subsequent half-cell studies are not a viable option. Here, we took the Multi-Species, Multi-Reaction model, developed by Verbrugge et al., and converted it into a whole-cell model using additional design parameters, such as total capacity loadings, lithiation ranges, and usable capacity within set voltage limits. Here, we were able to take open-circuit and differential voltage data at different SoHs from our dataset for one charge C-Rate and temperature and fit the whole-cell MSMR model. We were then able to examine how both the fundamental thermodynamic reactions, design parameters, and emergent properties

change with increased cycling. Using this model, we are able to estimate how the fundamental reactions and phase transitions within each electrode are degrading, using an accessible measurement and without the need for destructive testing or expensive crystallography or synchrotron experiments.

While the framework is mainly assessed against insertion electrodes, Verbrugge et al., has used the model to analyze different reaction systems, such as conversion electrodes. This makes the MSMR model increasingly valuable, as it can incorporate additional reaction schemes, allowing it to remain a viable analysis tool with new discoveries and achievements. As long as there is an open-library of available, well-procured half-cell data, the MSMR model can be seeded with relevant fundamental starting parameters for any electrode and used to study the whole-cell characteristics that emerge.

To improve upon this work, Baker et al., has expanded on this thermodynamic framework to incorporate kinetic and transport properties that can allow for increased accuracy of the model. Given that the OCV estimates in this work were derived from a dynamic, albeit very slow, operation, there is still an inherent offset generated by the overpotentials that occur at any passage of current. Especially since the whole-cell response is made up of the two electrodes, the inclusion of these important physical and chemical properties can reduce these overpotentials on both electrodes and yield more accurate parameters.

Furthermore, we know from experience that the charge and discharge curves are not equivalent, and that there is some inherent hysteresis as shown in Figure 6.1. We can see that the locations of the peaks are shifted, which is to be expected with the hysteresis, but the height of the peaks also differ, particularly in the graphite peaks. This could be indicative of an asymmetric reaction, where one direction, lithiation or delithiation, may be favored, proving to be ideal points of study with techniques such as NLEIS. In addition, the MSMR model can provide relevant thermodynamic information on the two electrodes for further analyses, as shown in the EIS/NLEIS fitting with equivalent circuits.

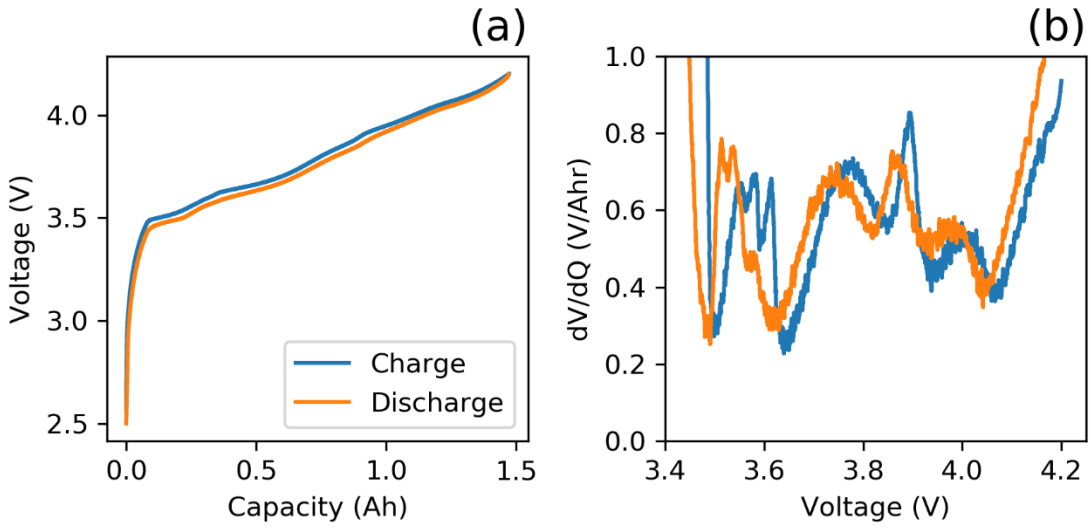

Figure 6.1 Open-circuit voltage data vs capacity (a) and the differential voltage (dV/dQ) vs voltage (b) for the two separate charge and discharge steps in the C/20 scans for a fresh cell.

6.3 Linear and nonlinear electrochemical impedance spectroscopy

In this work, we demonstrate that by simply increasing the input signal of an AC signal to a more-moderate amplitude, we can extract second harmonic signals, or nonlinear responses, without invalidating the linear impedance. While the incorporation of NLEIS experimental methods can be straightforward, without the need for any additional equipment, the models and data analysis can be significantly more complicated. However, we are still able to extract out new information that was previously invisible in the linearized technique, such as the breaking of charge-transfer symmetry in our electrodes, even with limited degradation. Here, we demonstrate that the inclusion of new, nonlinear circuit elements can be used in conjunction with the linearized equivalent circuit methods, to yield fit spectra for both the first and second-harmonic impedance. While not as flexible or tunable as the full-physics, pseudo-2-dimensional based COMSOL model, the equivalent circuit elements can model similar features at a much reduced-order and complexity.

While the equivalent circuits do a great job at capturing the linear impedance behavior in our tight SoC window studies in Chapter 4, it can be seen that there is still room for improvement, as the timescales in the nonlinear impedance do still differ between the fits and experimental data. In addition, these lumped thermodynamic parameters in the nonlinear impedance fits may not

accurately reflect the true thermodynamics of the electrode, as illustrated by the fact the B parameter remains negative in the aged studies, but based off the MSMR models, should be oscillatory in signs. For this work, fitting was done sequentially, where the linear impedance was fit first, and then these were held constant and used to fit the new nonlinear impedance parameters. Since ECMs in the linear impedance can be degenerate, multiple parameter sets can yield the same fit and solution. Thus, to improve the confidence of these fits in the linear regime and to improve the accuracy of the second-harmonic fit, a co-optimization could be implemented, where all the parameters are allowed to vary, with the hopes of finding solutions that match the timescales in both spectra.

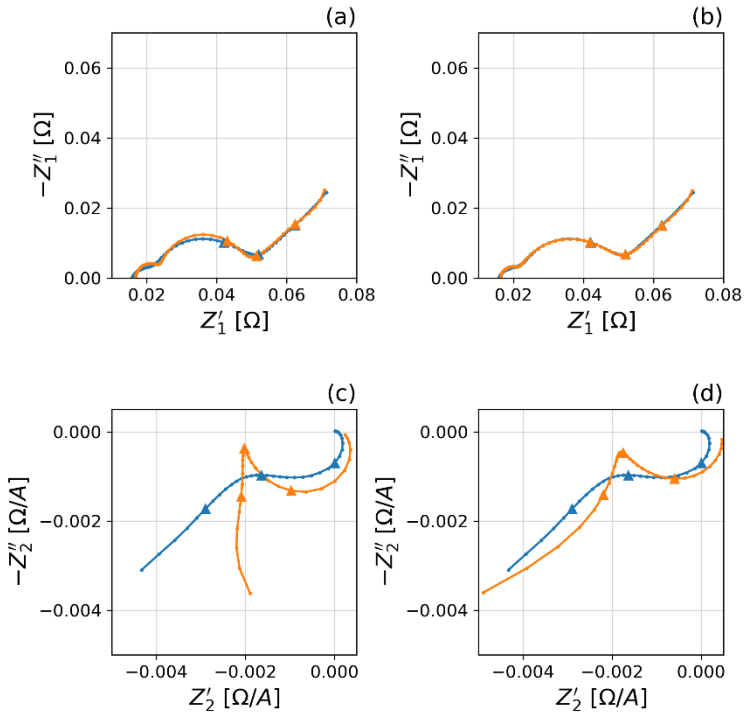

Figure 6.2 Nyquist plots showing the linear (a, b) and nonlinear (c, d) impedance for an aged-cell at 10% SoC. The left-hand side (a, c) show the spectra for the experimental data (light-blue) and the model fits from the equivalent circuit models (orange) when using two Randle's circuits with double-layer capacitances. The right-hand side (b, d) show the spectra for the same experimental data (light-blue) and the model fits from the equivalent circuit models (orange) when using one Randle's circuits and one circuit where the double-layer capacitance on the sluggish electrode is replaced with a constant-phase element. (Δ) denote frequencies that are 1×10^{x}. The second harmonic data is truncated at 10 Hz.

Finally, the impedance spectra collected in both of the fresh and the aged SoC studies were well modeled using just Randle's circuits, but in the limiting case of 10%, where we approach a

lithiation boundary, these elements can no longer accurately model the exhibited behavior. This could arise from porous electrode behavior, where inhomogeneity in the current distribution across the electrode can lead to drastically different responses than a perfectly uniform electrode. This can be seen in Fig 6.2a and 6.2c, where the same equivalent circuits with the two Randle's circuits for the two electrodes were used to try and fit the 10% impedance spectra, but the charge-transfer arc appears too large and the nonlinear Warburg element is not well captured, despite good parity in the linear impedance. One way to try and address the porous electrode behavior is to use a constant-phase element, which depresses the semicircles, to better match the response. While we see a much better fit in the linear impedance, particularly in the more sluggish electrode, there is still a separation in the charge-transfer and transport regimes in the nonlinear response. This spurs the need for further improved models in these limiting cases where the porous electrode behavior dominates the impedance response. One way would be to use full-physics based modelling with complicated models like the P2D model, but this can become inaccessible and overly complex for the experimental community. Instead, a good extension of the equivalent circuit methods would be to develop transmission-line models with the necessary nonlinear additions to help capture the porous electrode behavior.

Bibliography

(1) Kåberger, T. Progress of Renewable Electricity Replacing Fossil Fuels. *Global Energy Interconnection* **2018**, *1* (1), 48–52. https://doi.org/10.14171/j.2096-5117.gei.2018.01.006.

(2) Budischak, C.; Sewell, D.; Thomson, H.; Mach, L.; Veron, D. E.; Kempton, W. Cost-Minimized Combinations of Wind Power, Solar Power and Electrochemical Storage, Powering the Grid up to 99.9% of the Time. *Journal of Power Sources* **2013**, *225*, 60–74. https://doi.org/10.1016/j.jpowsour.2012.09.054.

(3) Goodenough, J. B.; Park, K.-S. The Li-Ion Rechargeable Battery: A Perspective. *J. Am. Chem. Soc.* **2013**, *135* (4), 1167–1176. https://doi.org/10.1021/ja3091438.

(4) Rowden, B.; Garcia-Araez, N. Estimating Lithium-Ion Battery Behavior from Half-Cell Data. *Energy Reports* **2021**, *7*, 97–103. https://doi.org/10.1016/j.egyr.2021.02.048.

(5) Gilbert, J. A.; Bareño, J.; Spila, T.; Trask, S. E.; Miller, D. J.; Polzin, B. J.; Jansen, A. N.; Abraham, D. P. Cycling Behavior of NCM523/Graphite Lithium-Ion Cells in the 3–4.4 V Range: Diagnostic Studies of Full Cells and Harvested Electrodes. *J. Electrochem. Soc.* **2017**, *164* (1), A6054–A6065. https://doi.org/10.1149/2.0081701jes.

(6) Bak, S.-M.; Shadike, Z.; Lin, R.; Yu, X.; Yang, X.-Q. In Situ/Operando Synchrotron-Based X-Ray Techniques for Lithium-Ion Battery Research. *NPG Asia Mater* **2018**, *10* (7), 563–580. https://doi.org/10.1038/s41427-018-0056-z.

(7) Verbrugge, M.; Baker, D.; Xiao, X. Formulation for the Treatment of Multiple Electrochemical Reactions and Associated Speciation for the Lithium-Silicon Electrode. *J. Electrochem. Soc.* **2016**, *163* (2), A262–A271. https://doi.org/10.1149/2.0581602jes.

(8) Schulze, M. C.; Neale, N. R. Half-Cell Cumulative Efficiency Forecasts Full-Cell Capacity Retention in Lithium-Ion Batteries. *ACS Energy Lett.* **2021**, *6* (3), 1082–1086. https://doi.org/10.1021/acsenergylett.1c00173.

(9) Weber, R.; Fell, C. R.; Dahn, J. R.; Hy, S. Operando X-Ray Diffraction Study of Polycrystalline and Single-Crystal LixNi0.5Mn0.3Co0.2O2. *J. Electrochem. Soc.* **2017**, *164* (13), A2992. https://doi.org/10.1149/2.0441713jes.

(10) Armand, M.; Tarascon, J.-M. Building Better Batteries. *Nature* **2008**, *451*, 652–657. https://doi.org/10.1038/451652a.

(11) Nölle, R.; Beltrop, K.; Holtstiege, F.; Kasnatscheew, J.; Placke, T.; Winter, M. A Reality Check and Tutorial on Electrochemical Characterization of Battery Cell Materials: How to Choose the Appropriate Cell Setup. *Materials Today* **2020**, *32*, 131–146. https://doi.org/10.1016/j.mattod.2019.07.002.

(12) Kim, C.-S.; Jeong, K. M.; Kim, K.; Yi, C.-W. Effects of Capacity Ratios between Anode and Cathode on Electrochemical Properties for Lithium Polymer Batteries. *Electrochimica Acta* **2015**, *155*, 431–436. https://doi.org/10.1016/j.electacta.2014.12.005.

(13) Kasnatscheew, J.; Placke, T.; Streipert, B.; Rothermel, S.; Wagner, R.; Meister, P.; Laskovic, I. C.; Winter, M. A Tutorial into Practical Capacity and Mass Balancing of Lithium Ion Batteries. *J. Electrochem. Soc.* **2017**, *164* (12), A2479–A2486. https://doi.org/10.1149/2.0961712jes.

(14) Chen, S.; Niu, C.; Lee, H.; Li, Q.; Yu, L.; Xu, W.; Zhang, J.-G.; Dufek, E. J.; Whittingham, M. S.; Meng, S.; Xiao, J.; Liu, J. Critical Parameters for Evaluating Coin Cells and Pouch Cells of Rechargeable Li-Metal Batteries. *Joule* **2019**, *3* (4), 1094–1105. https://doi.org/10.1016/j.joule.2019.02.004.

(15) Long, B. R.; Rinaldo, S. G.; Gallagher, K. G.; Dees, D. W.; Trask, S. E.; Polzin, B. J.; Jansen, A. N.; Abraham, D. P.; Bloom, I.; Bareño, J.; Croy, J. R. Enabling High-Energy, High-Voltage Lithium-Ion Cells: Standardization of Coin-Cell Assembly, Electrochemical Testing, and Evaluation of Full Cells. *J. Electrochem. Soc.* **2016**, *163* (14), A2999. https://doi.org/10.1149/2.0691614jes.

(16) Murray, V.; Hall, D. S.; Dahn, J. R. A Guide to Full Coin Cell Making for Academic Researchers. *J. Electrochem. Soc.* **2019**, *166* (2), A329–A333. https://doi.org/10.1149/2.1171902jes.

(17) Nordh, T.; Younesi, R.; Hahlin, M.; Duarte, R. F.; Tengstedt, C.; Brandell, D.; Edström, K. Manganese in the SEI Layer of Li4Ti5O12 Studied by Combined NEXAFS and HAXPES Techniques. *J. Phys. Chem. C* **2016**, *120* (6), 3206–3213. https://doi.org/10.1021/acs.jpcc.5b11756.

(18) Jung, R.; Linsenmann, F.; Thomas, R.; Wandt, J.; Solchenbach, S.; Maglia, F.; Stinner, C.; Tromp, M.; Gasteiger, H. A. Nickel, Manganese, and Cobalt Dissolution from Ni-Rich NMC and Their Effects on NMC622-Graphite Cells. *J. Electrochem. Soc.* **2019**, *166* (2), A378. https://doi.org/10.1149/2.1151902jes.

(19) Jang, D. H.; Shin, Y. J.; Oh, S. M. Dissolution of Spinel Oxides and Capacity Losses in 4 V Li / Li x Mn2 O 4 Cells. *J. Electrochem. Soc.* **1996**, *143* (7), 2204–2211. https://doi.org/10.1149/1.1836981.

(20) Barai, A.; Uddin, K.; Dubarry, M.; Somerville, L.; McGordon, A.; Jennings, P.; Bloom, I. A Comparison of Methodologies for the Non-Invasive Characterisation of Commercial Li-Ion Cells. *Progress in Energy and Combustion Science* **2019**, *72*, 1–31. https://doi.org/10.1016/j.pecs.2019.01.001.

(21) Harlow, J. E.; Ma, X.; Li, J.; Logan, E.; Liu, Y.; Zhang, N.; Ma, L.; Glazier, S. L.; Cormier, M. M. E.; Genovese, M.; Buteau, S.; Cameron, A.; Stark, J. E.; Dahn, J. R. A Wide Range of Testing Results on an Excellent Lithium-Ion Cell Chemistry to Be Used as Benchmarks for New Battery Technologies. *J. Electrochem. Soc.* **2019**, *166* (13), A3031. https://doi.org/10.1149/2.0981913jes.

(22) Dugas, R.; Forero-Saboya, J. D.; Ponrouch, A. Methods and Protocols for Reliable Electrochemical Testing in Post-Li Batteries (Na, K, Mg, and Ca). *Chem Mater* **2019**, *31* (21), 8613–8628. https://doi.org/10.1021/acs.chemmater.9b02776.

(23) Bloom, I.; Walker, L. K.; Basco, J. K.; Abraham, D. P.; Christophersen, J. P.; Ho, C. D. Differential Voltage Analyses of High-Power Lithium-Ion Cells. 4. Cells Containing NMC. *Journal of Power Sources* **2010**, *195* (3), 877–882. https://doi.org/10.1016/j.jpowsour.2009.08.019.

(24) Murbach, M. D.; Hu, V. W.; Schwartz, D. T. Nonlinear Electrochemical Impedance Spectroscopy of Lithium-Ion Batteries: Experimental Approach, Analysis, and Initial Findings. *J. Electrochem. Soc.* **2018**, *165* (11), A2758–A2765. https://doi.org/10.1149/2.0711811jes.

(25) Waldmann, T.; Scurtu, R.-G.; Richter, K.; Wohlfahrt-Mehrens, M. 18650 vs. 21700 Li-Ion Cells – A Direct Comparison of Electrochemical, Thermal, and Geometrical Properties. *Journal of Power Sources* **2020**, *472*, 228614. https://doi.org/10.1016/j.jpowsour.2020.228614.

(26) Liu, C.; Neale, Z. G.; Cao, G. Understanding Electrochemical Potentials of Cathode Materials in Rechargeable Batteries. *Materials Today* **2016**, *19* (2), 109–123. https://doi.org/10.1016/j.mattod.2015.10.009.

(27) Inzelt, G. Crossing the Bridge between Thermodynamics and Electrochemistry. From the Potential of the Cell Reaction to the Electrode Potential. *ChemTexts* **2014**, *1* (1), 2. https://doi.org/10.1007/s40828-014-0002-9.

(28) Chen, Y.; Wang, L.; Anwar, T.; Zhao, Y.; Piao, N.; He, X.; Zhu, Q. Application of Galvanostatic Intermittent Titration Technique to Investigate Phase Transformation of LiFePO4 Nanoparticles. *Electrochimica Acta* **2017**, *241*, 132–140. https://doi.org/10.1016/j.electacta.2017.04.137.

(29) Levi, M. D.; Aurbach, D. Diffusion Coefficients of Lithium Ions during Intercalation into Graphite Derived from the Simultaneous Measurements and Modeling of Electrochemical Impedance and Potentiostatic Intermittent Titration Characteristics of Thin Graphite Electrodes. *J. Phys. Chem. B* **1997**, *101* (23), 4641–4647. https://doi.org/10.1021/jp9701911.

(30) Tröltzsch, U.; Kanoun, O.; Tränkler, H.-R. Characterizing Aging Effects of Lithium Ion Batteries by Impedance Spectroscopy. *Electrochimica Acta* **2006**, *51* (8), 1664–1672. https://doi.org/10.1016/j.electacta.2005.02.148.

(31) Andre, D.; Meiler, M.; Steiner, K.; Walz, H.; Soczka-Guth, T.; Sauer, D. U. Characterization of High-Power Lithium-Ion Batteries by Electrochemical Impedance Spectroscopy. II: Modelling. *Journal of Power Sources* **2011**, *196* (12), 5349–5356. https://doi.org/10.1016/j.jpowsour.2010.07.071.

(32) Chen, C. H.; Liu, J.; Amine, K. Symmetric Cell Approach and Impedance Spectroscopy of High Power Lithium-Ion Batteries. *Journal of Power Sources* **2001**, 8.

(33) Imbeaux, J. C.; Savéant, J. M. Linear Sweep Voltammetry. Ohmic Drop and Chemical Polarization. *Journal of Electroanalytical Chemistry and Interfacial Electrochemistry* **1971**, *31* (1), 183–192. https://doi.org/10.1016/S0022-0728(71)80056-6.

(34) Hjelm, A.-K.; Lindbergh, G.; Lundqvist, A. Investigation of LiMn2O4 Cathodes for Use in Rechargeable Lithium Batteries by Linear Sweep Voltammetry: Part I. Theoretical Study. *Journal of Electroanalytical Chemistry* **2001**, *506* (2), 82–91. https://doi.org/10.1016/S0022-0728(01)00512-5.

(35) Levi, M. D.; Aurbach, D. The Mechanism of Lithium Intercalation in Graphite Film Electrodes in Aprotic Media. Part 1. High Resolution Slow Scan Rate Cyclic Voltammetric Studies and Modeling. *Journal of Electroanalytical Chemistry* **1997**, *421* (1), 79–88. https://doi.org/10.1016/S0022-0728(96)04832-2.

(36) Dubarry, M.; Truchot, C.; Liaw, B. Y. Synthesize Battery Degradation Modes via a Diagnostic and Prognostic Model. *Journal of Power Sources* **2012**, *219*, 204–216. https://doi.org/10.1016/j.jpowsour.2012.07.016.

(37) Dubarry, M.; Truchot, C.; Cugnet, M.; Liaw, B. Y.; Gering, K.; Sazhin, S.; Jamison, D.; Michelbacher, C. Evaluation of Commercial Lithium-Ion Cells Based on Composite Positive Electrode for Plug-in Hybrid Electric Vehicle Applications. Part I: Initial Characterizations. *Journal of Power Sources* **2011**, *196* (23), 10328–10335. https://doi.org/10.1016/j.jpowsour.2011.08.077.

(38) Mayur, M.; DeCaluwe, S. C.; Kee, B. L.; Bessler, W. G. Modeling and Simulation of the Thermodynamics of Lithium-Ion Battery Intercalation Materials in the Open-Source Software Cantera. *Electrochimica Acta* **2019**, *323*, 134797. https://doi.org/10.1016/j.electacta.2019.134797.

(39) Bloom, I.; Jansen, A. N.; Abraham, D. P.; Knuth, J.; Jones, S. A.; Battaglia, V. S.; Henriksen, G. L. Differential Voltage Analyses of High-Power, Lithium-Ion Cells: 1. Technique and Application. *Journal of Power Sources* **2005**, *139* (1), 295–303. https://doi.org/10.1016/j.jpowsour.2004.07.021.

(40) Keil, P.; Jossen, A. Calendar Aging of NCA Lithium-Ion Batteries Investigated by Differential Voltage Analysis and Coulomb Tracking. *J. Electrochem. Soc.* **2017**, *164* (1), A6066–A6074. https://doi.org/10.1149/2.0091701jes.

(41) Lewerenz, M.; Marongiu, A.; Warnecke, A.; Sauer, D. U. Differential Voltage Analysis as a Tool for Analyzing Inhomogeneous Aging: A Case Study for LiFePO4|Graphite Cylindrical Cells. *Journal of Power Sources* **2017**, *368*, 57–67. https://doi.org/10.1016/j.jpowsour.2017.09.059.

(42) Sieg, J.; Storch, M.; Fath, J.; Nuhic, A.; Bandlow, J.; Spier, B.; Sauer, D. U. Local Degradation and Differential Voltage Analysis of Aged Lithium-Ion Pouch Cells. *Journal of Energy Storage* **2020**, *30*, 101582. https://doi.org/10.1016/j.est.2020.101582.

(43) Wagemaker, M.; Van Der Ven, A.; Morgan, D.; Ceder, G.; Mulder, F. M.; Kearley, G. J. Thermodynamics of Spinel LixTiO2 from First Principles. *Chemical Physics* **2005**, *317* (2), 130–136. https://doi.org/10.1016/j.chemphys.2005.05.011.

(44) Karthikeyan, D. K.; Sikha, G.; White, R. E. Thermodynamic Model Development for Lithium Intercalation Electrodes. *Journal of Power Sources* **2008**, *185* (2), 1398–1407. https://doi.org/10.1016/j.jpowsour.2008.07.077.

(45) Tatsukawa, E.; Ikeda, T.; Tamura, K. Application of Gibbs Energy Model to Equilibrium Potential for Structural Phase Transition in Lithium Intercalation Process. *Fluid Phase Equilibria* **2013**, *357* (Supplement C), 19–23. https://doi.org/10.1016/j.fluid.2013.01.013.

(46) Lee, J.-W.; Hwang, D. Application of Thermodynamic Activity Models to the Equilibrium Potential for Lithium Intercalation Process of a Cobalt-Free Cathode Material with a Layered Structure. *Computational Materials Science* **2015**, *100* (Part A), 80–83. https://doi.org/10.1016/j.commatsci.2014.09.006.

(47) Verbrugge, M. W.; Koch, B. J. Electrochemical Analysis of Lithiated Graphite Anodes. *J. Electrochem. Soc.* **2003**, *150* (3), A374. https://doi.org/10.1149/1.1553788.

(48) Verbrugge, M.; Baker, D.; Koch, B.; Xiao, X.; Gu, W. Thermodynamic Model for Substitutional Materials: Application to Lithiated Graphite, Spinel Manganese Oxide, Iron Phosphate, and Layered Nickel-Manganese-Cobalt Oxide. *J. Electrochem. Soc.* **2017**, *164* (11), E3243–E3253. https://doi.org/10.1149/2.0341708jes.

(49) Baker, D. R.; Verbrugge, M. W. Multi-Species, Multi-Reaction Model for Porous Intercalation Electrodes: Part I. Model Formulation and a Perturbation Solution for Low-Scan-Rate, Linear-Sweep Voltammetry of a Spinel Lithium Manganese Oxide Electrode. *J. Electrochem. Soc.* **2018**, *165* (16), A3952–A3964. https://doi.org/10.1149/2.0771816jes.

(50) Orazem, M. E.; Tribollet, B. Experimental Methods. In *Electrochemical Impedance Spectroscopy*; John Wiley & Sons, Inc., 2008; pp 107–128. https://doi.org/10.1002/9780470381588.ch7.

(51) Yu, P.; Popov, B. N.; Ritter, J. A.; White, R. E. Determination of the Lithium Ion Diffusion Coefficient in Graphite. *J. Electrochem. Soc.* **1999**, *146* (1), 8–14. https://doi.org/10.1149/1.1391556.

(52) Levi, M. D.; Aurbach, D. Simultaneous Measurements and Modeling of the Electrochemical Impedance and the Cyclic Voltammetric Characteristics of Graphite Electrodes Doped with Lithium. *J. Phys. Chem. B* **1997**, *101* (23), 4630–4640. https://doi.org/10.1021/jp9701909.

(53) Zhang, S. S.; Xu, K.; Jow, T. R. EIS Study on the Formation of Solid Electrolyte Interface in Li-Ion Battery. *Electrochimica Acta* **2006**, *51* (8), 1636–1640. https://doi.org/10.1016/j.electacta.2005.02.137.

(54) Peled, E.; Menkin, S. Review—SEI: Past, Present and Future. *J. Electrochem. Soc.* **2017**, *164* (7), A1703–A1719. https://doi.org/10.1149/2.1441707jes.

(55) Barsoukov, E.; Kim, J. H.; Kim, J. H.; Yoon, C. O.; Lee, H. Effect of Low-Temperature Conditions on Passive Layer Growth on Li Intercalation Materials In Situ Impedance Study. *J. Electrochem. Soc.* **1998**, *145* (8), 2711–2717. https://doi.org/10.1149/1.1838703.

(56) Rahimian, S. K.; Rayman, S.; White, R. E. Comparison of Single Particle and Equivalent Circuit Analog Models for a Lithium-Ion Cell. *Journal of Power Sources* **2011**, *196* (20), 8450–8462. https://doi.org/10.1016/j.jpowsour.2011.06.007.

(57) Osaka, T.; Mukoyama, D.; Nara, H. Review—Development of Diagnostic Process for Commercially Available Batteries, Especially Lithium Ion Battery, by Electrochemical Impedance Spectroscopy. *J. Electrochem. Soc.* **2015**, *162* (14), A2529–A2537. https://doi.org/10.1149/2.0141514jes.

(58) Doyle, M.; Meyers, J. P.; Newman, J. Computer Simulations of the Impedance Response of Lithium Rechargeable Batteries. *J. Electrochem. Soc.* **2000**, *147* (1), 99–110. https://doi.org/10.1149/1.1393162.

(59) Fletcher, S. Tables of Degenerate Electrical Networks for Use in the Equivalent-Circuit Analysis of Electrochemical Systems. *J. Electrochem. Soc.* **1994**, *141* (7), 1823–1826. https://doi.org/10.1149/1.2055011.

(60) Darowicki, K. Linearization in Impedance Measurements. *Electrochimica Acta* **1997**, *42* (12), 1781–1788. https://doi.org/10.1016/S0013-4686(96)00377-5.

(61) Kiel, M.; Bohlen, O.; Sauer, D. U. Harmonic Analysis for Identification of Nonlinearities in Impedance Spectroscopy. *Electrochimica Acta* **2008**, *53* (25), 7367–7374. https://doi.org/10.1016/j.electacta.2008.01.089.

(62) Giner-Sanz, J. J.; Ortega, E. M.; Pérez-Herranz, V. Total Harmonic Distortion Based Method for Linearity Assessment in Electrochemical Systems in the Context of EIS. *Electrochimica Acta* **2015**, *186*, 598–612. https://doi.org/10.1016/j.electacta.2015.10.152.

(63) Giner-Sanz, J. J.; Ortega, E. M.; Pérez-Herranz, V. Harmonic Analysis Based Method for Perturbation Amplitude Optimization for EIS Measurements. *J. Electrochem. Soc.* **2017**, *164* (13), H918–H924. https://doi.org/10.1149/2.1451713jes.

(64) Bosch, R. W.; Bogaerts, W. F. Instantaneous Corrosion Rate Measurement with Small-Amplitude Potential Intermodulation Techniques. *CORROSION* **1996**, *52* (3), 204–212. https://doi.org/10.5006/1.3292115.

(65) Bosch, R. W.; Hubrecht, J.; Bogaerts, W. F.; Syrett, B. C. Electrochemical Frequency Modulation: A New Electrochemical Technique for Online Corrosion Monitoring. *CORROSION* **2001**, *57* (1), 60–70. https://doi.org/10.5006/1.3290331.

(66) Darowicki, K. Corrosion Rate Measurements by Non-Linear Electrochemical Impedance Spectroscopy. *Corrosion Science* **1995**, *37* (6), 913–925. https://doi.org/10.1016/0010-938X(95)00004-4.

(67) Wilson, W.; Wilson, J. R. Nonlinear Electrochemical Impedance Spectroscopy for Solid Oxide Fuel Cell Cathode Materials. *Electrochimica Acta* **2006**, *51* (8), 1389–1402.

(68) Wilson, J. R.; Sase, M.; Kawada, T.; Adler, S. B. Measurement of Oxygen Exchange Kinetics on Thin-Film La0.6Sr0.4CoO3 − δ Using Nonlinear Electrochemical Impedance Spectroscopy. *Electrochem. Solid-State Lett.* **2007**, *10* (5), B81–B86. https://doi.org/10.1149/1.2710178.

(69) Mao, Q.; Krewer, U. Sensing Methanol Concentration in Direct Methanol Fuel Cell with Total Harmonic Distortion: Theory and Application. *Electrochimica Acta* **2012**, *68*, 60–68. https://doi.org/10.1016/j.electacta.2012.02.018.

(70) Medina, J. A.; Schwartz, D. T. Nonlinear Dynamics of Modulated Flow between a Porous Injector and an Impermeable Substrate. *Physics of Fluids* **1996**, *8* (11), 2895–2905. https://doi.org/10.1063/1.869129.

(71) Medina, J. A.; Schwartz, D. T. Nonlinear Dynamics of Limiting Current in the Flow-Modulated Uniform-Injection Cell. *J. Electrochem. Soc.* **1997**, *144* (1), 155–164. https://doi.org/10.1149/1.1837378.

(72) Schwartz, D. T.; Stroeve, P.; Higgins, B. G. Fourier Transform Methods in Hydrodynamic Modulation Voltammetry. *J. Electrochem. Soc.* **1989**, *136* (6), 1755–1764. https://doi.org/10.1149/1.2097006.

(73) Smiechowski, M. F.; Lvovich, V. F.; Srikanthan, S.; Silverstein, R. L. Non-Linear Impedance Characterization of Blood Cells-Derived Microparticle Biomarkers Suspensions. *Electrochimica Acta* **2011**, *56* (23), 7763–7771. https://doi.org/10.1016/j.electacta.2011.03.116.

(74) Nakata, S.; Takitani, R.; Hirata, Y. Discrimination of Glucose from Its Interferences Using an Amperometric Sensor Based on Electrochemical Nonlinearity. *Anal. Chem.* **1998**, *70* (20), 4304–4308. https://doi.org/10.1021/ac980442h.

(75) Nakata, S.; Yoshikawa, K.; Matsuda, T. Voltage-Dependent Capacitance as a Probe for Albumin Adsorption onto a Solid Surface. *Biophysical Chemistry* **1992**, *42* (2), 213–220. https://doi.org/10.1016/0301-4622(92)85011-R.

(76) Harting, N.; Wolff, N.; Röder, F.; Krewer, U. Nonlinear Frequency Response Analysis (NFRA) of Lithium-Ion Batteries. *Electrochimica Acta* **2017**, *248* (Supplement C), 133–139. https://doi.org/10.1016/j.electacta.2017.04.037.

(77) Murbach, M. D.; Schwartz, D. T. Extending Newman's Pseudo-Two-Dimensional Lithium-Ion Battery Impedance Simulation Approach to Include the Nonlinear Harmonic Response. *J. Electrochem. Soc.* **2017**, *164* (11), E3311–E3320. https://doi.org/10.1149/2.0301711jes.

(78) Lvovich, V. F.; Smiechowski, M. F. Non-Linear Impedance Analysis of Industrial Lubricants. *Electrochimica Acta* **2008**, *53* (25), 7375–7385. https://doi.org/10.1016/j.electacta.2007.12.014.

(79) Xu, N.; Riley, D. J. Nonlinear Analysis of a Classical System: The Faradaic Process. *Electrochimica Acta* **2013**, *94*, 206–213. https://doi.org/10.1016/j.electacta.2013.01.141.

(80) Heubner, C.; Schneider, M.; Michaelis, A. Investigation of Charge Transfer Kinetics of Li-Intercalation in LiFePO4. *Journal of Power Sources* **2015**, *288*, 115–120. https://doi.org/10.1016/j.jpowsour.2015.04.103.

(81) Wolff, N.; Harting, N.; Heinrich, M.; Röder, F.; Krewer, U. Nonlinear Frequency Response Analysis on Lithium-Ion Batteries: A Model-Based Assessment.

Electrochimica Acta **2018**, *260*, 614–622. https://doi.org/10.1016/j.electacta.2017.12.097.

(82) Wolff, N.; Harting, N.; Heinrich, M.; Krewer, U. Nonlinear Frequency Response Analysis on Lithium-Ion Batteries: Process Identification and Differences between Transient and Steady-State Behavior. *Electrochimica Acta* **2019**, *298*, 788–798. https://doi.org/10.1016/j.electacta.2018.12.107.

(83) Masias, A.; Marcicki, J.; Paxton, W. A. Opportunities and Challenges of Lithium Ion Batteries in Automotive Applications. *ACS Energy Lett.* **2021**, *6* (2), 621–630. https://doi.org/10.1021/acsenergylett.0c02584.

(84) Buteau, S.; Dahn, J. R. Analysis of Thousands of Electrochemical Impedance Spectra of Lithium-Ion Cells through a Machine Learning Inverse Model. *J. Electrochem. Soc.* **2019**, *166* (8), A1611–A1622. https://doi.org/10.1149/2.1051908jes.

(85) McIntosh, D. Li-ion Battery Aging Datasets | NASA Open Data Portal https://data.nasa.gov/dataset/Li-ion-Battery-Aging-Datasets/uj5r-zjdb (accessed 2019 -09 -11).

(86) Severson, K. A.; Attia, P. M.; Jin, N.; Perkins, N.; Jiang, B.; Yang, Z.; Chen, M. H.; Aykol, M.; Herring, P. K.; Fraggedakis, D.; Bazant, M. Z.; Harris, S. J.; Chueh, W. C.; Braatz, R. D. Data-Driven Prediction of Battery Cycle Life before Capacity Degradation. *Nature Energy* **2019**, 1. https://doi.org/10.1038/s41560-019-0356-8.

(87) Aitio, A.; Howey, D. A. Predicting Battery End of Life from Solar Off-Grid System Field Data Using Machine Learning. *Joule* **2021**, *5* (12), 3204–3220. https://doi.org/10.1016/j.joule.2021.11.006.

(88) Lander, E. S.; Linton, L. M.; Birren, B.; Nusbaum, C.; Zody, M. C.; Baldwin, J.; Devon, K.; Dewar, K.; Doyle, M.; FitzHugh, W.; Funke, R.; Gage, D.; Harris, K.; Heaford, A.; Howland, J.; Kann, L.; Lehoczky, J.; LeVine, R.; McEwan, P.; McKernan, K.; Meldrim, J.; Mesirov, J. P.; Miranda, C.; Morris, W.; Naylor, J.; Raymond, C.; Rosetti, M.; Santos, R.; Sheridan, A.; Sougnez, C.; Stange-Thomann, N.; Stojanovic, N.; Subramanian, A.; Wyman, D.; Rogers, J.; Sulston, J.; Ainscough, R.; Beck, S.; Bentley, D.; Burton, J.; Clee, C.; Carter, N.; Coulson, A.; Deadman, R.; Deloukas, P.; Dunham, A.; Dunham, I.; Durbin, R.; French, L.; Grafham, D.; Gregory, S.; Hubbard, T.; Humphray, S.; Hunt, A.; Jones, M.; Lloyd, C.; McMurray, A.; Matthews, L.; Mercer, S.; Milne, S.; Mullikin, J.

C.; Mungall, A.; Plumb, R.; Ross, M.; Shownkeen, R.; Sims, S.; Waterston, R. H.; Wilson, R. K.; Hillier, L. W.; McPherson, J. D.; Marra, M. A.; Mardis, E. R.; Fulton, L. A.; Chinwalla, A. T.; Pepin, K. H.; Gish, W. R.; Chissoe, S. L.; Wendl, M. C.; Delehaunty, K. D.; Miner, T. L.; Delehaunty, A.; Kramer, J. B.; Cook, L. L.; Fulton, R. S.; Johnson, D. L.; Minx, P. J.; Clifton, S. W.; Hawkins, T.; Branscomb, E.; Predki, P.; Richardson, P.; Wenning, S.; Slezak, T.; Doggett, N.; Cheng, J.-F.; Olsen, A.; Lucas, S.; Elkin, C.; Uberbacher, E.; Frazier, M.; Gibbs, R. A.; Muzny, D. M.; Scherer, S. E.; Bouck, J. B.; Sodergren, E. J.; Worley, K. C.; Rives, C. M.; Gorrell, J. H.; Metzker, M. L.; Naylor, S. L.; Kucherlapati, R. S.; Nelson, D. L.; Weinstock, G. M.; Sakaki, Y.; Fujiyama, A.; Hattori, M.; Yada, T.; Toyoda, A.; Itoh, T.; Kawagoe, C.; Watanabe, H.; Totoki, Y.; Taylor, T.; Weissenbach, J.; Heilig, R.; Saurin, W.; Artiguenave, F.; Brottier, P.; Bruls, T.; Pelletier, E.; Robert, C.; Wincker, P.; Rosenthal, A.; Platzer, M.; Nyakatura, G.; Taudien, S.; Rump, A.; Smith, D. R.; Doucette-Stamm, L.; Rubenfield, M.; Weinstock, K.; Lee, H. M.; Dubois, J.; Yang, H.; Yu, J.; Wang, J.; Huang, G.; Gu, J.; Hood, L.; Rowen, L.; Madan, A.; Qin, S.; Davis, R. W.; Federspiel, N. A.; Abola, A. P.; Proctor, M. J.; Roe, B. A.; Chen, F.; Pan, H.; Ramser, J.; Lehrach, H.; Reinhardt, R.; McCombie, W. R.; de la Bastide, M.; Dedhia, N.; Blöcker, H.; Hornischer, K.; Nordsiek, G.; Agarwala, R.; Aravind, L.; Bailey, J. A.; Bateman, A.; Batzoglou, S.; Birney, E.; Bork, P.; Brown, D. G.; Burge, C. B.; Cerutti, L.; Chen, H.-C.; Church, D.; Clamp, M.; Copley, R. R.; Doerks, T.; Eddy, S. R.; Eichler, E. E.; Furey, T. S.; Galagan, J.; Gilbert, J. G. R.; Harmon, C.; Hayashizaki, Y.; Haussler, D.; Hermjakob, H.; Hokamp, K.; Jang, W.; Johnson, L. S.; Jones, T. A.; Kasif, S.; Kaspryzk, A.; Kennedy, S.; Kent, W. J.; Kitts, P.; Koonin, E. V.; Korf, I.; Kulp, D.; Lancet, D.; Lowe, T. M.; McLysaght, A.; Mikkelsen, T.; Moran, J. V.; Mulder, N.; Pollara, V. J.; Ponting, C. P.; Schuler, G.; Schultz, J.; Slater, G.; Smit, A. F. A.; Stupka, E.; Szustakowki, J.; Thierry-Mieg, D.; Thierry-Mieg, J.; Wagner, L.; Wallis, J.; Wheeler, R.; Williams, A.; Wolf, Y. I.; Wolfe, K. H.; Yang, S.-P.; Yeh, R.-F.; Collins, F.; Guyer, M. S.; Peterson, J.; Felsenfeld, A.; Wetterstrand, K. A.; Myers, R. M.; Schmutz, J.; Dickson, M.; Grimwood, J.; Cox, D. R.; Olson, M. V.; Kaul, R.; Raymond, C.; Shimizu, N.; Kawasaki, K.; Minoshima, S.; Evans, G. A.; Athanasiou, M.; Schultz, R.; Patrinos, A.; Morgan, M. J.; International Human Genome Sequencing Consortium; Whitehead Institute for Biomedical Research, C. for

G. R.; The Sanger Centre:; Washington University Genome Sequencing Center; US DOE Joint Genome Institute:; Baylor College of Medicine Human Genome Sequencing Center:; RIKEN Genomic Sciences Center:; Genoscope and CNRS UMR-8030:; Department of Genome Analysis, I. of M. B.; GTC Sequencing Center:; Beijing Genomics Institute/Human Genome Center:; Multimegabase Sequencing Center, T. I. for S. B.; Stanford Genome Technology Center:; University of Oklahoma's Advanced Center for Genome Technology:; Max Planck Institute for Molecular Genetics:; Cold Spring Harbor Laboratory, L. A. H. G. C.; GBF—German Research Centre for Biotechnology:; *Genome Analysis Group (listed in alphabetical order, also includes individuals listed under other headings):; Scientific management: National Human Genome Research Institute, U. N. I. of H.; Stanford Human Genome Center:; University of Washington Genome Center:; Department of Molecular Biology, K. U. S. of M.; University of Texas Southwestern Medical Center at Dallas:; Office of Science, U. D. of E.; The Wellcome Trust: Initial Sequencing and Analysis of the Human Genome. *Nature* **2001**, *409* (6822), 860–921. https://doi.org/10.1038/35057062.

(89) Jain, A.; Ong, S. P.; Hautier, G.; Chen, W.; Richards, W. D.; Dacek, S.; Cholia, S.; Gunter, D.; Skinner, D.; Ceder, G.; Persson, K. A. Commentary: The Materials Project: A Materials Genome Approach to Accelerating Materials Innovation. *APL Materials* **2013**, *1* (1), 011002. https://doi.org/10.1063/1.4812323.

(90) Barkholtz, H. M.; Fresquez, A.; Chalamala, B. R.; Ferreira, S. R. A Database for Comparative Electrochemical Performance of Commercial 18650-Format Lithium-Ion Cells. *J. Electrochem. Soc.* **2017**, *164* (12), A2697–A2706. https://doi.org/10.1149/2.1701712jes.

(91) Ward, L.; Babinec, S.; Dufek, E. J.; Howey, D. A.; Viswanathan, V.; Aykol, M.; Beck, D. A. C.; Blaiszik, B.; Chen, B.-R.; Crabtree, G.; de Angelis, V.; Dechent, P.; Dubarry, M.; Eggleton, E. E.; Finegan, D. P.; Foster, I.; Gopal, C.; Herring, P.; Hu, V. W.; Paulson, N. H.; Preger, Y.; Sauer, D. U.; Smith, K.; Snyder, S.; Sripad, S.; Tanim, T. R.; Tao, L. Principles of the Battery Data Genome. *arXiv:2109.07278 [physics]* **2021**.

(92) Dubarry, M.; Beck, D. Big Data Training Data for Artificial Intelligence-Based Li-Ion Diagnosis and Prognosis. *Journal of Power Sources* **2020**, *479*, 228806. https://doi.org/10.1016/j.jpowsour.2020.228806.

(93) Rumpf, K.; Rheinfeld, A.; Schindler, M.; Keil, J.; Schua, T.; Jossen, A. Influence of Cell-to-Cell Variations on the Inhomogeneity of Lithium-Ion Battery Modules. *J. Electrochem. Soc.* **2018**, *165* (11), A2587. https://doi.org/10.1149/2.0111811jes.

(94) Manthiram, A. A Reflection on Lithium-Ion Battery Cathode Chemistry. *Nat Commun* **2020**, *11* (1), 1550. https://doi.org/10.1038/s41467-020-15355-0.

(95) Feng, X.; Merla, Y.; Weng, C.; Ouyang, M.; He, X.; Liaw, B. Y.; Santhanagopalan, S.; Li, X.; Liu, P.; Lu, L.; Han, X.; Ren, D.; Wang, Y.; Li, R.; Jin, C.; Huang, P.; Yi, M.; Wang, L.; Zhao, Y.; Patel, Y.; Offer, G. A Reliable Approach of Differentiating Discrete Sampled-Data for Battery Diagnosis. *eTransportation* **2020**, *3*, 100051. https://doi.org/10.1016/j.etran.2020.100051.

(96) Schönleber, M.; Klotz, D.; Ivers-Tiffée, E. A Method for Improving the Robustness of Linear Kramers-Kronig Validity Tests. *Electrochimica Acta* **2014**, *131* (Supplement C), 20–27. https://doi.org/10.1016/j.electacta.2014.01.034.

(97) Murbach, M. D.; Gerwe, B.; Dawson-Elli, N.; Tsui, L. Impedance.Py: A Python Package for Electrochemical Impedance Analysis. *Journal of Open Source Software* **2020**, *5* (52), 2349. https://doi.org/10.21105/joss.02349.

(98) Hu, V. W.; Schwartz, D. Low Error Estimation of Half-Cell Thermodynamic Parameters from Whole-Cell Li-Ion Battery Experiments: Physics-Based Model Formulation, Experimental Demonstration, and an Open Software Tool. *J. Electrochem. Soc.* **2022**. https://doi.org/10.1149/1945-7111/ac5a1a.

(99) Hu, V. W.; Schwartz, D. T. *Data and Code for "Low Error Estimation of Half-Cell Thermodynamic Parameters from Whole-Cell Li-Ion Battery Experiments: Physics-Based Model Formulation, Experimental Demonstration, and an Open Software Tool";* Zenodo, 2022. https://doi.org/10.5281/zenodo.5847378.

(100) Cabañero, M. A.; Boaretto, N.; Röder, M.; Müller, J.; Kallo, J.; Latz, A. Direct Determination of Diffusion Coefficients in Commercial Li-Ion Batteries. *J. Electrochem. Soc.* **2018**, *165* (5), A847. https://doi.org/10.1149/2.0301805jes.

(101) Bridgewater, G.; Capener, M. J.; Brandon, J.; Lain, M. J.; Copley, M.; Kendrick, E. A Comparison of Lithium-Ion Cell Performance across Three Different Cell Formats. *Batteries* **2021**, *7* (2), 38. https://doi.org/10.3390/batteries7020038.

(102) Abraham, D. P.; Knuth, J. L.; Dees, D. W.; Bloom, I.; Christophersen, J. P. Performance Degradation of High-Power Lithium-Ion Cells—Electrochemistry of Harvested Electrodes. *Journal of Power Sources* **2007**, *170* (2), 465–475. https://doi.org/10.1016/j.jpowsour.2007.03.071.

(103) Truchot, C.; Dubarry, M.; Liaw, B. Y. State-of-Charge Estimation and Uncertainty for Lithium-Ion Battery Strings. *Applied Energy* **2014**, *119*, 218–227. https://doi.org/10.1016/j.apenergy.2013.12.046.

(104) Birkl, C. R.; McTurk, E.; Zekoll, S.; Richter, F. H.; Roberts, M. R.; Bruce, P. G.; Howey, D. A. Degradation Diagnostics for Commercial Lithium-Ion Cells Tested at − 10°C. *J. Electrochem. Soc.* **2017**, *164* (12), A2644. https://doi.org/10.1149/2.1401712jes.

(105) Birkl, C. R.; McTurk, E.; Roberts, M. R.; Bruce, P. G.; Howey, D. A. A Parametric Open Circuit Voltage Model for Lithium Ion Batteries. *J. Electrochem. Soc.* **2015**, *162* (12), A2271–A2280. https://doi.org/10.1149/2.0331512jes.

(106) Zhu, Y.; Gao, T.; Fan, X.; Han, F.; Wang, C. Electrochemical Techniques for Intercalation Electrode Materials in Rechargeable Batteries. *Acc. Chem. Res.* **2017**, *50* (4), 1022–1031. https://doi.org/10.1021/acs.accounts.7b00031.

(107) Dahn, J. R. Phase Diagram of ${\mathrm{Li}}_{\mathit{x}}$${\mathrm{C}}_{6}$. *Phys. Rev. B* **1991**, *44* (17), 9170–9177. https://doi.org/10.1103/PhysRevB.44.9170.

(108) Motohashi, T.; Ono, T.; Sugimoto, Y.; Masubuchi, Y.; Kikkawa, S.; Kanno, R.; Karppinen, M.; Yamauchi, H. Electronic Phase Diagram of the Layered Cobalt Oxide System ${\text{Li}}_{x}{\text{CoO}}_{2}$ $(0.0\ensuremath{\le}x\ensuremath{\le}1.0)$. *Phys. Rev. B* **2009**, *80* (16), 165114. https://doi.org/10.1103/PhysRevB.80.165114.

(109) Whittingham, M. S. Lithium Batteries and Cathode Materials. *Chem. Rev.* **2004**, *104* (10), 4271–4302. https://doi.org/10.1021/cr020731c.

(110) Tarascon, J. M.; Wang, E.; Shokoohi, F. K.; McKinnon, W. R.; Colson, S. The Spinel Phase of LiMn2 O 4 as a Cathode in Secondary Lithium Cells. *J. Electrochem. Soc.* **1991**, *138* (10), 2859–2864. https://doi.org/10.1149/1.2085330.

(111) Yang, S.; Song, Y.; Ngala, K.; Zavalij, P. Y.; Stanley Whittingham, M. Performance of LiFePO4 as Lithium Battery Cathode and Comparison with Manganese and Vanadium

Oxides. *Journal of Power Sources* **2003**, *119–121*, 239–246. https://doi.org/10.1016/S0378-7753(03)00240-4.

(112) Goodenough, J. B.; Kim, Y. Challenges for Rechargeable Li Batteries. *Chem. Mater.* **2010**, *22* (3), 587–603. https://doi.org/10.1021/cm901452z.

(113) Baker, D. R.; Verbrugge, M. W.; Gu, W. Multi-Species, Multi-Reaction Model for Porous Intercalation Electrodes: Part II. Model-Experiment Comparisons for Linear-Sweep Voltammetry of Spinel Lithium Manganese Oxide Electrodes. *J. Electrochem. Soc.* **2019**, *166* (4), A521. https://doi.org/10.1149/2.0091904jes.

(114) Dahn, H. M.; Smith, A. J.; Burns, J. C.; Stevens, D. A.; Dahn, J. R. User-Friendly Differential Voltage Analysis Freeware for the Analysis of Degradation Mechanisms in Li-Ion Batteries. *J. Electrochem. Soc.* **2012**, *159* (9), A1405. https://doi.org/10.1149/2.013209jes.

(115) Lee, S.; Siegel, J. B.; Stefanopoulou, A. G.; Lee, J.-W.; Lee, T.-K. Electrode State of Health Estimation for Lithium Ion Batteries Considering Half-Cell Potential Change Due to Aging. *J. Electrochem. Soc.* **2020**, *167* (9), 090531. https://doi.org/10.1149/1945-7111/ab8c83.

(116) Ando, K.; Matsuda, T.; Imamura, D. Degradation Diagnosis of Lithium-Ion Batteries with a LiNi0.5Co0.2Mn0.3O2 and LiMn2O4 Blended Cathode Using DV/DQ Curve Analysis. *Journal of Power Sources* **2018**, *390*, 278–285. https://doi.org/10.1016/j.jpowsour.2018.04.043.

(117) Baker, D. R.; Verbrugge, M. W. Intercalate Diffusion in Multiphase Electrode Materials and Application to Lithiated Graphite. *J. Electrochem. Soc.* **2012**, *159* (8), A1341. https://doi.org/10.1149/2.002208jes.

(118) Kasnatscheew, J.; Rodehorst, U.; Streipert, B.; Wiemers-Meyer, S.; Jakelski, R.; Wagner, R.; Laskovic, I. C.; Winter, M. Learning from Overpotentials in Lithium Ion Batteries: A Case Study on the LiNi1/3Co1/3Mn1/3O2 (NCM) Cathode. *J. Electrochem. Soc.* **2016**, *163* (14), A2943–A2950. https://doi.org/10.1149/2.0461614jes.

(119) Hu, V. W.; Schwartz, D. T. *Data and Code for "Adapting Electrochemical Half-Cell Thermodynamic Analysis to Whole-Cell Diagnostics of Lithium-Battery Cycling and Aging";* Zenodo, 2021. https://doi.org/10.5281/zenodo.5542603.

(120) Mao, Z.; Farkhondeh, M.; Pritzker, M.; Fowler, M.; Chen, Z. Calendar Aging and Gas Generation in Commercial Graphite/NMC-LMO Lithium-Ion Pouch Cell. *J. Electrochem. Soc.* **2017**, *164* (14), A3469–A3483. https://doi.org/10.1149/2.0241714jes.

(121) Nitta, N.; Wu, F.; Lee, J. T.; Yushin, G. Li-Ion Battery Materials: Present and Future. *Materials Today* **2015**, *18* (5), 252–264. https://doi.org/10.1016/j.mattod.2014.10.040.

(122) Zheng, J.; Yan, P.; Zhang, J.; Engelhard, M. H.; Zhu, Z.; Polzin, B. J.; Trask, S.; Xiao, J.; Wang, C.; Zhang, J. Suppressed Oxygen Extraction and Degradation of LiNixMnyCozO2 Cathodes at High Charge Cut-off Voltages. *Nano Research* **2017**, *10* (12). https://doi.org/10.1007/s12274-017-1761-6.

(123) Jung, S.-K.; Gwon, H.; Hong, J.; Park, K.-Y.; Seo, D.-H.; Kim, H.; Hyun, J.; Yang, W.; Kang, K. Understanding the Degradation Mechanisms of LiNi0.5Co0.2Mn0.3O2 Cathode Material in Lithium Ion Batteries. *Advanced Energy Materials* **2014**, *4* (1), 1300787. https://doi.org/10.1002/aenm.201300787.

(124) Zhang, Y.; Xie, H.; Jin, H.; Zhang, Q.; Li, Y.; Li, X.; Li, K.; Bao, C. Research Status of Spinel LiMn $_2$ O $_4$ Cathode Materials for Lithium Ion Batteries. *IOP Conf. Ser.: Earth Environ. Sci.* **2020**, *603*, 012051. https://doi.org/10.1088/1755-1315/603/1/012051.

(125) Ohzuku, T.; Kitagawa, M.; Hirai, T. Electrochemistry of Manganese Dioxide in Lithium Nonaqueous Cell III . X-Ray Diffractional Study on the Reduction of Spinel-Related Manganese Dioxide. *J. Electrochem. Soc.* **1990**, *137* (3), 769–775. https://doi.org/10.1149/1.2086552.

(126) Gallagher, K. G.; Dees, D. W.; Jansen, A. N.; Abraham, D. P.; Kang, S.-H. A Volume Averaged Approach to the Numerical Modeling of Phase-Transition Intercalation Electrodes Presented for LixC6. *J. Electrochem. Soc.* **2012**, *159* (12), A2029–A2037. https://doi.org/10.1149/2.015301jes.

(127) Li, T.; Yuan, X.-Z.; Zhang, L.; Song, D.; Shi, K.; Bock, C. Degradation Mechanisms and Mitigation Strategies of Nickel-Rich NMC-Based Lithium-Ion Batteries. *Electrochem. Energ. Rev.* **2020**, *3* (1), 43–80. https://doi.org/10.1007/s41918-019-00053-3.

(128) Tornheim, A.; O'Hanlon, D. C. What Do Coulombic Efficiency and Capacity Retention Truly Measure? A Deep Dive into Cyclable Lithium Inventory, Limitation Type, and Redox Side Reactions. *J. Electrochem. Soc.* **2020**, *167* (11), 110520. https://doi.org/10.1149/1945-7111/ab9ee8.

(129) Pender, J. P.; Jha, G.; Youn, D. H.; Ziegler, J. M.; Andoni, I.; Choi, E. J.; Heller, A.; Dunn, B. S.; Weiss, P. S.; Penner, R. M.; Mullins, C. B. Electrode Degradation in Lithium-Ion Batteries. *ACS Nano* **2020**, *14* (2), 1243–1295. https://doi.org/10.1021/acsnano.9b04365.

(130) Zhang, D.; Haran, B. S.; Durairajan, A.; White, R. E.; Podrazhansky, Y.; Popov, B. N. Studies on Capacity Fade of Lithium-Ion Batteries. *Journal of Power Sources* **2000**, *91* (2), 122–129. https://doi.org/10.1016/S0378-7753(00)00469-9.

(131) Saha, B.; Goebel, K.; Poll, S.; Christophersen, J. Prognostics Methods for Battery Health Monitoring Using a Bayesian Framework. *IEEE Transactions on Instrumentation and Measurement* **2009**, *58* (2), 291–296. https://doi.org/10.1109/TIM.2008.2005965.

(132) Song, J.; Bazant, M. Z. Effects of Nanoparticle Geometry and Size Distribution on Diffusion Impedance of Battery Electrodes. *J. Electrochem. Soc.* **2012**, *160* (1), A15. https://doi.org/10.1149/2.023301jes.

(133) Chikkannanavar, S. B.; Bernardi, D. M.; Liu, L. A Review of Blended Cathode Materials for Use in Li-Ion Batteries. *Journal of Power Sources* **2014**, *248*, 91–100. https://doi.org/10.1016/j.jpowsour.2013.09.052.

(134) Murbach, M. D.; Hu, V.; Schwartz, D. T. Nonlinear Electrochemical Impedance Spectroscopy of Lithium-Ion Batteries: Experimental Approach, Analysis, and Initial Findings. *ECSarXiv* **2018**. https://doi.org/10.17605/OSF.IO/T635X.

(135) Murbach, M. D.; Hu, V. W. Data and Supplementary Notebook for NLEIS Manuscript.

(136) Armand, M.; Tarascon, J.-M. Building Better Batteries. *Nature* **2008**, *451* (7179), 652–657.

(137) Orazem, M. E.; Tribollet, B. *Electrochemical Impedance Spectroscopy*; The Electrochemical Society series; Wiley: Hoboken, N.J, 2008.

(138) Zhang, S. S.; Xu, K.; Jow, T. R. EIS Study on the Formation of Solid Electrolyte Interface in Li-Ion Battery. *Electrochimica Acta* **2006**, *51* (8), 1636–1640. https://doi.org/10.1016/j.electacta.2005.02.137.

(139) Gilbert, J. A.; Bareño, J.; Spila, T.; Trask, S. E.; Miller, D. J.; Polzin, B. J.; Jansen, A. N.; Abraham, D. P. Cycling Behavior of NCM523/Graphite Lithium-Ion Cells in the 3–4.4 V Range: Diagnostic Studies of Full Cells and Harvested Electrodes. *J. Electrochem. Soc.* **2017**, *164* (1), A6054–A6065. https://doi.org/10.1149/2.0081701jes.

(140) Osaka, T.; Mukoyama, D.; Nara, H. Review—Development of Diagnostic Process for Commercially Available Batteries, Especially Lithium Ion Battery, by Electrochemical Impedance Spectroscopy. *Journal of The Electrochemical Society* **2015**, *162* (14), A2529–A2537.

(141) Murbach, M. D.; Schwartz, D. T. Analysis of Li-Ion Battery Electrochemical Impedance Spectroscopy Data: An Easy-to-Implement Approach for Physics-Based Parameter Estimation Using an Open-Source Tool. *Journal of The Electrochemical Society* **2018**, *165* (2), A297–A304. https://doi.org/10.1149/2.1021802jes.

(142) Doyle, M.; Meyers, J. P.; Newman, J. Computer Simulations of the Impedance Response of Lithium Rechargeable Batteries. *Journal of The Electrochemical Society* **2000**, *147* (1), 99–110.

(143) Wilson, J. R.; Schwartz, D. T.; Adler, S. B. Nonlinear Electrochemical Impedance Spectroscopy for Solid Oxide Fuel Cell Cathode Materials. *Electrochimica Acta* **2006**, *51* (8–9), 1389–1402. https://doi.org/10.1016/j.electacta.2005.02.109.

(144) Hirschorn, B.; Ibrahim, I.; Orazem, M. E.; Takenouti, H.; Tribollet, B. Effect of Large Perturbation Amplitudes on the Impedance Response of an Electrochemical System; ECS, 2008; pp 81–100. https://doi.org/10.1149/1.3004031.

(145) Giner-Sanz, J. J.; Ortega, E. M.; Pérez-Herranz, V. Total Harmonic Distortion Based Method for Linearity Assessment in Electrochemical Systems in the Context of EIS. *Electrochimica Acta* **2015**, *186*, 598–612. https://doi.org/10.1016/j.electacta.2015.10.152.

(146) Giner-Sanz, J. J.; Ortega, E. M.; Pérez-Herranz, V. Harmonic Analysis Based Method for Perturbation Amplitude Optimization for EIS Measurements. *Journal of The Electrochemical Society* **2017**, *164* (13), H918–H924.

(147) Kadyk, T.; Hanke-Rauschenbach, R.; Sundmacher, K. Nonlinear Frequency Response Analysis of Dehydration Phenomena in Polymer Electrolyte Membrane Fuel Cells. *International Journal of Hydrogen Energy* **2012**, *37* (9), 7689–7701. https://doi.org/10.1016/j.ijhydene.2012.01.148.

(148) Medina, J. A.; Schwartz, D. T. Nonlinear Dynamics of Modulated Flow between a Porous Injector and an Impermeable Substrate. *Physics of Fluids (1994-present)* **1996**, *8* (11), 2895–2905.

(149) Medina, J. A.; Schwartz, D. T. Nonlinear Dynamics of Limiting Current in the Flow-Modulated Uniform-Injection Cell. *Journal of the Electrochemical Society* **1997**, *144* (1), 155–164.

(150) Smiechowski, M. F.; Lvovich, V. F.; Srikanthan, S.; Silverstein, R. L. Non-Linear Impedance Characterization of Blood Cells-Derived Microparticle Biomarkers Suspensions. *Electrochimica Acta* **2011**, *56* (23), 7763–7771. https://doi.org/10.1016/j.electacta.2011.03.116.

(151) Murbach, M. D.; Schwartz, D. T. Extending Newman's Pseudo-Two-Dimensional Lithium-Ion Battery Impedance Simulation Approach to Include the Nonlinear Harmonic Response. *Journal of The Electrochemical Society* **2017**, *164* (11), E3311–E3320. https://doi.org/10.1149/2.0301711jes.

(152) Wolff, N.; Harting, N.; Heinrich, M.; Röder, F.; Krewer, U. Nonlinear Frequency Response Analysis on Lithium-Ion Batteries: A Model-Based Assessment. *Electrochimica Acta* **2018**, *260*, 614–622. https://doi.org/10.1016/j.electacta.2017.12.097.

(153) Harting, N.; Schenkendorf, R.; Wolff, N.; Krewer, U. State-of-Health Identification of Lithium-Ion Batteries Based on Nonlinear Frequency Response Analysis: First Steps with Machine Learning. *Applied Sciences* **2018**, *8* (5), 821. https://doi.org/10.3390/app8050821.

(154) Harting, N.; Wolff, N.; Krewer, U. Identification of Lithium Plating in Lithium-Ion Batteries Using Nonlinear Frequency Response Analysis (NFRA). *Electrochimica Acta* **2018**, *281*, 378–385. https://doi.org/10.1016/j.electacta.2018.05.139.

(155) Barai, A.; Chouchelamane, G. H.; Guo, Y.; McGordon, A.; Jennings, P. A Study on the Impact of Lithium-Ion Cell Relaxation on Electrochemical Impedance Spectroscopy. *Journal of Power Sources* **2015**, *280*, 74–80. https://doi.org/10.1016/j.jpowsour.2015.01.097.

(156) Schönleber, M.; Klotz, D.; Ivers-Tiffée, E. A Method for Improving the Robustness of Linear Kramers-Kronig Validity Tests. *Electrochimica Acta* **2014**, *131*, 20–27. https://doi.org/10.1016/j.electacta.2014.01.034.

(157) Atebamba, J.-M.; Moskon, J.; Pejovnik, S.; Gaberscek, M. On the Interpretation of Measured Impedance Spectra of Insertion Cathodes for Lithium-Ion Batteries. *Journal of The Electrochemical Society* **2010**, *157* (11), A1218. https://doi.org/10.1149/1.3489353.

(158) Erol, S.; Orazem, M. E. The Influence of Anomalous Diffusion on the Impedance Response of LiCoO2|C Batteries. *Journal of Power Sources* **2015**, *293*, 57–64. https://doi.org/10.1016/j.jpowsour.2015.05.047.

(159) Pathak, M.; Murbach, M. D.; Pathak, C.; Jang, T.-J.; Qi, Y.; Schwartz, D. T.; Subramanian, V. R. Fast Impedance Simulation of Lithium-Ion Batteries with Pseudo-Two Dimensional Electrochemical Models. *J. Electrochem. Soc.* **2018**, *165* (7), A1324–A1337. https://doi.org/10.1149/2.0831805jes.